



2010-08-13

Acoustical Analysis of a Horn-Loaded Compression Drivers Using Numerical Analysis

Daniel Ross Tengelsen
Brigham Young University - Provo

Follow this and additional works at: <https://scholarsarchive.byu.edu/etd>

 Part of the [Astrophysics and Astronomy Commons](#), and the [Physics Commons](#)

BYU ScholarsArchive Citation

Tengelsen, Daniel Ross, "Acoustical Analysis of a Horn-Loaded Compression Drivers Using Numerical Analysis" (2010). *All Theses and Dissertations*. 2448.

<https://scholarsarchive.byu.edu/etd/2448>

This Thesis is brought to you for free and open access by BYU ScholarsArchive. It has been accepted for inclusion in All Theses and Dissertations by an authorized administrator of BYU ScholarsArchive. For more information, please contact scholarsarchive@byu.edu, ellen_amatangelo@byu.edu.

ACOUSTICAL ANALYSIS OF HORN-LOADED COMPRESSION DRIVERS
USING NUMERICAL TECHNIQUES

Daniel R. Tengelsen

A thesis submitted to the faculty of
Brigham Young University
in partial fulfillment of the requirements for the degree of
Master of Science

Timothy W. Leishman, Advisor

Vianey Villamizar

Kent Gee

Brian E. Anderson

Department of Physics and Astronomy

Brigham Young University

December 2010

Copyright © 2010 Daniel R. Tengelsen

All Rights Reserved

ABSTRACT

ACOUSTICAL ANALYSIS OF HORN-LOADED COMPRESSION DRIVERS USING NUMERICAL TECHNIQUES

Daniel R. Tengelsen

Department of Physics and Astronomy

Master of Science

Two numerical techniques, the boundary-element method (BEM) and the finite-difference method (FDM), are used for simulating the radiation from horn-loaded compression drivers and from an infinitely-baffled, finite-length pipe. While computations of the horn-loaded compression driver are in steady state, transient analysis of the finite-length pipe is studied as a precursor to transient analysis within the horn-loaded compression driver. BEM numerical simulations show promise for the development of new designs. Numerical simulations serve as a good tool for time and cost-effective prototyping as poor designs are detected before they are built.

ACKNOWLEDGMENTS

Many people are responsible for my success as a graduate student at BYU. Inevitably, there will be many people who I forget to thank here; however, I do wish to point out the individuals that deserve recognition.

I want to thank Dr. Anderson for his ambition and keen insight into this research. His motivation and advisement has helped me to better understand the station and objective of a researcher. I want to thank Dr. Villamizar for the wonderful class in finite-difference methods that made this research possible. I especially thank him for his patience as I attempted time and time again to be more mathematically inclined. Thank you for the extra seminars, conversations, and friendship. I thank Dr. Leishman for his help on this project—even through his sabbatical. I venture that many professors do not have such a kind and giving heart. I thank Dr. Gee and Dr. Sommerfeldt both for entertaining my many questions, often at times which were inconvenient. Acoustics Research Group members Buye Xu, Dave Krueger, Alan Wall, Cole Duke, and Matt Shaw deserve my thanks for listening to me and for their invaluable advice. Members Michael Muhlestein and Sam Anderson deserve special thanks for all the hours they gave to help take measurements.

Most of all, I want to thank my wife. Her many sacrifices have allowed me to work long hours and weekends to earn this degree. When the professors go to their homes and I am still struggling to finish my work, her attitude carries me and encourages me to keep moving forward. Thank you, Kate, for never letting your eyes glaze as I talk about my research.

Contents

Table of Contents	vi
List of Figures.....	viii
List of Tables and Charts.....	xii
Chapter 1	1
Introduction.....	1
1.1 Background.....	1
1.2 Research Objectives.....	2
1.3 Outline.....	3
Chapter 2	5
Numerical Techniques	5
2.1 Background.....	5
2.2 The Boundary Element Method.....	6
2.2.1 Important Considerations.....	8
2.2.1.1 Consideration 1: Nodes and Elements	9
2.2.1.2 Consideration 2: Matrix Values	11
2.2.1.3 Consideration 3: Absorptive Boundary Conditions	16
2.3 The Finite Difference Method	17
2.3.1 Approximating Derivatives via Taylor Series Expansions.....	18
2.3.1.1 Example: Approximating a First Derivative.....	19
2.4 The Finite Element Method	21
2.5 Selection of an Appropriate Computational Method	21
Chapter 3	25
Transient Analysis from Finite-Length Pipes	25
3.1 Background.....	25
3.2 The Mathematical Model.....	28
3.2.1 The Physical Problem	28
3.2.2 The Physical Problem in Generalized Curvilinear Coordinates	31
3.2.3 Elliptic Grid Generation.....	36
3.2.4 Discretization	38
3.2 Numerical Simulation	42
3.3 FDM Results	45
3.4 Discussion.....	51

3.5	Conclusions.....	54
Chapter 4	57
Steady-State Analysis of Horns with Simplified Excitation Signals		57
4.1	Background.....	57
4.2	Modeling of Existing Horns.....	61
4.3	Input Wavefront Study.....	70
4.3.1	Comparative Study of Directivity	71
4.3.2	Comparative Study of Frequency Response	76
4.4	Higher-Frequency Disagreement	78
4.5	Conclusions.....	87
Chapter 5	89
Steady-State Analysis of Horn-Loaded Compression Drivers		89
5.1	Background.....	89
5.2	The Diaphragm	93
5.2.1	Natural Modes.....	94
5.2.2	SLDV Scans.....	100
5.3	Phase Plugs	107
5.3.1	Modeling of Existing Compression Driver.....	108
5.3.1.1	Model Specifications	108
5.3.1.2	Parasitic Resonances	114
5.3.2	Phase Plug Study.....	118
5.4	Conclusions.....	122
Chapter 6	125
Conclusions.....		125
6.1	Conclusions.....	125
6.2	Future Work	128
Bibliography	131
Appendix	141
MATLAB Code		141
A.1	MainWave.m.....	141
A.2	LeapFrog_Step.m.....	145
A.3	Horn_Step.m	151
A.4	Metrics_Step.m	152
A.5	InitialGrid.m.....	156
A.6	interpoint.m.....	157
A.7	gridgen.m	158

List of Figures

Figure 2.1	(a) A continuous boundary. (b) A discrete representation of the continuous boundary. In (b), nodes are indicated by the circles and elements are indicated by the straight lines.6
Figure 2.2	(a) Chosen discrete x-values. (b) Output values of $f(x)$ at discrete x-values. (c) Relationships between nodes (elements/lines connecting nodes).10
Figure 2.3	(a) Geometry of a two-dimensional problem considered for Section 2.2.1.2. (b) Two-dimensional problem dissected into nodes and elements. Elements are indicated by the lines and starred (*) numbers. Nodes are indicated by the circles and regular numbers.12
Figure 3.1	Physical domain used to study transient radiation from a finite-length pipe.....29
Figure 3.2	Pictorial relationship between cylindrical and Cartesian coordinates.32
Figure 3.3	Transformation used in the generation of boundary conforming coordinates.....32
Figure 3.4	Wave propagation images for a single-cycle 16 kHz excitation signal in the (0,0) mode. Wave propagation for the full spatial model is shown to scale in (a), (c), and (e). Wave propagation within the pipe at an exaggerated vertical scale is shown in (b), (d), and (f). The times for each subplot are as follows: (a) and (b) 0.0625 ms, (c) and (d) 1.5 ms, (e) and (f) 2.2 ms.46
Figure 3.5	Wave propagation images for a single-cycle 16 kHz excitation signal in the (0,1) mode. Wave propagation for the full spatial model is shown to scale in (a), (c), and (e). Wave propagation within the pipe at an exaggerated vertical scale is shown in (b), (d), and (f). The times for each subplot are as follows: (a) and (b) 0.0625 ms, (c) and (d) 1.5 ms, (e) and (f) 2.2 ms.47
Figure 3.6	Far-field radiation (pressure magnitude) measured at 0.508 meters from the exit of the pipe as a function of angle and time. (a) (0,0) mode. (b) (0,1) mode. (c) (0,2) mode. (d) Combination of several modes.51
Figure 4.1	Pictorial illustration of a full horn model and a reduced quarter of the model. Pink boundary represents excitation source.....63
Figure 4.2	Mesh of existing horn used in BE simulation.63

Figure 4.3	Comparison of pressure directivity in dB (normalized to 0 dB) of a simulated 30° x 45° horn (---) and experimental measurement (—). The decibel value is indicated radially and 0 degrees is on-axis with the horn. The 30° slice is shown.	66
Figure 4.4	Comparison of pressure directivity in dB (normalized to 0 dB) of a simulated 30° x 45° horn (---) and experimental measurement (—). The decibel value is indicated radially and 0 degrees is on-axis with the horn. The 45° slice is shown.	67
Figure 4.5	Comparison of pressure directivity in dB (normalized to 0 dB) of a simulated 120° x 60° horn (---) and experimental measurement (—). The decibel value is indicated radially and 0 degrees is on-axis with the horn. The 120° slice is shown.	68
Figure 4.6	Comparison of pressure directivity in dB (normalized to 0 dB) of a simulated 120° x 60° horn (---) and experimental measurement (—). The decibel value is indicated radially and 0 degrees is on-axis with the horn. The 60° slice is shown.	69
Figure 4.7	Illustration of the different curvatures used for input wavefront study: (a) an outward curvature, (b) no curvature, and (c) an inward curvature. Not drawn to scale.	71
Figure 4.8	Comparison of pressure directivity in dB (normalized to 0 dB) of a simulated 30° x 45° horn inward (---), outward (), and no curvature (—). The decibel value is indicated radially and 0 degrees is on-axis with the horn. The 30° slice is shown.	72
Figure 4.9	Comparison of pressure directivity in dB (normalized to 0 dB) of a simulated 30° x 45° horn inward (---), outward (), and no curvature (—). The decibel value is indicated radially and 0 degrees is on-axis with the horn. The 45° slice is shown.	73
Figure 4.10	Comparison of pressure directivity in dB (normalized to 0 dB) of a simulated 120° x 60° horn inward (---), outward (), and no curvature (—). The decibel value is indicated radially and 0 degrees is on-axis with the horn. The 120° slice is shown.	74
Figure 4.11	Comparison of pressure directivity in dB (normalized to 0 dB) of a simulated 120° x 60° horn inward (---), outward (), and no curvature (—). The decibel value is indicated radially and 0 degrees is on-axis with the horn. The 60° slice is shown.	75
Figure 4.12	Simulated results for on-axis frequency response of a 30° x 45° horn with different input wavefront curvatures.	77

Figure 4.13	On-axis frequency response numerical simulations of a 120° x 60° horn for different input wavefront curvatures.....	77
Figure 4.14	Side view of the horns simulated in Sec. 4.3. The 30° cross section of the 30° x 45° horn is shown on the left and the 120° cross section of the 120° x 60° horn is shown on the right.	80
Figure 4.15	Pressure magnitude of the interior pressure field for the 120° x 60° horn along the 120° cross section at 4 kHz.	81
Figure 4.16	Pressure magnitude of the interior pressure field for the 120° x 60° horn along the 120° cross section at 10 kHz.	82
Figure 4.17	Pressure magnitude of the interior pressure field for the 120° x 60° horn along the 120° cross section at 16 kHz.	83
Figure 4.18	Pressure magnitude of the interior pressure field for the 120° x 60° horn along the 60° cross section at 4 kHz.	84
Figure 4.19	Pressure magnitude of the interior pressure field for the 120° x 60° horn along the 60° cross section at 10 kHz.	85
Figure 4.20	Pressure magnitude of the interior pressure field for the 120° x 60° horn along the 60° cross section at 16 kHz.	86
Figure 5.1	Illustration of the cross section of a compression driver. The illustration is motivated by an Electrovoice ND6 compression driver schematic. Drawing not to scale.	90
Figure 5.2	Illustration of the compression driver diaphragm.	94
Figure 5.3	Predicted modes for a spherical cap. Mode: (a) (0,0); (b) (0,1); (c) (1,0); (d) (1,1).	99
Figure 5.4	Spatial velocity profiles of a compression driver diaphragm driven at 12.8 kHz. (a) SLDV data used for reconstruction. (b) Reconstruction of Scanning Laser Doppler Vibrometer (SLDV) data using natural modes.	102
Figure 5.5	(a) Scanning Laser Doppler Vibrometer (SLDV) measurement with no additional loading. (b) SLDV measurement with clay fit into outside edge of compression driver exit. (c) The magnitude of the difference of both velocity profiles.	104
Figure 5.6	(a) Scanning Laser Doppler Vibrometer (SLDV) measurement with no additional loading. (b) SLDV measurement with a 30° x 45° horn mounted to the compression driver. (c) The magnitude of the difference of both velocity profiles.	105

Figure 5.7	Directivity results of Boundary-Element (BE) simulations run with, and without, the reconstructed Scanning Laser Doppler Vibrometer data. Both results are compared to experimental data of the physical system. The BE simulations are mounted to a 30° x 45° horn.....	106
Figure 5.8	Mesh used in simulation. A side view (top) and a back view (bottom) are shown.	109
Figure 5.9	Drawing indicating receiver locations (red dots) found in each numerical simulation where the compression driver is mounted to the reference horn. This drawing is not to scale.	111
Figure 5.10	Frequency response results for simulation and experiment of an ND6 compression driver on a 45° x 30° horn. Measurement is on-axis, 3.048 m from the entrance of the horn.....	112
Figure 5.11	Frequency response for simulated and experimental results of an ND6 compression driver on a 120° x 60° horn. Measurement is on-axis, 3.048 m from the entrance of the horn.....	112
Figure 5.12	Illustration of the gap in the BE mesh (top) that causes a parasitic resonance, and the reduced boundary (bottom) used to eliminate it.....	116
Figure 5.13	Frequency response comparison at compression driver exit of an existing model with and without the boundary causing a parasitic resonance at 2.5 kHz.....	117
Figure 5.14	Comparison of on-axis frequency response radiation for models 1, 2, and 3.....	120
Figure 5.15	Comparison of on-axis frequency response radiation for Model 1, 6, and 7.....	122

List of Tables and Charts

Table 3.1	Angles of maximum pressure radiation for the first three modes of the pipe.....	52
Table 5.1	Description of the seven compression driver models used in the study of phase plug designs.	119

Chapter 1

Introduction

1.1 Background

A horn-loaded compression driver is a high-frequency sound reproduction device commonly used in professional audio systems. They are used for sound reinforcement in arenas, auditoria, large churches, outdoor concert venues, and in other large-scale audience applications. Typically, its purpose is to reproduce frequencies between around 1 kHz to 20 kHz (though sometimes spanning lower frequency ranges) with as much amplitude very high amplitude without sacrificing the fidelity of the signal to various forms of distortion.

The typical design process for horns and compression drivers involves a prototyping phase. During this part of the design process, a single version (prototype) of each type of several different new horns or compression drivers is created. Each prototype is rigorously compared with other prototypes and existing production designs through measurements of on-axis

frequency response and angular directivity. If the prototype improves upon existing designs, the prototype may become part of the next generation of products. Unfortunately, the design process for horns or compression drivers often includes guesswork and is sometimes not very scientific. This results in costly and time-consuming prototyping processes, which may be repeated several times until an appropriate design is discovered.

With the advent of sufficient computing power, numerical simulations are becoming an important tool in the scientific analysis of new designs. These simulations precede the prototyping phase and can help loudspeaker engineering companies by providing an efficient first step in the design process, eliminating poor prototypes before they are created physically and tested experimentally.

In general, the three most widely used numerical schemes for loudspeaker design are the boundary-element method (BEM), the finite-difference method (FDM), and the finite-element method (FEM). Each method has its advantages, which must be understood to select the most efficient scheme for the system under study. Boundary-element (BE) and finite-difference (FD) techniques are performed in this thesis, though much work employing the FEM has shown that it has merit as well in modeling compression drivers.

1.2 Research Objectives

One goal of the work presented in this thesis is to study various aspects of the acoustics and vibration important to both the horn and compression driver using BE numerical methods. For horns, both the directivity and frequency response are compared for several existing designs. This process not only tested the abilities of the numerical method, but the comparative abilities

of the simulation results as well. For compression drivers, an existing design was compared to several different prototype designs. They provided comparative results to help determine which models best qualified for physical prototyping.

Another research objective was to better understand the transient nature of horn-loaded compression driver systems that are most often used to radiate signals that are inherently transient in nature themselves. Fundamental research in this area may help improve the sound-reproduction abilities of the horn-loaded compression driver for both transient and steady-state signals. Because the commercial BEM package available for this research was only able to perform steady-state analysis, the FDM was used instead to lay the groundwork for possible future transient analysis. This thesis explored infinitely-baffled, finite-length pipes to better understand the importance of transient analysis in horns. Although general acoustical analysis of wave propagation in pipes is well researched, the numerical methods used for simulation are constantly being explored and improved upon.

1.3 Outline

Chapter 2 provides a semiformal introduction to the numerical methods employed in this thesis, the BEM and the FDM. A very basic introduction to the FEM is also given. The chapter is intended to help the reader better understand the general concepts behind numerical methods and to be more informed on which numerical method performs best for a given problem.

Chapter 3 explores analytical and numerical groundwork for transient analysis. It uses the FDM to study transient signal wave propagation through an infinitely-baffled, finite-length pipe system. The pipe serves as a precursor to the possible transient analysis that could be performed

on horns or other problems where transient analysis may be beneficial. Pipes are used due to their prevalent use and analytically definable geometry. Future work may look at similar transient analysis of horns and may provide an exciting new area of research for the professional audio industry. The Appendix includes the MATLAB code used to generate the FD results presented in Ch. 3.

Chapter 4 provides analysis of several existing horns using the BEM. It explores a specific set of horns whose directivities have been measured experimentally. The numerical simulations are compared with experimental data to verify that the BE simulations produce reliable results. A BE study is then conducted in which the spatial profile of the input wavefront is altered on several different horns in an attempt to determine an optimal spatial profile desired for the exiting wavefront from the compression driver. Two horns are given as examples to summarize results from several horns.

Chapter 5 provides both vibrational and acoustical analysis of the compression driver. It contains an analysis of the mechanical vibrations of the driver diaphragm. Laser vibrometer scans of diaphragm vibrations are extracted experimentally, compared with analytically-derived natural modes for a spherical cap, and the analytical results are subsequently used in BE simulations. The chapter then analyzes a group of newly-designed compression drivers and performs a relative comparison among the different models to demonstrate the possible use of numerical packages to provide insight into prototype designs before they are constructed.

Chapter 6 provides general conclusions for the thesis. It also identifies future work that may be based on the ground work has been provided by this thesis.

It should be noted here that Chapters 2, 3, 4, and 5 will provide additional introduction and background specific to the subject matter discussed therein.

Chapter 2

Numerical Techniques

2.1 Background

This chapter is intended to provide the reader with a better understanding of the numerical schemes employed in this thesis. The three most widely used numerical schemes are the boundary-element method (BEM), the finite-difference method (FDM), and the finite-element method (FEM). The BEM and FDM are both used in this thesis. This chapter will provide an in-depth explanation of the BEM and FDM, and an introduction to the FEM. Because boundary-element (BE) and finite-difference (FD) simulations are so different, the chapter also addresses the general strengths and weaknesses of each method. A general understanding of all three methods enables the reader to better understand some of their similarities and differences, and aids the reader in knowing which computational method is best for specific scenarios.

2.2 The Boundary Element Method

The BEM is unique because it only requires information on the boundary of the domain to compute field values within the domain, where the domain is simply the space over which the governing equation is defined. Much like Gauss's Theorem (or the divergence theorem), the BEM arrives at its fundamental equation after reducing a volume integral to a surface integral. In doing this, however, the fluid through which acoustic waves propagate is assumed to be homogeneous. Since the BEM only requires mathematical specification of the boundary of the domain, it is especially useful when considering problems in an unbounded domain. As long as the boundary itself is not infinite in nature, this method naturally handles problems that would otherwise require artificial infinite boundaries with imperfect absorbing boundary conditions.

The BEM has only recently been programmed in the time domain.¹ Consequently, most commercial packages program the BEM to solve the Kirchhoff-Helmholtz Integral Equation (KHIE), which restricts the problem to single-frequency, steady-state analysis. BEM packages also require that the continuous boundary surface [see Fig. 2.1(a)] be made discrete by segmenting it into a number of different nodes and elements [see Fig. 2.1(b)]. Nodes are discrete locations on the boundary (circles), and elements are the area between specified nodes.



FIG. 2.1. (a) A continuous boundary. (b) A discrete representation of the continuous boundary. In (b), nodes are indicated by the circles and elements are indicated by the straight lines.

Once the discrete problem is created, the mathematics of the continuous boundary must be discretized as well. The integral describing the continuous surface depicted in Fig. 2.1(a) becomes a sum of smaller integrals, where the region of integration for each smaller integral is over a single element. Thus, each straight line in Fig. 2.1(b) would be represented mathematically by an integral, and the sum of these element integrals would approximate the original continuous integral. The approximation improves as the discrete boundary better represents the continuous boundary with a higher discretization density.

Before discretization, the only unknown functions within the KHIE, pressure and its normal derivative, are continuous over the boundary. When these functions are specified by boundary conditions, it is then possible to solve the problem, assuming it can be done analytically. After discretization, however, the KHIE has been expanded mathematically. The general unknown functions are still pressure and its normal derivative, but their values cannot be obtained as continuous functions. Instead, both functions must be obtained at the specific nodal point of the discrete model. As in the continuous case, the problem can be solved once both functions are described along the boundary. Many times, both of these functions are not known along the entire boundary, resulting in many unknowns. Hence, the formulation for the BEM first creates enough equations such that both functions are defined along the entire boundary. Then information within the fluid of the domain can be calculated.

Several unique equations are created for each of the unknowns by evaluating the discretized KHIE, where each node is used as the field point (computational receiver) of the model. After an equation is formed for each point, a system of equations can be formed and the discrete KHIE can be solved through matrix analysis. Although the matrix only includes elements on the surface of the domain, each node from each element on the discrete surface will

interact with all the other nodal points on the model boundary. Mathematically, this results in a dense (full) matrix to correctly represent the acoustic interaction of each node with itself and with all the other nodes on the boundary.

Although the matrix created by the BEM is dense, the computational domain has been reduced to the boundary. As long as this reduction is significant, the savings in computation time is also significant. For instance, if the pressure field is desired from a flat plate that radiates in free space, the number of points needed to represent the fluid volume is much larger than the points needed to represent the boundary and the numerical simulation is likely computed faster with the BEM. However, if the pressure field is desired within a pipe, where the number of points needed to represent the boundary of the pipe is comparable to the points needed to represent the volume of fluid within the pipe, then the BEM is most likely slower than a different fluid-based simulation that does not require global interdependencies between all nodes.

2.2.1 Important Considerations

The purpose of this section is to suggest a few important considerations to those readers who are not familiar with numerical methods and expound on additional details of the BEM. Some of the mathematics will be addressed, insofar as needed, to explain a few mistakes commonly made when implementing the BEM. A few general aspects of the BEM are also discussed to help the reader understand more of the particular requirements for a given computation. For a rigorous development of the theory, the reader is referred to Refs. [2]-[7], which give sufficient treatment of the mathematics behind the BEM. References [2], [4], and [7] are most helpful, but require a substantial background in mathematics. Reference [6] is helpful

for a better understanding of computer implementation. The relevant mathematics in this thesis is based on those in Ref. [2].

2.2.1.1 Consideration 1: Nodes and Elements

The mathematics used in the BEM contains several summations, integrals, and iterative procedures. It often requires significant effort to sort out which sum or integral goes with a particular node or element. Thus, a brief explanation of the fundamental mathematics will assist in understanding later concepts.

The concept of a node only requires one to have a rudimentary exposure to mathematics. Suppose there exists a continuous function $f(x)$ defined for any x . One can graph a representation of $f(x)$ by plotting its values at discrete values of x . Discrete values of the x -axis *must* be chosen because it is impossible to input an infinite number of values on a continuous axis. Once the output values at those discrete points are known, the function is typically graphed by imposing the concepts of elements.

Figure 2.2 illustrates how a continuous function is created from nodes and elements. First, Fig. 2.2(a) shows the discrete values along the x -axis that are chosen as input values for $f(x)$. Next, Fig. 2.2(b) shows the output values of $f(x)$, indicated by the vertical displacement of each chosen point from Fig. 2.2(a). These values become the place holders for the overall shape of the function (nodes). The elements are created when a functional relationship is created between two nodes, indicated by the lines in Fig. 2.2(c). These lines, or elements, can have a linear relationship and appear as straight lines between nodes (as drawn), or they can have a non-linear relationship and the lines will include curvature between nodes.

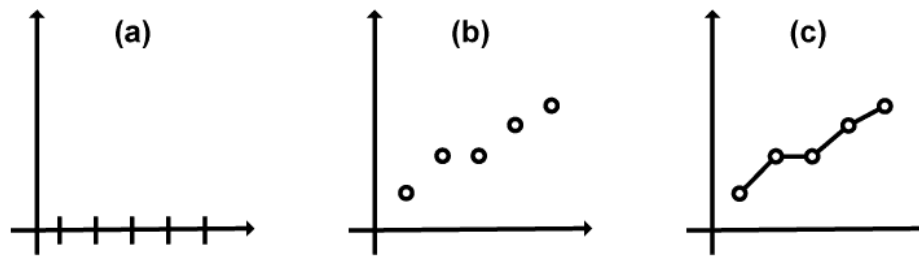


FIG. 2.2. (a) Chosen discrete x -values. (b) Output values of $f(x)$ at discrete x -values. (c) Relationships between nodes (elements/lines connecting nodes).

Elements are defined geometrically and functionally. The geometric requirements help the user understand how the discrete points, or nodes, of an element are grouped together. Geometric grouping happens in various ways. While nodes are usually found at the edges of each element, this is not a requirement. For simple problems with slowly-varying pressure fluctuations, a single node at the center of each element is all that is needed. The number of nodes also depends on how the functional relationship is defined. There is no reason to have several nodes if the pressure across a given element is assumed to be constant.

Elements are defined functionally in an attempt to recreate the continuous function $f(x)$ from the discrete values known at the nodal points. For example, if $f(x)$ varies linearly, then the functional values at each nodal point vary linearly and a straight line between contiguous nodes produces the least amount of error between the reconstructed function and the actual function $f(x)$. However, if $f(x)$ varies quadratically, then the reconstructed function is more accurate if it accounts for the curvature of the actual function. In this example, the function is known at the nodal values before an element's curvature is assigned; however, the BEM requires a mathematical description of the functional dependence between nodes *before* the values of the unknown function are solved at the nodal points. A linear relationship between contiguous nodes

is often sufficient as long as enough nodal points exist per functional wavelength. A computational rule of thumb suggests that the model contain at least six nodes per wavelength.⁸ However, more elements per wavelength are required if the boundary cannot be sufficiently represented.

The functional definition of an element is described mathematically by shaping functions, which are described in their most basic form on page 26 of Ref. [2]. Shaping functions are what create the lines or curves between the nodes illustrated in Fig. 2.2(c).

While attempting to understand some of the fundamentals of the BEM, it may initially seem unclear whether the BEM is solving the system at the nodes or over the elements. *Values of the unknown function are always solved at the nodal positions in the BEM.* The functional aspect of the elements is merely the shaping function. Thus, elements define the integrand and the area over which integration occurs via shaping functions.

2.2.1.2 Consideration 2: Matrix Values

When seeing the BEM for the first time, there is often confusion on how to build the system of equations created for matrix analysis. Although integration occurs over each element, sometimes these integrations are combined with other integrations from different elements per matrix value, which can be unintuitive at first glance. Thus, a brief explanation of how the matrix values are created will now be given.

The goal of the BEM is to solve the Kirchhoff-Helmholtz integral equation,

$$cu = \int_{\Gamma} (qu^* - uq^*)d\Gamma, \quad (2.1)$$

where c is a weighting function, u is the unknown scalar function (usually pressure), q is the normal derivative of u (usually normal velocity), Γ is the boundary, u^* is the free-space Green's function, and q^* is the normal derivative of the free-space Green's function. Once the problem is discretized into N elements, the continuous problem becomes

$$c_i u_i + \sum_{j=1}^N \int_{\Gamma_j} u q^* d\Gamma = \sum_{j=1}^N \int_{\Gamma_j} q u^* d\Gamma, \quad (2.2)$$

where i is the iteration index for the nodes, j is the iteration index for the elements, and Γ_j is the surface described by the j^{th} element {Equation (2.2) corresponds to Eq. (2.42) of Ref. [2]}. In order to solve Eq. (2.2), the shaping function $\phi(\xi)$ is introduced, which correlates the nodes across a given element—the surface of integration.

For illustrative purposes, consider Fig. 2.3, a two-dimensional problem, where each element has a node located at the ends of each element. This problem will be considered as the BE theory is developed.

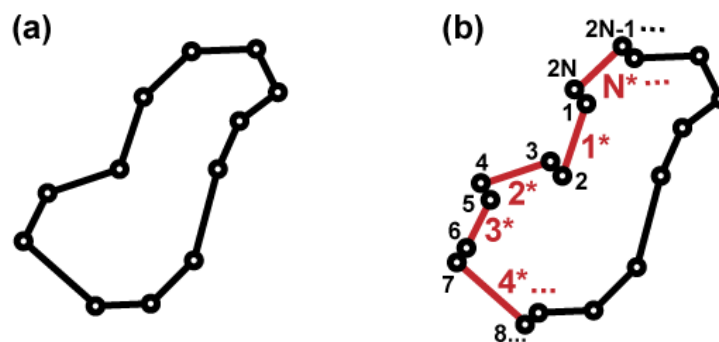


FIG. 2.3. (a) Geometry of a two-dimensional problem considered for Section 2.2.1.2. (b) Two-dimensional problem dissected into nodes and elements. Elements are indicated by the lines and starred (*) numbers. Nodes are indicated by the circles and regular numbers.

Mathematically, a typical integration over the j^{th} element is decomposed as

$$\int_{\Gamma_j} uq^* d\Gamma = \int_{\Gamma_j} (\phi_1 u_j^1 + \phi_2 u_j^2) q^* d\Gamma, \quad (2.3)$$

where the variables u_j^1 and u_j^2 are the nodal values of the unknown scalar function over the j^{th} element. Because u_j^1 and u_j^2 are evaluated at specific points on the surface, they are constants within the integration and may be factored out. Thus,

$$\begin{aligned} \int_{\Gamma_j} uq^* d\Gamma &= \int_{\Gamma_j} (\phi_1 u_j^1 + \phi_2 u_j^2) q^* d\Gamma, \\ &= u_j^1 \int_{\Gamma_j} \phi_1 q^* d\Gamma + u_j^2 \int_{\Gamma_j} \phi_2 q^* d\Gamma. \end{aligned} \quad (2.4)$$

Equation (2.4) was formulated for an arbitrary element. Thus, no matter what shape is considered, as long as the element is defined such that it has two nodes on each end, it consistently applies. This notation is slightly changed from Ref. [2]. Because the reference only considers the j^{th} element and doesn't formulate the entire matrix, u_j^1 and u_j^2 are respectively written as u_1 and u_2 .

When considering all of the elemental integrations necessary to solve the problem at its nodal locations, Ref. [2] gives the following equation:

$$c_i u_i + [\bar{H}_{i1} \quad \bar{H}_{i2} \quad \cdots \quad \bar{H}_{iN}] \begin{bmatrix} u_1 \\ u_2 \\ \vdots \\ u_N \end{bmatrix} = [\bar{G}_{i1} \quad \bar{G}_{i2} \quad \cdots \quad \bar{G}_{iN}] \begin{bmatrix} q_1 \\ q_2 \\ \vdots \\ q_N \end{bmatrix}. \quad (2.5)$$

The text only briefly mentions how \bar{H}_{ij} and \bar{G}_{ij} are constructed; however, it is imperative to understand how these matrices are constructed. For this example, and as is common in actual BE code, two elements share the same node. Hence, two integrations over two different elements

combine to create the matrix values \bar{H}_{ij} and \bar{G}_{ij} . Therefore, by expanding matrices \bar{H} and \bar{G} , Eq. (2.5) becomes

$$\begin{aligned} c_i u_i + u_1^1 h_{i1}^1 + u_1^2 h_{i1}^2 + u_2^1 h_{i2}^1 + u_2^2 h_{i2}^2 + \cdots + u_N^1 h_{iN}^1 + u_N^2 h_{iN}^2 \\ = q_1^1 g_{i1}^1 + q_1^2 g_{i1}^2 + q_2^1 g_{i2}^1 + q_2^2 g_{i2}^2 + \cdots + q_N^1 g_{iN}^1 + q_N^2 g_{iN}^2, \end{aligned} \quad (2.6)$$

where

$$h_{ij}^k = \int_{\Gamma_j} \phi_k q^* d\Gamma, \quad (2.7)$$

and

$$g_{ij}^k = \int_{\Gamma_j} \phi_k u^* d\Gamma. \quad (2.8)$$

The index k ranges from one to the total number of shaping functions (also the number of nodes used to define each element), which is two in our example.

Although the model only consists of N unknowns (nodes), Eq. (2.6) contains $2N$ unknowns since each element is integrated separately and the nodes are temporarily separated. The left-hand side of Eq. (2.6) is simplified since u is a scalar function and the spatial location for u_j^2 is the same as u_{j+1}^1 . Hence, these variables are identical. We then combine them and write them as u_i , where i is the nodal index. The same simplification is done with values q_j^2 and q_{j+1}^1 , but only if the elements are parallel. This is because the function q is a vector. Although the spatial location for both nodal values is identical, their normal vector may point in different directions and thus produce different values.

No two contiguous elements have the same normal in this example. Thus, the \bar{G} matrix cannot be simplified. Once the preceding simplifications are applied to Eq. (2.6) and an Eq.

(2.5) has been created for all N nodes as the reception point ($c_i u_i$), the following system of linear equations is formed:

$$\begin{aligned} & \begin{bmatrix} c_1 u_1 \\ c_2 u_2 \\ \vdots \\ c_N u_N \end{bmatrix} + \begin{bmatrix} h_{11}^1 + h_{1N}^2 & h_{11}^2 + h_{12}^1 & \cdots & h_{1N-1}^2 + h_{1N}^1 \\ h_{21}^1 + h_{2N}^2 & h_{21}^2 + h_{22}^1 & \cdots & h_{2N-1}^2 + h_{2N}^1 \\ \vdots & \vdots & \ddots & \vdots \\ h_{N1}^1 + h_{NN}^2 & h_{N1}^2 + h_{N2}^1 & \cdots & h_{NN-1}^2 + h_{NN}^1 \end{bmatrix} \begin{bmatrix} u_1 \\ u_2 \\ \vdots \\ u_N \end{bmatrix} \\ &= \begin{bmatrix} g_{11}^1 & g_{11}^2 & g_{12}^1 & g_{12}^2 & \cdots & g_{1N-1}^2 & g_{1N}^1 & g_{1N}^2 \\ g_{21}^1 & g_{21}^2 & g_{22}^1 & g_{22}^2 & \cdots & g_{2N-1}^2 & g_{2N}^1 & g_{2N}^2 \\ \vdots & \vdots & \vdots & \vdots & \ddots & \vdots & \vdots & \vdots \\ g_{N1}^1 & g_{N1}^2 & g_{N2}^1 & g_{N2}^2 & \cdots & g_{NN-1}^2 & g_{NN}^1 & g_{NN}^2 \end{bmatrix} \begin{bmatrix} q_1^1 \\ q_1^2 \\ q_2^1 \\ \vdots \\ q_{N-1}^1 \\ q_N^1 \\ q_N^2 \end{bmatrix}, \end{aligned} \quad (2.9)$$

where the matrix including all of the h_{ij}^k elements is size $N \times N$, and the matrix including all of the g_{ij}^k elements is size $N \times 2N$.

Equation (2.9) may be insufficient to solve the entire system. This depends on the specified boundary conditions. If the boundary condition prescribes the nodal values of q , then only the unknown nodal values for u remain and N equations are required to solve the system. In this case, Eq. (2.9) is sufficient. However, if the boundary condition prescribes the nodal values of u , then the system contains $2N$ unknowns and Eq. (2.9) must include N more equations in the system before a solution is acquired.

Assuming one formulates and solves Eq. (2.9) correctly, the unknown functions u_i and q_j^k (pressure and normal velocity) are then known on the boundary. Once these values are determined, both functions are used to calculate their respective values at any point on or within the domain.

2.2.1.3 Consideration 3: Absorptive Boundary Conditions

The BEM is, as its name suggests, a numerical scheme which requires knowledge of the entire boundary to infer a solution within the fluid. Many times, this approach reduces the size of a problem that radiates to infinity. However, if the boundary must also extend to infinity, then the BEM requires an infinite amount of nodes and elements to construct the problem computationally and is therefore ill-posed. The remedy is an artificial infinite boundary that imitates continuous radiation to infinity by imposing some radiation condition on the boundary (i.e., the Sommerfeld radiation condition⁹). The BEM does this by assigning pressure, normal velocity, or a combination of both along the boundaries of the model. Because the BEM does not have nodal points within the fluid, the absorptive boundary condition must be constructed at each nodal point analytically. If that cannot be done using these quantities, the BEM cannot create the appropriate boundary condition and the problem must be solved using a different method. The following example will illustrate why this process can be difficult for the BEM.

Suppose that we desire to model a semi-infinite-length pipe in steady state. The pipe model cannot reasonably extend to infinity, so it is truncated. However, due to truncation, an acoustic discontinuity is necessarily introduced into the model. To prevent reflection from the discontinuity, an artificial infinite boundary is created. With the appropriate radiation condition prescribed at this boundary, the simulation behaves as if the wavefront propagates continuously. Appropriate prescription of this boundary condition at each nodal point of the artificial infinite boundary requires an analytical knowledge of the amplitude and phase characteristics of each mode that propagates to the artificial infinite boundary. If we further assume that the excitation source is different from the pipe, such that the relationship between propagating eigenfunctions

is unknown, then the boundary condition cannot be correctly prescribed. Thus, correct prescription of the boundary condition at the artificial infinite boundary requires an analytical definition of the excitation source.

The problem described above is specific to steady-state problems. The author is uncertain as to whether a similar problem exists in the time-domain approach of the BEM since the governing equation is different. It may be that a different approach is able to better describe the artificial infinite boundary.

2.3 The Finite Difference Method

The next numerical scheme to discuss is the FDM. Unlike the BEM, the FDM discretizes the fluid, as well as the boundary. Although discretization of the fluid region adds a considerable number of grid points to the model, the field value on each grid point does not depend on the field values on all other grid points, which is the case for the BEM. Instead, the computation of a field value at a particular grid point only depends on a small set of field values on surrounding nodes, or grid points. This difference in nodal dependence is manifest in the matrix associated with each method. While the matrix obtained in the BEM is full, the matrix obtained by the FDM is banded, or sparse.

Another important difference between the BEM and the FDM is that the BEM requires an integral representation of the governing differential equations, which is commonly the Kirchhoff-Helmholtz integral equation, approximated using all the discretization points on the boundary. Conversely, the FDM is governed by partial differential equations. Each grid is defined analytically, and partial derivatives are approximated by a linear combination of truncated Taylor

series expansions of surrounding grid points. The FDM method is very intuitive and is probably the easiest method to grasp of the three being considered. Several distinct differential equations can be approximated and solved quickly. Both time-domain and steady-state analysis are computable. The option for time-domain analysis is of particular interest since it is not readily available in many BE software packages.

Since the FDM is easy to code, its use is not restricted to a commercial package. Two-dimensional models run efficiently on an average computer, but most three-dimensional models easily become too large computationally and may require the use of a super-computer, taking days to compute a single scenario. Since an attractive possibility for using this method is to compute several scenarios quickly, computational speed is a priority. Thus, all three-dimensional models treated in this thesis are cylindrically symmetric such that the computational domain of each model reduces to a two-dimensional cross section. Although this restriction is not a big disadvantage, it does limit the computational possibilities of the FDM by impeding research on any three-dimensional models that are not axisymmetric. A general method for approximating derivatives of any order is shown to help the reader better understand this numerical scheme.

2.3.1 Approximating Derivatives via Taylor Series Expansions

In order for a function to be expressed as a Taylor series, the function and all of its derivatives must be defined.¹⁰ If the same function is expanded multiple times—about different points—then some linear combination of these expansions may be found that approximates a certain-order derivative. The accuracy of the approximation will depend on how many terms, other than the desired derivative, are set to zero when all of the expansions are aggregated.¹¹ The

number of nodes used to create the approximate derivative also affects the accuracy. Though not always true, generally the more points used in the approximation, the easier it is to create. The following example illustrates a general method for approximating a function's derivatives using Taylor series expansions. For ease, derivatives are notated as a subscript of the function (i.e.

$$\frac{d}{dx}u(x) = u_x).$$

2.3.1.1 Example: Approximating a First Derivative

Assume that five points, spaced a distance h apart, are used to approximate the first derivative of a function $u(x)$. The initial equation may be written as

$$u_x = \alpha u(x - 2h) + \beta u(x - h) + \gamma u(x) + \delta u(x + h) + \phi u(x + 2h), \quad (2.10)$$

where α , β , γ , δ , and ϕ are the unknown coefficients that need to be solved. If the desired accuracy is of order h^4 , then each Taylor series expansion is truncated after the fifth term. After expansion, the functions in Eq. (2.10) become

$$\begin{aligned} u(x - 2h) &= u(x) - 2hu_x + (2h)^2u_{xx} - (2h)^3u_{xxx} + (2h)^4u_{xxxx}, \\ u(x - h) &= u(x) - hu_x + h^2u_{xx} - h^3u_{xxx} + h^4u_{xxxx}, \\ u(x) &= u(x), \\ u(x + h) &= u(x) + hu_x + h^2u_{xx} + h^3u_{xxx} + h^4u_{xxxx}, \\ u(x + 2h) &= u(x) + 2hu_x + (2h)^2u_{xx} + (2h)^3u_{xxx} + (2h)^4u_{xxxx}. \end{aligned} \quad (2.11)$$

Determining the coefficients α , β , γ , δ , and ϕ is done by forming a system of equations with the desired aggregate for each derivative (or term in each expansion) indicated on the right-hand side. Since the goal is to solve for u_x and cancel all other terms with error less than h^4 , no

contributions are desired from $u(x)$, u_{xx} , u_{xxx} , and u_{xxxx} . This is indicated by the right-hand side of the following equation:

$$\begin{bmatrix} 1 & 1 & 1 & 1 & 1 \\ -(2h) & -h & 0 & h & 2h \\ (2h)^2 & h^2 & 0 & h^2 & (2h)^2 \\ -(2h)^3 & -h^3 & 0 & h^3 & (2h)^3 \\ (2h)^4 & h^4 & 0 & h^4 & (2h)^4 \end{bmatrix} \begin{bmatrix} \alpha \\ \beta \\ \gamma \\ \delta \\ \phi \end{bmatrix} = \begin{bmatrix} 0 \\ 1 \\ 0 \\ 0 \\ 0 \end{bmatrix}. \quad (2.12)$$

Each column in the matrix contains the coefficients of each expansion given in Eq. (2.11). This system of equations is solved by multiplying both sides by the inverse of the 5x5 matrix, after which the coefficients are solved:

$$\begin{bmatrix} \alpha \\ \beta \\ \gamma \\ \delta \\ \phi \end{bmatrix} = \begin{bmatrix} 1/12h \\ -8/12h \\ 0 \\ 8/12h \\ -1/12h \end{bmatrix}. \quad (2.13)$$

Substitution of the coefficients into Eq. (2.10) gives

$$u_x + O(h^4) = \frac{u(x-2h) - 8u(x-h) + 8u(x+h) - u(x+2h)}{12h}, \quad (2.14)$$

where the error of the approximation is grouped in the term $O(h^4)$. Thus, an approximation for u_x with error of order h^4 is described by Eq. (2.14).

An alternate approximation for u_x can be derived using only points to the right, or only points to the left. The coefficients result in different values, but the end result is the same. The coefficients for any given scenario are easily computed once the order of accuracy and number of points are chosen. Additional examples of deriving coefficients generally are given in Ref. [11].

2.4 The Finite Element Method

The FEM method is similar to the BEM in that many people have created packages that are efficient and usable; however, the concept behind the FEM is more akin to the FDM. Like many instances of the FDM, each field value being computed in the FEM only depends on local changes from field values at surrounding grid points. As seen before, this effect results in a sparse matrix which is much faster to compute than a full matrix. However, the FEM is based on discretization of the fluid and the boundary by representing the operators in the governing differential equation and matrices. Many times, these matrices are thought of as describing the mass and spring components of each grid point.¹²

Regardless of its similarities to the FDM, the FEM does not have the stringent mesh requirements seen in the FDM. It is free to have irregularly-spaced and non-analytically defined meshes. Thus, the FEM is very popular for applications in which geometries are irregular, or in which the mesh cannot easily be mapped into an analytical domain. These meshes are used for both transient and steady-state analysis and allow the coupling of multiple domains.

Because this method is not used in any of the simulations performed in this thesis, an in-depth explanation of this method is not given. However, a fairly rigorous treatment is given in Refs. [12] and [13], for the interested reader.

2.5 Selection of an Appropriate Computational Method

With a reasonable understanding of the three numerical methods, a simple description of their strong points may help the reader to better understand where each method is best employed.

The BEM generally performs well when the domain of the problem is infinite or semi-infinite in nature. Because the numerical integration is only a surface integral, the fluid needs to be homogeneous. The BEM also performs faster than other numerical schemes when the amount of points needed to define the fluid is significantly larger than the number of points required to define the boundary. Otherwise, computation time may be comparatively higher for the BEM. Although the commercial BE package used for this thesis does not include time-domain analysis, this is starting to become available and will not be a future restriction for this method. Currently, however, most BE software only allows steady-state, single-frequency analysis. The BEM also has difficulty imposing absorbing boundary conditions (i.e., an anechoic termination) when models need to account for higher-order mode propagation and when an appropriate radiation condition cannot be imposed. Simple absorbing boundary conditions only work when the excitation frequency is well below the cutoff frequency of the first higher-order mode of the system in the case of wave propagation in pipes. In this manner the absorptive boundary condition is constant spatially, and can be predefined, as is required, before simulation.

The FDM requires discretization of the fluid, instead of just the boundary, and works best with enclosed boundaries. However, the FDM can be used to simulate an infinite domain by creating artificial infinite boundaries where infinite radiation is imitated. The FDM is a highly intuitive method and is versatile due to its adaptable manner of approximating derivatives. Its programming is straightforward and does not require a commercial package to perform meaningful computations. The FDM requires an analytically defined grid and does not perform well with irregularly shaped geometries. However, this restriction is somewhat circumvented when using generalized curvilinear coordinates to define irregular geometries. Since any

differential equation can be approximated by Taylor series expansions, time-domain analysis is as easy to simulate as steady-state analysis with the FDM.

The FEM is most similar to the FDM. It requires discretization of the fluid, but does not require an analytically defined mesh. It is readily available in many commercial packages and seems versatile in nature. This package was not used to simulate any of the problems analyzed in this thesis. However, it is still a plausible scheme that can provide time-domain analysis of very complex geometries, which is used to simulate many models of compression-driver and horn systems.

Chapter 3

Transient Analysis from Finite-Length Pipes

3.1 Background

Wave propagation through and from a pipe is a widely studied field in acoustics. Many researchers interested in turbofans, ventilation systems, mufflers, exhaust pipes, loudspeakers, etc. use the analytical analysis of pipes as a first step to better understand their more complicated system of interest. The initial research on wave propagation through pipes was performed by Lord Rayleigh,¹⁴ who analytically considered infinite-length pipes in steady state. His methods were later expanded upon by Pearson,¹⁵ who gave an analytical treatment of the dispersive nature of transient signals in infinite-length pipes. Pearson's work was confirmed experimentally by Proud *et al.*,¹⁶ who used water-filled rectangular ducts to study the dispersive effects of transient signals. Baumeister¹⁷ produced similar results numerically.

After the establishment of infinite-pipe theory, analytical progress was made with finite-length pipes.¹⁸⁻²⁰ Probably the most recognized is the work done by Levine and Schwinger.¹⁸ By using Green's functions, their work rigorously defined the radiation from an unbaffled, finite-length pipe in steady state. Their work has been furthered in different ways to produce more uniform convergence between the pipe domain and the half-space domain by using alternate integral equations,¹⁹ but the solution remains more or less the same. An area of possible improvement in the solution was introduced by Amir and Matzner.²⁰ They used different basis functions within the pipe and in doing so improved the mathematical disparity of the pipe domain and the half-space domain by requiring fewer basis functions to obtain an accurate approximation.

Though analytical treatment of propagation through finite-length pipes and subsequent radiation has progressed general understanding, numerical work has helped to more accurately simulate this problem and allow for a better understanding of its results. Both the finite-difference method (FDM) and finite-element method (FEM) were first used to solve steady-state problems within finite-length pipes.²¹⁻²⁴ Because these methods required large matrices, early use was restricted to smaller computational domains (less grid points) and lower frequencies. To reduce the computational burden of the steady-state approach, Baumeister introduced a time domain method using FD techniques.¹⁷ If the simulation ran long enough, the transient solution would decay to nothing and the steady-state solution would therefore be obtained without matrices. While this work helped to reduce computation time, problems from the interaction of the artificial infinite boundary with higher-order modes could not be considered due to an ill-defined boundary condition at the pipe exit.²⁵ A comprehensive review of the use of numerical methods in duct acoustics was given in Ref. [25].

While many of these authors have numerically obtained solutions for sound radiation from a finite-length pipe (baffled and/or unbaffled), their results are either only for steady-state conditions or using transient signals (a sine wave modulated by a Heaviside function at $t = 0$) to obtain the steady state.²¹⁻²⁴ Thus, transient effects within the pipe were not isolated sufficiently to independently observe their effects. This concept, however, may be particularly relevant to audio transducer applications as many signals reproduced by them are generally innately transient. Dalmont *et al.* used both the FDM and BEM to analyze subsequent radiation for several different pipe-like geometries (with and without a baffle) in steady state.²⁴ Tsubakishita *et al.* did similar work to Dalmont *et al.* in terms of steady-state analysis, but their approach was more accurate as they approximated the governing differential equations to fourth-order accuracy.

Others who considered wave propagation through pipe-like structures for short-duration transient signal were Noreland²⁶ and Davis.²⁷ Both of their research used the idea of transmission lines to model the excitation source. However, the transmission-line method restricts wave propagation to the plane-wave mode. Since higher-order modes are an important part of this work, this approach is not appropriate for the problems considered in this article. Stepanishen and Tougas also published a paper on pulse-like transient radiation from a finite-length pipe.²⁸ They gave an in-depth analytical description of acoustic wave propagation and radiation from a finite-length pipe due to short-duration transient signals. However, a one-to-one correspondence of pipe modes to half-space modes was used as a necessary simplification of their approach. One of their key findings was that radiation from higher-order pipe modes showed no on-axis radiation. By using numerical methods to evaluate this problem, both domains are inherently coupled to one another and the accuracy of their simplification may be observed.

The numerical simulations reported in this chapter incorporate a leapfrog FDM for evaluation of wave propagation for short-duration transient signals. The pipe is made rigid and the case of no mean flow is considered as this is more characteristic of an audio transducer. Curvilinear coordinates are used to generate smooth grids that do not need to be truncated before the half-space domain, eliminating the need for a problematic impedance boundary condition at the pipe exit.¹⁷ As considered by Stepanishen and Tougas, several higher-order modes are independently excited here in an initially quiescent field by single-cycle, gated sine waves. Propagation through and from the pipe are simulated and their subsequent radiation patterns are presented and discussed. Some of the problems created from using such short-duration transient signals in the simulation are also addressed.

3.2 The Mathematical Model

3.2.1 The Physical Problem

Transient radiation is studied from a finite-length pipe mounted to an infinite-length baffle. At time $t = 0$, the fluid is excited at the end of the pipe not mounted to the baffle. The excitation signal is defined as either a gated, single-cycle sine wave. Once excited, an acoustic wave propagates through the pipe and eventually radiates to infinity.

Inside the pipe and in the half plane outside the pipe, the sound pressure is mathematically modeled by the wave equation, where symmetry around the polar ϕ -axis is assumed. The wave equation expressed in cylindrical coordinates is

$$\frac{1}{r} \frac{\partial}{\partial r} \left(r \frac{\partial p}{\partial r} \right) + \frac{1}{r^2} \frac{\partial^2 p}{\partial \phi^2} + \frac{\partial^2 p}{\partial z^2} = \frac{1}{c^2} \frac{\partial^2 p}{\partial t^2}, \quad (3.1)$$

where p is pressure, c is the acoustic sound speed. By imposing cylindrical symmetry,

$$\frac{\partial p}{\partial \phi} = 0,$$

and through expansion of the first term, Eq. (3.1) becomes

$$\frac{\partial^2 p}{\partial r^2} + \frac{1}{r} \frac{\partial p}{\partial r} + \frac{\partial^2 p}{\partial z^2} = \frac{1}{c^2} \frac{\partial^2 p}{\partial t^2}. \quad (3.2)$$

Also, the pipe and baffle have rigid walls. An illustration of the physical problem is given in Fig.

3.1. The right-hand illustration in depicts the physical domain of propagation \mathcal{D} . Its boundaries

$C_1 \cup C_2 \cup C_3 \cup C_4$ are also illustrated.

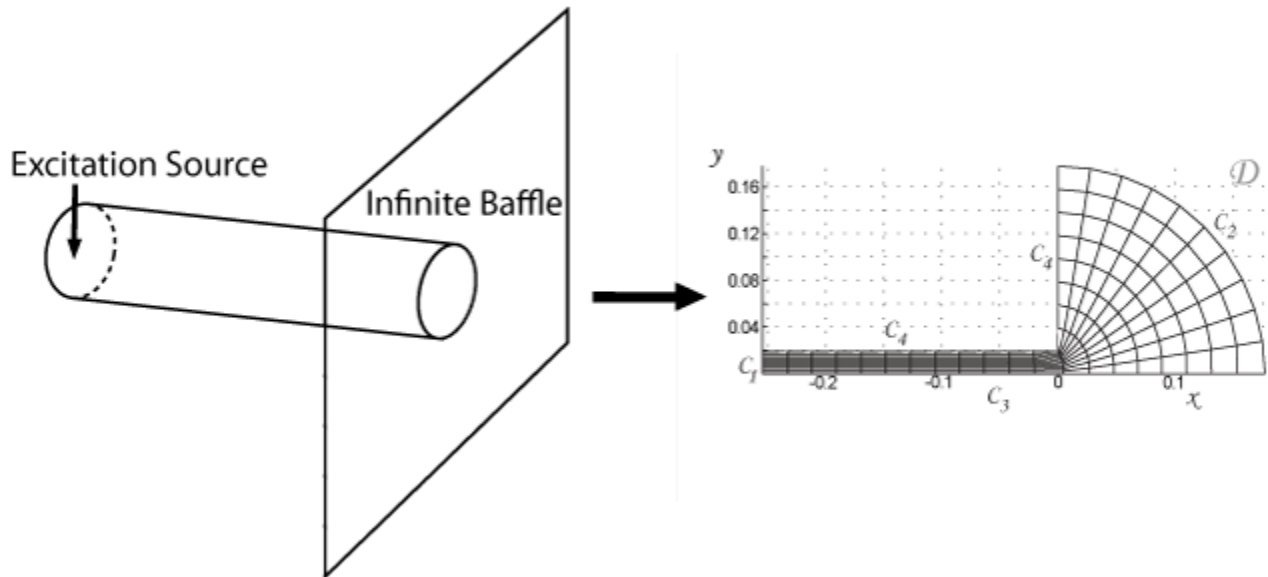


FIG. 3.1. Physical domain used to study transient radiation from a finite-length pipe.

The boundary condition at C_4 is modeling a rigid condition for both the pipe wall and the infinite baffle. At C_3 , the interface conditions,

$$p(0^+, z, t) = p(0^-, z, t), \quad (3.3)$$

$$\frac{\partial}{\partial r} p(0^+, z, t) = \frac{\partial}{\partial r} p(0^-, z, t), \quad (3.4)$$

combined with the boundary condition leads to

$$\frac{\partial}{\partial r} p(0, z, t) = 0. \quad (3.5)$$

The condition on C_1 is defined by the nature of the excitation at this end of the pipe. It is assumed that the pressure field is initially quiescent. Also, the mathematical description of the outgoing wave at infinity is through the well-known Sommerfeld radiation condition, given by $p_t + cp_r \rightarrow 0$ as $r \rightarrow \infty$, where the subscripts t and r denote derivatives in time and space, respectively. This Initial Boundary Value Problem (IBVP) is solved numerically for p using FD in generalized curvilinear coordinates to account for irregular geometries. For computational reasons, a truncation of the infinite half-plane to the right of the pipe is necessary. Thus, the boundary C_2 in Fig. 3.1 corresponds to an artificial infinite boundary. This requires an introduction of an absorbing condition at C_2 instead of the Sommerfeld radiation condition. This condition should be such that there are no spurious reflections at the boundary. In this thesis, a condition, $p_t + cp_r + \frac{c}{2r}p \rightarrow 0$, as $r \rightarrow \infty$ of $\mathcal{O}(1/r^{5/2})$ is used. A complete review of absorbing boundary conditions is found in Refs. [29]-[30]. The IBVP in complete form is written as

$$\frac{1}{c^2} p(r, z, t)_{tt} = p_{rr} + \frac{1}{r} p_r + p_{zz}, \quad (r, z) \in \mathcal{D}, \quad t > 0, \quad (3.6)$$

$$\frac{\partial}{\partial n} p(r, z, t) = 0 \quad (r, z) \in C_4 \cup C_3, \quad (3.7)$$

$$\frac{\partial}{\partial n} p(r, z, t) = \begin{cases} -\rho_0 \hat{a}(r, t), & 0 \leq t \leq T_d, \\ 0, & \text{otherwise,} \end{cases} \quad (r, z) \in C_1, \quad (3.8)$$

$$p_t + cp_r + \frac{c}{2r} p = 0, \quad (r, z) \in C_2, \quad (3.9)$$

$$p(r, z, 0) = 0 \quad \text{and} \quad p_t(r, z, 0) = 0, \quad (r, z) \in \mathcal{D}. \quad (3.10)$$

3.2.2 The Physical Problem in Generalized Curvilinear Coordinates

Since this problem can only be solved analytically for very few cases, where the geometry of the pipe and the surrounding fluid can be described in separable coordinates (Cartesian, cylindrical, etc.), the IBVP [Eqs. (3.6)-(3.10)] will be numerically solved. For this purpose, it is first written in terms of generalized curvilinear coordinates. Much of the work done in generalized curvilinear coordinates (ξ and η) translates to Cartesian coordinates (x and y), it is desirable to write the IBVP in terms of x and y . Since the wave equation no longer depends on ϕ , the variables r and z are easily identified with y and x , respectively. Thus, $y = r$, $x = z$, and Eq. (3.6) can be written as

$$\frac{\partial^2 p}{\partial y^2} + \frac{1}{y} \frac{\partial p}{\partial y} + \frac{\partial^2 p}{\partial x^2} = \frac{1}{c^2} \frac{\partial^2 p}{\partial t^2}, \quad (3.11)$$

where p is now a function of x , y , and t . Figure 3.2 illustrates how the coordinate systems identify with one another.

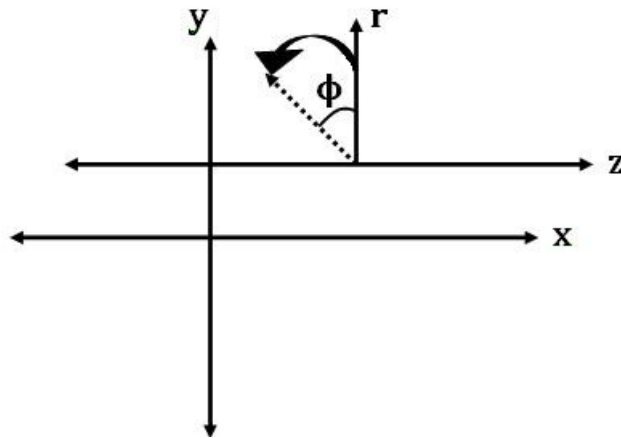


FIG. 3.2. Pictorial relationship between cylindrical and Cartesian coordinates.

The change to curvilinear coordinates can be mathematically described by a transformation between generalized curvilinear coordinates (ξ, η) and Cartesian coordinates (x, y) . Figure 3.3 pictorially describes this transformation $T: \mathcal{D}' \rightarrow \mathcal{D}$, defined by $x = x(\xi, \eta)$ and $y = y(\xi, \eta)$ from a rectangular region \mathcal{D}' called the computational domain to the plane region \mathcal{D} called physical domain.

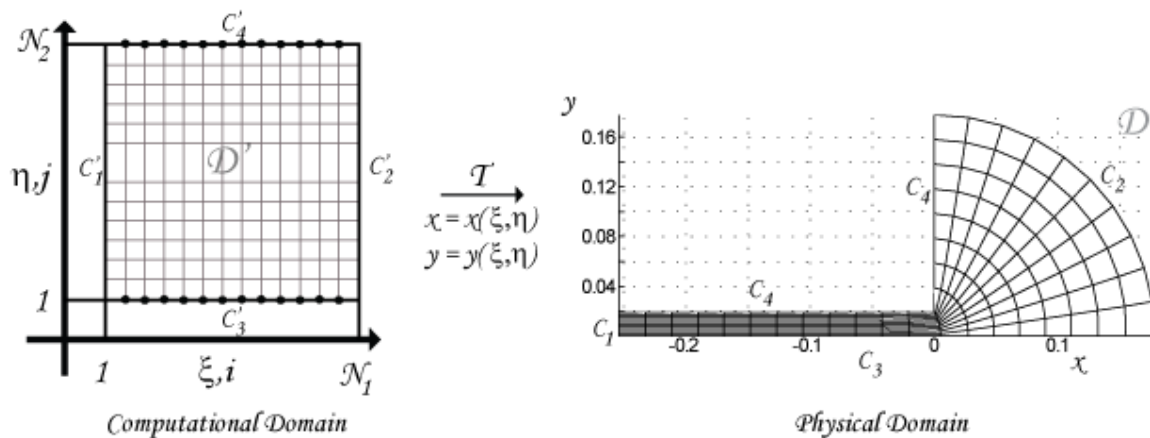


FIG. 3.3. Transformation used in the generation of boundary conforming coordinates.

As a result, the pressure is written in terms of curvilinear coordinates as $p(\xi, \eta) = p(x(\xi, \eta), y(\xi, \eta))$. Moreover, the wave equation expressed in Eq. (3.11) transforms into

$$\begin{aligned} & \frac{1}{J^2} (\alpha p_{\xi\xi} - 2\beta p_{\xi\eta} + \gamma p_{\eta\eta}) + \frac{1}{J^3} (\alpha y_{\xi\xi} - 2\beta y_{\xi\eta} + \gamma y_{\eta\eta}) (x_{\eta} p_{\xi} - x_{\xi} p_{\eta}) \dots \\ & + \frac{1}{J^3} (\alpha x_{\xi\xi} - 2\beta x_{\xi\eta} + \gamma x_{\eta\eta}) (y_{\xi} p_{\eta} - y_{\eta} p_{\xi}) \dots \\ & + \frac{1}{yJ} (x_{\xi} p_{\eta} - x_{\eta} p_{\xi}) = \frac{1}{c^2} p_{tt}, \end{aligned} \quad (3.12)$$

in generalized curvilinear coordinates. Partial derivatives are denoted as subscripts and $J = x_{\xi} y_{\eta} - x_{\eta} y_{\xi}$ corresponds to the Jacobian of the transformation. For completeness, a derivation of Eq. (3.12) follows. Considering the inverse transformation \mathcal{T}^{-1} , pressure p can be expressed as

$$p(x, y) = p(\xi(x, y), \eta(x, y)). \quad (3.13)$$

Then, by using the chain rule

$$\begin{aligned} \frac{\partial^2 p}{\partial y^2} &= \frac{\partial}{\partial y} (p_{\xi} \xi_y + p_{\eta} \eta_y) \\ &= p_{\xi\xi} \xi_y^2 + p_{\xi\eta} \xi_y \eta_y + p_{\xi} \xi_{yy} + p_{\eta\eta} \eta_y^2 + p_{\eta\xi} \eta_y \xi_y + p_{\eta} \eta_{yy}, \end{aligned} \quad (3.14)$$

$$\frac{1}{y} \frac{\partial p}{\partial y} = \frac{1}{y} (p_{\xi} \xi_y + p_{\eta} \eta_y), \quad (3.15)$$

and

$$\frac{\partial^2 p}{\partial x^2} = p_{\xi\xi} \xi_x^2 + p_{\xi\eta} \xi_x \eta_x + p_{\xi} \xi_{xx} + p_{\eta\eta} \eta_x^2 + p_{\eta\xi} \eta_x \xi_x + p_{\eta} \eta_{xx}. \quad (3.16)$$

Substitution of Eqs. (3.14)-(3.16) into Eq. (3.12) produces

$$\begin{aligned}
& p_{\xi\xi}(\xi_x^2 + \xi_y^2) + p_{\eta\eta}(\eta_x^2 + \eta_y^2) + 2p_{\xi\eta}(\xi_x\eta_x + \xi_y\eta_y) + p_{\xi}(\xi_{xx} + \xi_{yy}) \dots \\
& + p_{\eta}(\eta_{xx} + \eta_{yy}) + \frac{1}{y}(p_{\xi}\xi_y + p_{\eta}\eta_y) = \frac{1}{c^2} \frac{\partial^2 p}{\partial t^2}.
\end{aligned} \tag{3.17}$$

This equation is not a sufficient stopping point since derivatives are expressed in terms of both coordinate systems. In order to express Eq. (3.17) in a single coordinate system, a relationship between first order derivatives in both coordinate systems must be established. Returning to the definition of the transformation, coordinates x and y are expressed as

$$x = x(\xi(x, y), \eta(x, y)), \tag{3.18}$$

$$y = y(\xi(x, y), \eta(x, y)). \tag{3.19}$$

Taking a partial derivative of x in Eqs. (3.18) and (3.19) produces

$$1 = x_{\xi}\xi_x + x_{\eta}\eta_x, \tag{3.20}$$

$$0 = y_{\xi}\xi_x + y_{\eta}\eta_x. \tag{3.21}$$

Writing Eqs. (3.20) and (3.21) in matrix form gives

$$\begin{bmatrix} x_{\xi} & x_{\eta} \\ y_{\xi} & y_{\eta} \end{bmatrix} \begin{bmatrix} \xi_x \\ \eta_x \end{bmatrix} = \begin{bmatrix} 1 \\ 0 \end{bmatrix}. \tag{3.22}$$

If the same process is repeated by taking a partial derivative with respect to y , the resulting matrix changes to

$$\begin{bmatrix} x_{\xi} & x_{\eta} \\ y_{\xi} & y_{\eta} \end{bmatrix} \begin{bmatrix} \xi_y \\ \eta_y \end{bmatrix} = \begin{bmatrix} 0 \\ 1 \end{bmatrix}. \tag{3.23}$$

Combining these systems of equations produces

$$\begin{bmatrix} x_{\xi} & x_{\eta} \\ y_{\xi} & y_{\eta} \end{bmatrix} \begin{bmatrix} \xi_x & \xi_y \\ \eta_x & \eta_y \end{bmatrix} = \begin{bmatrix} 1 & 0 \\ 0 & 1 \end{bmatrix}, \tag{3.24}$$

where the right-hand side of Eq. (3.24) is the identity matrix. Since the product of the two matrices on the left-hand side of Eq. (3.24) equals the identity matrix, one matrix is the other's inverse.

Relationships of the first-order derivatives of both coordinate systems can be obtained from Eq. (3.24). The inverse of the left-most matrix in Eq. (3.24) is given by

$$\frac{1}{J} \begin{bmatrix} y_\eta & -x_\eta \\ -y_\xi & x_\xi \end{bmatrix}.$$

Therefore,

$$\frac{1}{J} \begin{bmatrix} y_\eta & -x_\eta \\ -y_\xi & x_\xi \end{bmatrix} = \begin{bmatrix} \xi_x & \xi_y \\ \eta_x & \eta_y \end{bmatrix}. \quad (3.25)$$

Term by term from Eq. (3.25), the following relationships hold between first derivatives of the two coordinate systems:

$$\begin{aligned} \xi_x &= \frac{y_\eta}{J}, & \xi_y &= -\frac{x_\eta}{J}, \\ \eta_x &= -\frac{y_\xi}{J}, & \eta_y &= \frac{x_\xi}{J}. \end{aligned}$$

A similar procedure can also relate the two coordinate systems for second-order derivatives. These relationships are given as

$$\begin{aligned} \xi_{xx} &= \frac{Ay_\eta - Bx_\eta}{J^3}, & \xi_{yy} &= \frac{Cy_\eta - Dx_\eta}{J^3}, \\ \eta_{xx} &= \frac{Bx_\xi - Ay_\xi}{J^3}, & \eta_{yy} &= \frac{Dx_\xi - Cy_\xi}{J^3}, \end{aligned}$$

where

$$\begin{aligned} A &\equiv -(x_{\xi\xi}y_\eta^2 - 2x_{\xi\eta}y_\xi y_\eta + x_{\eta\eta}y_\xi^2), & C &\equiv -(x_{\xi\xi}x_\eta^2 - 2x_{\xi\eta}x_\xi x_\eta + x_{\eta\eta}x_\xi^2), \\ B &\equiv -(y_{\xi\xi}y_\eta^2 - 2y_{\xi\eta}y_\xi y_\eta + y_{\eta\eta}y_\xi^2), & D &\equiv -(y_{\xi\xi}x_\eta^2 - 2y_{\xi\eta}x_\xi x_\eta + y_{\eta\eta}x_\xi^2). \end{aligned}$$

After some lengthy algebraic work involving substitution of $\xi_x, \xi_{xx}, \eta_x, \eta_{xx}, \xi_y, \xi_{yy}, \eta_y,$ and η_{yy} , it can be shown that the wave equation, Eq. (3.12), can be written as

$$\begin{aligned} & \frac{1}{J^2}(\alpha p_{\xi\xi} - 2\beta p_{\xi\eta} + \gamma p_{\eta\eta}) + \frac{1}{J^3}(\alpha y_{\xi\xi} - 2\beta y_{\xi\eta} + \gamma y_{\eta\eta})(x_\eta p_\xi - x_\xi p_\eta) \dots \\ & + \frac{1}{J^3}(\alpha x_{\xi\xi} - 2\beta x_{\xi\eta} + \gamma x_{\eta\eta})(y_\xi p_\eta - y_\eta p_\xi) \dots \\ & + \frac{1}{yJ}(x_\xi p_\eta - x_\eta p_\xi) = \frac{1}{c^2} p_{tt}, \end{aligned} \quad (3.26)$$

So far, the transformation T between the coordinate system (ξ, η) and (x, y) has not been defined. In the next section, T is defined through the solution of a system of elliptic partial differential equations (PDE).

3.2.3 Elliptic Grid Generation

Among the desirable properties of grid generation procedures are smoothness and non-overlapping gridlines. Based on the maximum value principle for PDEs, these two properties can be achieved by defining $T: \mathcal{D}' \rightarrow \mathcal{D}$ as the solution of the quasi-linear elliptic system

$$\alpha x_{\xi\xi} - 2\beta x_{\xi\eta} + \gamma x_{\eta\eta} = 0 \quad (3.27)$$

$$\alpha y_{\xi\xi} - 2\beta y_{\xi\eta} + \gamma y_{\eta\eta} = 0, \quad (3.28)$$

where $\alpha = x_\eta^2 + y_\eta^2$, $\beta = x_\xi x_\eta + y_\xi y_\eta$, and $\gamma = x_\xi^2 + y_\xi^2$, with Dirichlet boundary conditions.

The system of Eqs. (3.27) and (3.28) is known as Winslow elliptic grid generator.

A more robust grid generator can be obtained by introducing control functions ψ and ϕ into Eqs. (3.29) and (3.30). These control functions are responsible for grid properties such as orthogonality, gridline spacing, and cell areas among others. In this thesis, the grid generator

introduced by Villamizar and Acosta will be adopted.³¹ Thus, these control functions help to define the transformation \mathcal{T} as

$$\alpha x_{\xi\xi} - 2\beta x_{\xi\eta} + \gamma x_{\eta\eta} = -\alpha\psi(\xi, \eta)x_{\xi} - \gamma\phi(\xi, \eta)x_{\eta}, \quad (3.29)$$

$$\alpha y_{\xi\xi} - 2\beta y_{\xi\eta} + \gamma y_{\eta\eta} = -\alpha\psi(\xi, \eta)y_{\xi} - \gamma\phi(\xi, \eta)y_{\eta}, \quad (3.30)$$

where $\psi = \alpha_{\xi}(\xi, \eta)/2\alpha(\xi, \eta)$ and $\phi = \gamma_{\eta}(\xi, \eta)/2\gamma(\xi, \eta)$ are the grid control functions. The grids generated by Eqs. (3.29) and (3.30) constitute a generalized transformation of polar grids to arbitrary regions. Substitution of the right-hand side of Eqs. (3.29) and (3.30) into Eq. (3.26) simplifies the expression considerably. In summary, the entire IBVP is written in terms of generalized curvilinear coordinates as

$$\begin{aligned} \frac{1}{J^2}(\alpha p_{\xi\xi} - 2\beta p_{\xi\eta} + \gamma p_{\eta\eta}) + \left(\frac{\alpha\psi}{J^2} - \frac{x_{\eta}}{yJ}\right)p_{\xi} + \left(\frac{\gamma\phi}{J^2} + \frac{x_{\xi}}{yJ}\right)p_{\eta} \dots \\ = \frac{1}{c^2}p_{tt}, \end{aligned} \quad (\xi, \eta) \in \mathcal{D}', \quad t > 0, \quad (3.31)$$

$$\frac{\partial}{\partial n}p(\xi, N_2, t) = \frac{1}{J\sqrt{\gamma}}(\gamma p_{\eta} - \beta p_{\xi}) = 0, \quad (\xi, \eta) \in C_4' \cup C_3', \quad (3.32)$$

$$\frac{\partial}{\partial n}p(1, \eta, t) = \frac{1}{J\sqrt{\alpha}}(\beta p_{\eta} - \alpha p_{\xi}) = \begin{cases} -\rho_0 a_n, & t = 0 \\ 0, & \text{otherwise} \end{cases}, \quad (\xi, \eta) \in C_1', \quad (3.33)$$

$$p_t + \frac{c}{JR}((xy_{\eta} - yx_{\eta})p_{\xi} + (yx_{\xi} - xy_{\xi})p_{\eta}) + \frac{c}{2R}p = 0, \quad (\xi, \eta) \in C_2', \quad (3.34)$$

$$p(\xi, \eta, 0) = 0 \quad \text{and} \quad p_t(\xi, \eta, 0) = 0, \quad (\xi, \eta) \in \mathcal{D}', \quad (3.35)$$

where $R = \sqrt{x^2 + y^2}$. Equations (3.31)-(3.35) are in the form used during FD discretization, as described in the following section.

3.2.4 Discretization

A second-order discretization of all the governing equations expressed in curvilinear coordinates is used in this thesis. Since the governing equations are partial differential equations in time and space, discretization must occur both temporally and spatially. Temporally, the computation requires the current and past time steps to infer what the solution of the governing equation over the computational domain will be in the future. This second-order method is known as the leapfrog scheme. Time steps are indicated with the index n and written as superscripts in the following equations. Spatially, the computational domain \mathcal{D}' is described by the coordinates ξ and η , where $1 \leq \xi \leq N_1$ and $1 \leq \eta \leq N_2$. For convenience, the computational step size for both of these coordinates is $\Delta\xi = \Delta\eta = 1$. The spatial step size is indicated with the subscripts i and j , which correspond to steps taken in ξ and η respectively.

By solving for the future time step of pressure, using both the spatial and temporal discretizations, the wave equation described by Eq. (3.31) becomes

$$\begin{aligned}
p_{i,j}^{n+1} &= 2p_{i,j}^n - p_{i,j}^{n-1} \dots \\
&+ \delta_{i,j}^2 \left[\alpha_{i,j} (p_{i+1,j}^n - 2p_{i,j}^n + p_{i-1,j}^n) \dots \right. \\
&- \frac{\beta_{i,j}}{2} (p_{i+1,j+1}^n - p_{i+1,j-1}^n - p_{i-1,j+1}^n + p_{i-1,j-1}^n) \dots \\
&+ \gamma_{i,j} (p_{i,j+1}^n - 2p_{i,j}^n + p_{i,j-1}^n) \dots \\
&+ \left(\frac{(\alpha_\xi)_{i,j}}{4} - \frac{J_{i,j}(x_\eta)_{i,j}}{2y_{i,j}} \right) (p_{i+1,j}^n - p_{i-1,j}^n) \dots \\
&\left. + \left(\frac{(\gamma_\eta)_{i,j}}{4} + \frac{J_{i,j}(x_\xi)_{i,j}}{2y_{i,j}} \right) (p_{i,j+1}^n - p_{i,j-1}^n) \right],
\end{aligned} \tag{3.36}$$

where $\delta_{i,j} = c\Delta t/J_{i,j}$ and Δt is the time step. All of the relevant discretizations are as follows:

$$\begin{aligned}
p_{tt} &= p_{i,j}^{n+1} - 2p_{i,j}^n + p_{i,j}^{n-1}, & p_\eta &= (p_{i,j+1}^n - p_{i,j-1}^n)/2, \\
p_{\xi\xi} &= p_{i+1,j}^n - 2p_{i,j}^n + p_{i-1,j}^n, & (x_\eta)_{i,j} &= (x_{i,j+1} - x_{i,j-1})/2, \\
p_{\xi\eta} &= (p_{i+1,j+1}^n - p_{i+1,j-1}^n - p_{i-1,j+1}^n + p_{i-1,j-1}^n)/4, & (x_\xi)_{i,j} &= (x_{i+1,j} - x_{i-1,j})/2, \\
p_{\eta\eta} &= p_{i,j+1}^n - 2p_{i,j}^n + p_{i,j-1}^n, & (y_\eta)_{i,j} &= (y_{i,j+1} - y_{i,j-1})/2, \\
p_\xi &= (p_{i+1,j}^n - p_{i-1,j}^n)/2, & (y_\xi)_{i,j} &= (y_{i+1,j} - y_{i-1,j})/2.
\end{aligned}$$

All of the other metrics found in Eq. (3.36) are composed of these discretizations. Equation (3.36) is only used to calculate approximate values for $p_{i,j}^{n+1}$ on the interior points in the computational domain. When the computation is at an edge of the domain, the boundary condition equations, Eqs. (3.32)-(3.34), need to be discretized. Depending on the location of the boundary point, different discretizations may be required because the interior points necessary

for the approximation cannot be referenced the same way. Accurate computation at the boundaries require the consideration of ghost points. These are points that lie outside of the domain, but can still be used in the calculation of the field values at the boundary points. Essentially, the ghost points provide the additional grid point needed to combine the governing equation [Eq. (3.36)] with the discretized boundary condition equations. This combination of equations is desirable because field values at boundary points are affected by both.

Since the discretizations of the boundary conditions are different for each boundary of the domain, they are treated individually. Thus, at the boundary line C_1 , a second-order discretization leads to

$$p_{0,j}^n = \begin{cases} p_{2,j}^n - \left[\frac{\beta_{1,j}}{\alpha_{1,j}} (p_{1,j+1}^n - p_{1,j-1}^n) + \frac{2\rho_0(\hat{a})_{1,j}}{\alpha_{1,j}} \right], & t = 0, \\ p_{2,j}^n - \frac{\beta_{1,j}}{\alpha_{1,j}} (p_{1,j+1}^n - p_{1,j-1}^n), & \textit{otherwise}, \end{cases} \quad (3.37)$$

where the value at the ghost point, $p_{0,j}^n$, has been solved for. Once the field value at the ghost point is known, it is substituted into Eq. (3.36) for calculation of the pressure field at the boundary point. Thus, the boundary condition equations are accounted for in the governing equation by substitution of the ghost point.

The rigid condition on boundary C_4 and the symmetry condition on boundary C_3 are very similar. Both require that the normal derivative of the pressure be zero. Their discretizations are similar since their normal vectors are in the same axis (but opposite in direction) in the computational domain. Once again, second-order discretizations and ghost points are used to calculate the field values at these boundaries. Thus,

$$p_{i,N_2+1}^n = p_{i,N_2-1}^n + \frac{\beta_{i,N_2}}{\gamma_{i,N_2}} (p_{i+1,N_2}^n - p_{i-1,N_2}^n), \quad (3.38)$$

which solves for the ghost point for boundary C_4 , and

$$p_{i,0}^n = p_{i,2}^n, \quad (3.39)$$

which solves for the ghost point for boundary C_3 , due to symmetry. Intuitively, this is exactly what is needed since symmetry should impose a mirror image of the problem. Both sets of ghost points are substituted into Eq. (3.36) to calculate the pressure field with application of the boundary conditions from the ghost points.

Finally, a second-order discretization for the absorbing boundary condition on boundary C_2 is presented. Because both the governing wave equation and the absorbing boundary condition contain derivatives of pressure temporally and spatially, finding $p_{N_1,j}^{n+1}$ requires that both equations be first solved in terms of their ghost point, $p_{N_1+1,j}^n$. Then both discrete equations are set equal to one another, eliminating the field value at the ghost point, and the resulting single equation is solved for the future pressure value $p_{i,j}^{n+1}$. This procedure leads to,

$$\begin{aligned}
p_{i,j}^{n+1} = & \frac{1}{1 + \frac{c\Delta t R}{\lambda_{i,j} J_{i,j}} \left(\alpha_{i,j} + \frac{(\alpha_\xi)_{i,j}}{4} - \frac{(x_\eta)_{i,j} J_{i,j}}{2y_{i,j}} \right)} \left[\delta_{i,j}^2 \left(\left(\alpha_{i,j} + \frac{(\alpha_\xi)_{i,j}}{4} \dots \right. \right. \right. \\
& \left. \left. \left. - \frac{(x_\eta)_{i,j} J_{i,j}}{2y_{i,j}} \right) \left(-\frac{2\kappa_{i,j}}{\lambda_{i,j}} p_\eta - \frac{J_{i,j}}{\lambda_{i,j}} p_{i,j}^n + \frac{RJ}{c\lambda\Delta t} p_{i,j}^{n-1} \right) \dots \right. \right. \\
& \left. \left. + 2\alpha_{i,j} (p_{i-1,j}^n - p_{i,j}^n) - 2\beta_{i,j} p_{\xi\eta} + \gamma_{i,j} p_{\eta\eta} \dots \right. \right. \\
& \left. \left. + \left(\frac{(\gamma_\eta)_{i,j}}{2} + \frac{(x_\xi)_{i,j} J_{i,j}}{y_{i,j}} \right) p_\eta \right) + 2p_{i,j}^n - p_{i,j}^{n-1} \right], \tag{3.40}
\end{aligned}$$

where $\kappa_{i,j} = y_{i,j}(x_\xi)_{i,j} - x_{i,j}(y_\xi)_{i,j}$ and $\lambda_{i,j} = x_{i,j}(y_\eta)_{i,j} - y_{i,j}(x_\eta)_{i,j}$.

In summary, a FD technique has been developed, supported by a set of special elliptic grids, that applies to wave propagations through axially symmetric boundaries in three-dimensional space. Villamizar and Acosta³²⁻³⁶ have developed a variety of curvilinear grids, including the one used in this thesis, and have applied them to multiple scattering in two-dimensions.

3.2 Numerical Simulation

The model simulated in this thesis is exactly one-fourth the size of the mathematical model used by Stepanishen and Tougas.²⁸ In order to compare relevant results, the frequencies used in our model are increased by a factor of four so the wavelengths can be reduced by a factor of four as well. This creates the same pipe diameter to wavelength ratio used by Stepanishen and Tougas. Thus, the 2 kHz and 4 kHz results reported by Stepanishen and Tougas correspond to the 8 kHz and 16 kHz results presented in this work. The cylindrical, rigid pipe is 0.5 meters

long with a radius of $a = 19.05$ mm (0.75 inches). One end of the pipe is mounted to an infinite, rigid baffle.

The absorbing boundary condition, applied at boundary C_2 , is a constant radius $R = 50$ cm from the origin, located at the center of the exit of the pipe. Boundary C_2 was placed from the pipe exit, over 7.5 times the Rayleigh distance ($ka^2/2$, where k is the acoustic wavenumber) for the highest frequency considered. Although the radiation patterns versus angle at 80 and 100 cm from the exit of the pipe (when the computational model is evaluated with C_2 at greater distances) look slightly different, indicating that the 50 cm boundary may still be in the near field, it is of computational interest for transient analysis to keep the model smaller with an artificial infinite boundary at the approximate 50 cm radius from the center of the pipe exit.

To independently excite natural modes of the pipe independently, an appropriate acceleration profile is defined. The goal is to create a source function such that all of the acoustic energy produced by the source is transferred into any desired mode. Following Ref. [28], the acceleration profile of the piston, $\hat{a}(r, t)$, was required to satisfy the following relationship:

$$\alpha_{m,n} = \frac{1}{S} \int_S \hat{a}(r, t) \Phi_{m,n} dS. \quad (3.41)$$

where $\alpha_{m,n}$ is the modal coefficient, $\Phi_{m,n}$ is the mode, or eigenfunction of a circular pipe, and S is the cross-sectional area of the pipe. For a circularly symmetric pipe these eigenfunctions are

$$\Phi_{0,n} = J_0(\chi_{0,n}r), \quad n = 1, 2, \dots, \quad (3.42)$$

where $J_0(\chi_{0,n}r)$ is a zero-order Bessel function of the first kind. Subscript m is always zero because only axisymmetric modes are considered (as done by Stepanishen and Tougas). The values of $\chi_{0,n}$ are determined from the rigid boundary condition at $r = a$, the radius of the pipe,

and are the set of discrete values which satisfy the wave equation in the radial direction

Substitution of Eq. (3.42) into Eq. (3.41) results in

$$\alpha_{0,n} = \frac{1}{S} \int_S \hat{a}(r, t) \Phi_{0,n} dS = \frac{2\pi}{S} \int_0^a \hat{a}(r, t) J_0(\chi_{0,n} r) r dr. \quad (3.43)$$

At this point, an acceleration profile *different* from Stepanishen and Tougas' is chosen. While their function is versatile, it cannot excite modes of the pipe independently. Based on the orthogonality property of the Bessel functions, the acceleration profile is chosen as

$$\hat{a}(r, t) = \begin{cases} J_0(\chi_{0,p} r) \sin\left(\frac{2\pi t}{T_d}\right), & 0 \leq t \leq T_d, \\ 0, & \text{otherwise,} \end{cases} \quad (3.44)$$

where T_d is the period defined by single-cycle sine wave. Thus, by orthogonality and for $0 \leq t \leq T_d$,

$$\alpha_{0,n} = \frac{2\pi}{S} \int_0^a J_0(\chi_{0,p} r) \sin\left(\frac{2\pi t}{T_d}\right) J_0(\chi_{0,n} r) r dr = \begin{cases} J_{0,p}(i_{1,p})^2 \sin\left(\frac{2\pi t}{T_d}\right), & p = n, \\ 0, & p \neq n, \end{cases} \quad (3.45)$$

where $i_{1,n}$ is the n^{th} root of the first-order Bessel function of the first kind. This spatial profile is the simplest profile that can be chosen if pipe modes are to be independently excited. Any other spatial profile would require an infinite series to describe the shape of a Bessel function.

If the acceleration profile above is used to excite each pipe mode independently, there can be problems with minimal excitation of lower-order modes (namely the plane-wave mode). Essentially, the discrete profile of the pressure distribution does not perfectly couple the energy to the specific pipe mode of interest and leakage occurs [see Fig. 3.6(c)]. This imperfection has only been observed during excitation of higher-order modes, where the spatial portion of each acceleration profile becomes more difficult to represent, and is reduced significantly after increasing the number of grid lines in the radial direction.

3.3 FDM Results

The FD model allows the study of the angular and time dependent properties of each natural mode of the pipe as it radiates to the absorbing boundary. In order to study the radiation from the modes of the pipe independently, the prescribed acceleration profile at the source boundary is prescribed as a Bessel function of order zero, as explained in the previous section. Simulations of the first three modes of the pipe, independently excited and radiated to the absorbing boundary, are recorded and analyzed using a 3101 x 71 point grid. Figures 3.4 and 3.5 show the development of wave propagation over time for the plane-wave and the first higher-order mode for a 16 kHz single-cycle, sine wave excitation signal, respectively. While the pulse begins and stays as a compact, single condensation for the plane-wave mode (explained later), the signal rapidly disperses as it propagates for all other higher-order modes. Upon arrival at the exit of the pipe, each wave crest imparts its energy to either transmission and eventual far-field radiation [as shown more clearly in Figs. 3.4(e)-3.5(e)], or reflection back down the pipe [as shown more clearly in Figs. 3.4(f)-3.5(f)].

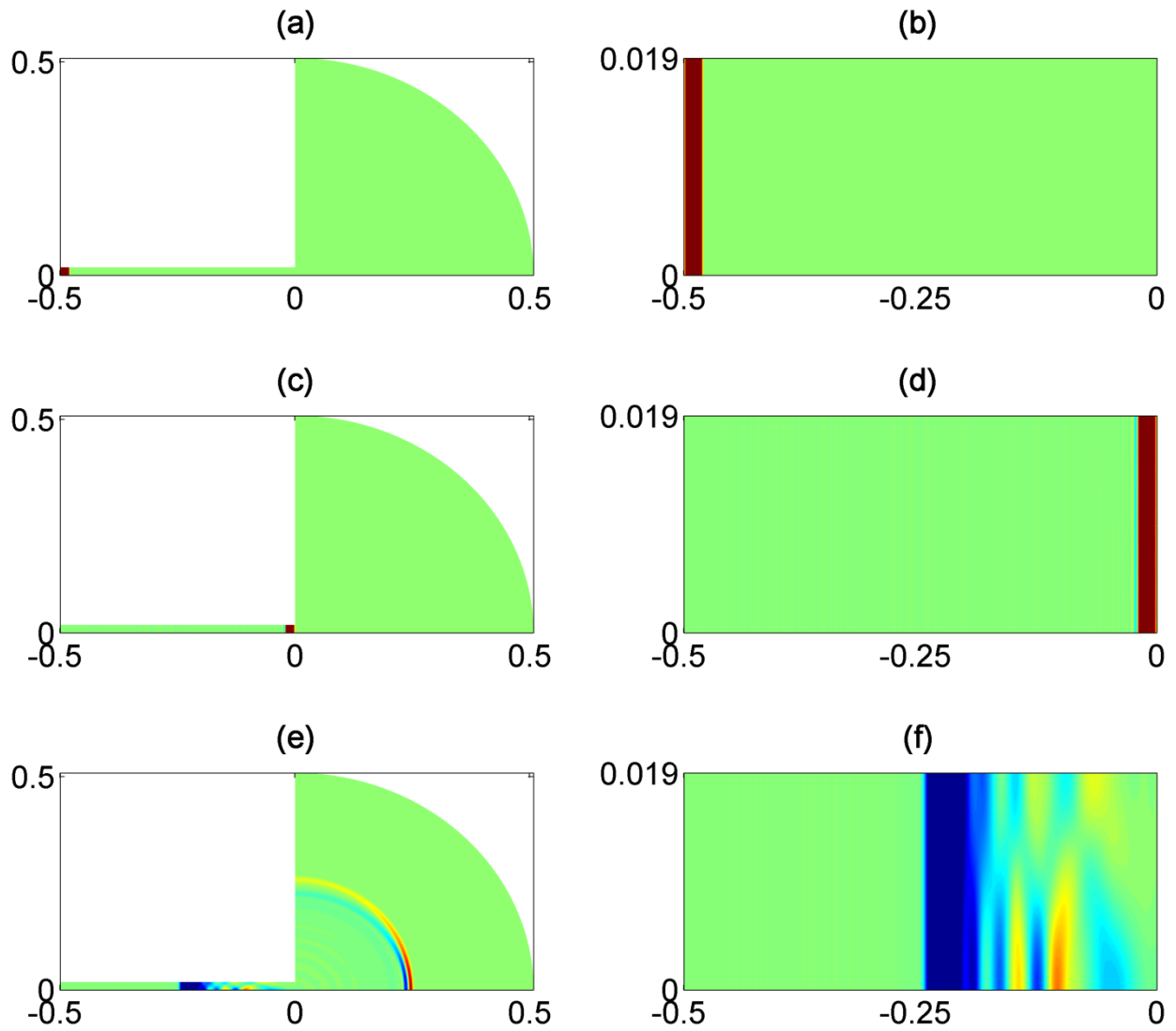


FIG. 3.4. Wave propagation images for a single-cycle 16 kHz excitation signal in the (0,0) mode. Wave propagation for the full spatial model is shown to scale in (a), (c), and (e). Wave propagation within the pipe at an exaggerated vertical scale is shown in (b), (d), and (f). The times for each subplot are as follows: (a) and (b) 0.0625 ms, (c) and (d) 1.5 ms, (e) and (f) 2.2 ms.

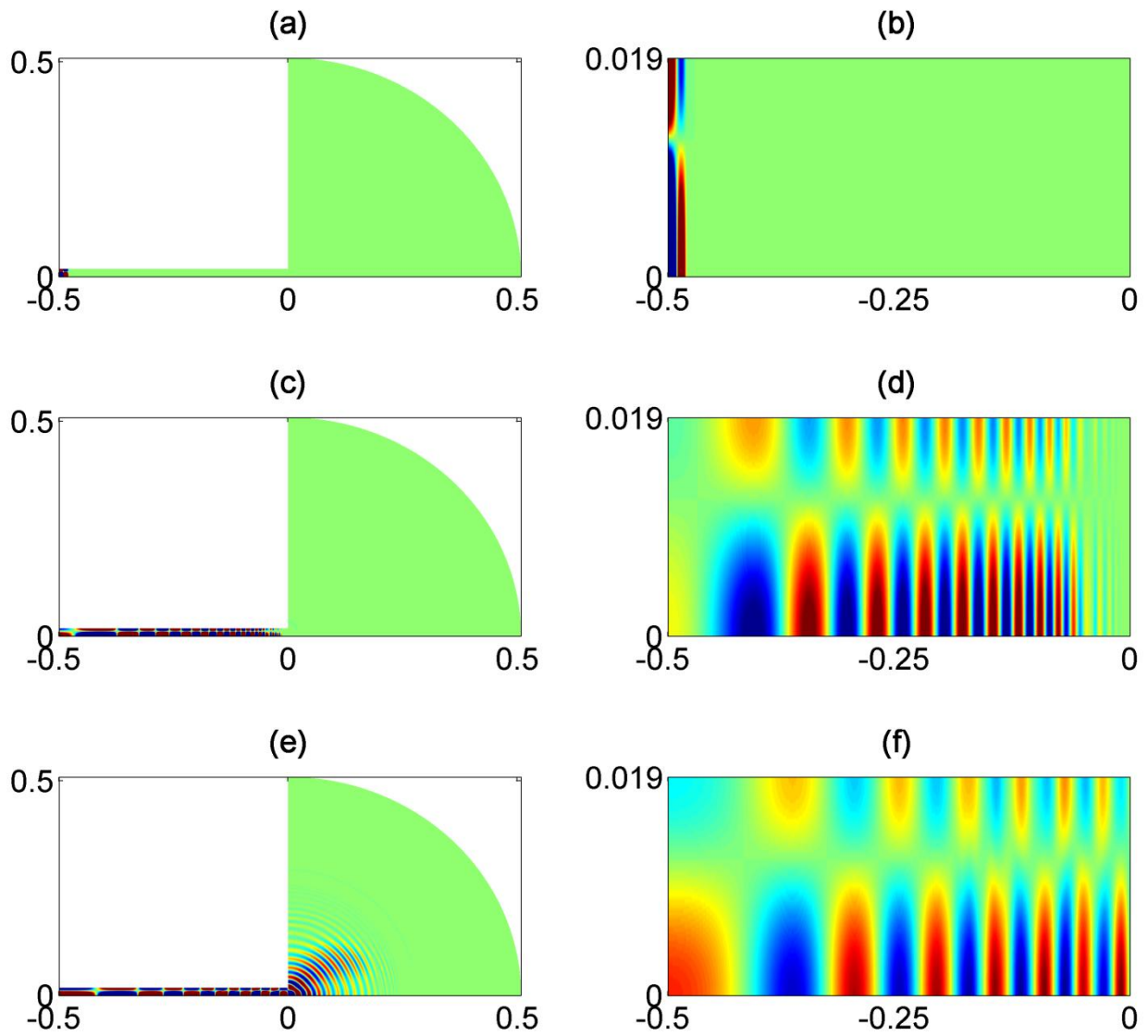


FIG. 3.5. Wave propagation images for a single-cycle 16 kHz excitation signal in the (0,1) mode. Wave propagation for the full spatial model is shown to scale in (a), (c), and (e). Wave propagation within the pipe at an exaggerated vertical scale is shown in (b), (d), and (f). The times for each subplot are as follows: (a) and (b) 0.0625 ms, (c) and (d) 1.5 ms, (e) and (f) 2.2 ms.

The preceding figures are best understood within the context of group and phase speed. As explained in many fundamental acoustics textbooks,³⁷⁻³⁸ phase speed is defined as

$$c_p = \frac{c}{\sqrt{1 - \left(\frac{f_N}{f}\right)^2}}, \quad (3.46)$$

and group speed, the speed at which the energy propagates, is defined as

$$c_g = c \sqrt{1 - \left(\frac{f_N}{f}\right)^2}, \quad (3.47)$$

where f_N is the cutoff frequency for the N^{th} pipe mode. Considering Eqs. (3.46) and (3.47) for a given cutoff frequency, frequencies greater than the cutoff frequency propagate (with no attenuation) through the pipe at its specified group speed, while frequencies less than the cutoff frequency decay exponentially with distance.

Figure 3.4 shows the propagation of a single-cycle sine wave with a plane-wave spatial profile. Since, the cutoff frequency of the plane wave mode is 0 Hz, all frequencies with this spatial profile propagate through the pipe with no evanescence. Additionally, all frequencies have the same group and phase speed. As a result, the pulse-like shape created at the beginning of the pipe is maintained throughout the first propagation down the pipe, from the source to the pipe exit. The pressure profile for the plane-wave mode (see Fig. 3.4) does not appear to be the gated sine wave assigned to the acceleration profile because it is proportional to velocity.⁹ To understand what the pulse should look like in the pressure field, the acceleration profile is integrated in time and multiplied by constants of the fluid. Thus, the pressure takes the form

$$\begin{aligned} p &= \rho_0 c u \\ &= \rho_0 c \int_0^t \hat{a}(r, \bar{t}) d\bar{t} \\ &= \frac{\rho_0 c T_d}{2\pi} J_0(\chi_{0,0} r) \left(1 - \cos\left(\frac{2\pi t}{T_d}\right)\right) \end{aligned} \quad (3.48)$$

for the plane wave mode.

Figure 3.5 is also explainable through the concepts of group and phase velocity. The cutoff frequency for the first axisymmetric cross mode is no longer 0 Hz as it was for the plane wave mode, but is approximately 10,975.3 Hz. Thus, frequencies below the cutoff decay exponentially and frequencies above the cutoff propagate. An additional observation due to dispersion is that higher frequencies are observed to lead lower frequencies. Their group speeds are higher and thus travel down the pipe more quickly. As the frequencies increase, their group speed approaches the sound speed of the fluid c . If multiple modes were excited in the pipe for a single frequency, lower modes would travel down the pipe faster as their group velocity would be higher. Combining these concepts helps to understand the problem where multiple modes and multiple frequencies are excited. Again, lower-order modes travel down the pipe faster than higher-order modes for a single frequency, but higher frequencies travel down the pipe faster than lower frequencies of a given mode (with exception to the plane-wave mode). Additionally, because the boundary conditions for the pipe walls are completely rigid, no energy is lost in the reflections from the pipe walls. These reflections would not be produced to this magnitude if the boundary condition of the pipe walls included a finite amount of damping.

Physically, at higher frequencies multiple modes are almost always excited. Thus, lower frequencies (usually contained in lower-order modes due to evanescence of low frequencies for higher-order modes) travel down the pipe faster than higher frequencies and can significantly spread out with a long enough pipe to where the sweep in frequency is audible.¹⁶ After more time has passed, the signal falls in pitch. This is due to the slowly-decaying, reactive energy of lower frequencies.²⁸ Higher frequencies radiate from the pipe more easily due to the mostly resistive acoustic loading seen at the exit of the pipe. Because their wavelengths are so small, the exit of

the pipe begins to resemble a free-field condition, rather than a reactive boundary. Thus, almost no energy is reflected back into the pipe for higher frequencies, and most of the high-frequency energy is found, in the beginning of the signal arriving in the far-field. Lower frequencies continue to ring due to the high amount of energy reflected back down the pipe. This energy containment within the pipe causes continued lower frequency radiation and accounts for the fall in pitch after the initial rise in pitch due to dispersion.

As alluded to previously, a main point of analysis for each simulation is to record the radiated pressure over time as it arrives at the absorbing boundary (the semi-circular boundary, or right-hand side of the model as depicted in Figs. 3.4 and 3.5). By storing these data, the radiated pressure along this boundary from the finite-length pipe can be viewed as a function of time. Figure 3.6 shows the results of the pressure amplitude as a function of angle and time. The various subplots depict the radiation due to different pipe modes as noted in the caption. Note the different arrival times for each independently excited mode. The plane-wave mode travels at the sound speed of the fluid c . If this variable is taken to be 343 m/s and the sound must travel 1.008 meters, the signal should first arrive at the boundary at approximately 2.939 ms. Very high frequencies of higher-order modes can travel close to the sound speed of the fluid; however, the numerical grid needs to be very fine to account for these frequencies. The main body of energy is contained in frequencies centered around 16 kHz (the frequency of the single-cycle excitation period), which will travel notably slower than the plane-wave mode. When multiple modes and frequencies are excited, Fig. 3.6(d) shows arrival of the plane wave mode first, while each higher-order mode takes progressively longer to arrive at the absorbing boundary.

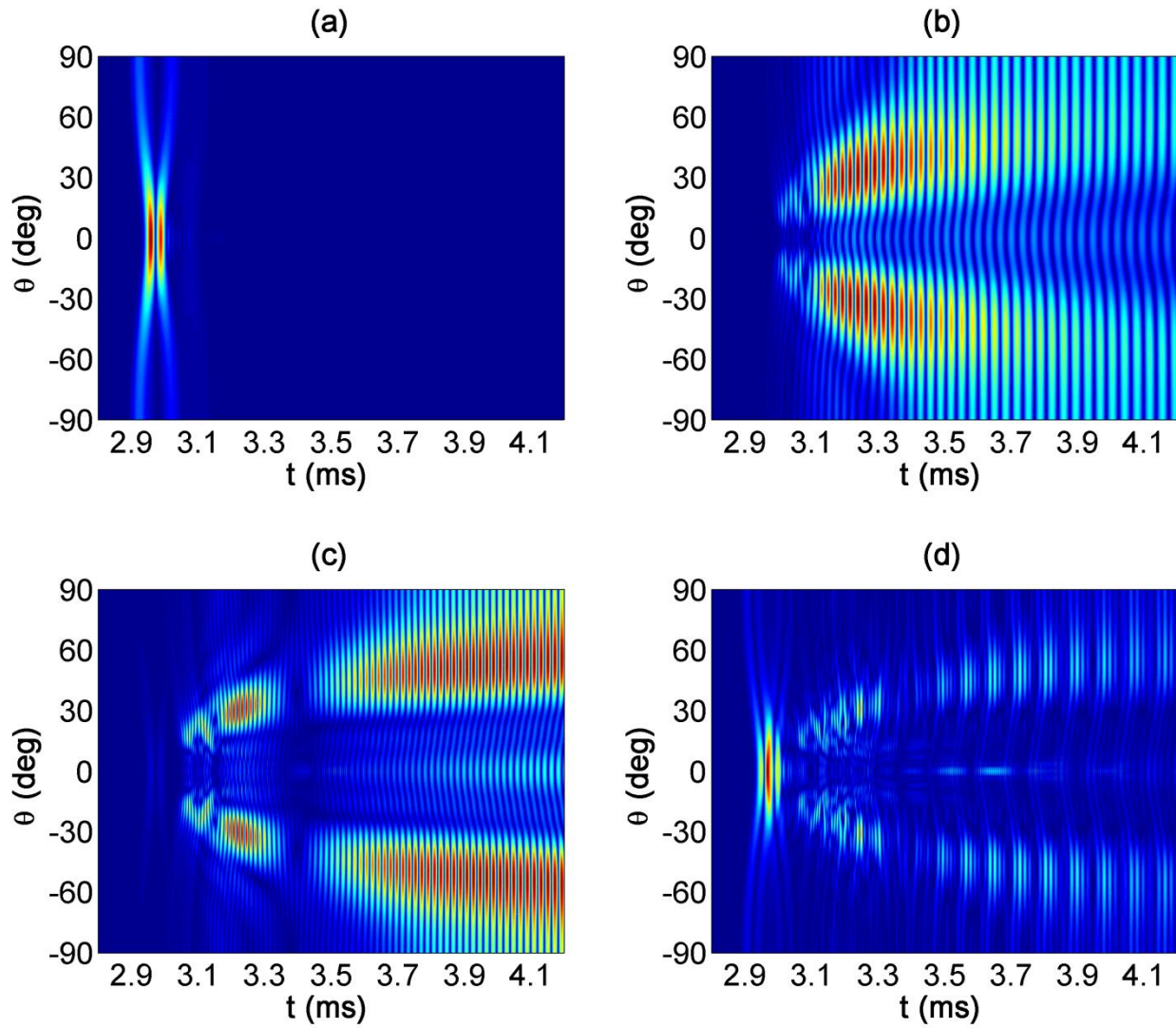


FIG. 3.6. Far-field radiation (pressure magnitude) measured at 0.508 meters from the exit of the pipe as a function of angle and time. (a) (0,0) mode. (b) (0,1) mode. (c) (0,2) mode. (d) Combination of several modes.

3.4 Discussion

As Stepanishen and Tougas²⁸ found, the results in Fig. 3.6 show significant off-axis radiation for higher-order modes. The radiation pattern not only depends on frequency, but also

on the spatial excitation profile of the driver. As frequency increases or the pipe mode number increases, and so does the angle of maximum radiation (with exception to the plane-wave mode whose maximum radiation is on axis). Table 3.1 summarizes the angles at which maximum radiation occurs for the 8 kHz and 16 kHz single-cycle sine-wave excitation signals.

TABLE 3.1. Angles of maximum pressure radiation for the first three modes of the pipe.

	8 kHz	16 kHz
Mode (0,0)	0°	0°
Mode (0,1)	27°	33°
Mode (0,2)	36°	34°

The angles at which maximum pressure radiation occurs agree with the results obtained by Stepanishen and Tougas. However, in contrast to their results, on-axis pressure radiation from higher-order modes in these finite-difference simulations is non-zero. The theory derived in Stepanishen and Tougas' paper assumes that the pipe modes correlated with the half-space modes on a one-to-one basis, where no modal coupling occurs between the two domains. As a result, the acoustical spatial profile at the exit of the pipe was simply used as the velocity spatial profile at the excitation boundary, which resulted in zero on-axis radiation for higher-order modes in the far field. Stepanishen and Tougas did realize the importance of accounting for modal coupling between domains and cited it as future work; however, this becomes difficult to do analytically, requiring the use of some numerical method for a more accurate depiction of pressure radiation for higher-order modes.

The model used to compute the results in Fig. 3.6 automatically accounts for coupling between the pipe modes and the half-space modes. Thus, on-axis radiation is expected to a certain degree since individually excited higher-order modes of the pipe excite all of the half-space modes. The coefficient for each half-space mode highly depends upon the spatial profile of

the propagating acoustic modes in the pipe. The majority of the energy for a pipe mode is transferred to the half-space modes on a one-to-one basis, but not completely. This possibly explains why the pressure maximums obtained in the results presented here agree with those found by Stepanishen and Tougas, although minor variations in the radiation patterns are observed. Thus, Stepanishen and Tougas' omission of modal coupling from the analytical model resulted in a loss of the finer details of the radiation patterns—one of those details being the existence of on-axis radiation.

Although the numerical simulation simplifies the problem of matching the pipe domain with the half-space domain, the FDM has many problems of its own. First, for transient signals as short as the one considered here, numerical dispersion can be difficult to handle. The simulation must have a sufficient grid size for all higher frequencies that are excited within the model. As the excitation signal becomes shorter, amplitudes of higher frequencies become more significant. Second, the analysis done by Stepanishen and Tougas is only valid in the far field. The expression used by them to describe the half-space modes is essentially the Rayleigh integral where the specified velocity is a mode of the pipe. Ironically, if the directivity of a baffled circular piston is computed in the near field via the Rayleigh integral, significant on-axis radiation is produced. Thus, on-axis radiation found in the current study may be (in part) a near-field effect. As the receiver locations move farther from the source, the on-axis radiation decreases; however, the on-axis radiation never disappears completely—even when the receiver locations are fairly distant from the source. Lastly, to ensure that the recorded radiation patterns were not significantly affected by the imperfect absorbing boundary condition, the boundary was moved farther from the exit of the pipe (by increasing R) while radiated pressure was still

recorded at the same location. Results were the same, showing that the on-axis radiation is likely not occurring due to the imperfect absorptive boundary condition.

3.5 Conclusions

A FD model was created to observe far-field pressure radiation patterns for an infinitely baffled, finite-length pipe. Natural modes of the pipe were excited individually by using a Bessel function for the spatial velocity profile. The independent excitation of these modes resulted in unique radiation patterns over time and angle. The temporal acceleration used for boundary excitation was a single-cycle sine wave. Results were presented for the single-cycle sine wave with a corresponding period of 16 kHz. Each of the signals were varied spatially to excite the (0,0) and (0,1) natural modes of the cylindrical pipe.

Peak-pressures recorded at the absorptive boundary (a 50.8 cm semicircle centered around the exit of the pipe) were observed at very similar locations as found by Stepanishen and Tougas.²⁸ However, the numerical results presented here produced notable on-axis radiation for higher-order modes. On-axis radiation in these results was due to innate coupling of pipe modes with half-space modes in the numerical model, which was not accounted for by Stepanishen and Tougas. Thus, a single-mode excitation of a mode within the pipe will excite all of the half-space modes (to varying degrees).

The effects of dispersion were discussed for situations involving multiple frequencies with excitation of single and multiple pipe modes. Dispersion causes lower modes to travel through the pipe faster than higher modes; however, for a given mode higher frequencies were observed to travel faster than lower frequencies, as expected from well-established theory.

Physically, multiple pipe modes are easily excited and, for long enough pipes, an audible sweep in frequency occurs. Others have remarked about a prolonged ringing caused by the fundamental resonance of the pipe length. This occurs after several reflections of the transient signal occur within the pipe. Thus, the excitation of short-duration transient signals through a finite-length pipe results in an initial sweep in frequency due to dispersion, followed by prolonged radiation of the fundamental frequency of the pipe (a decrease in pitch).

Further work may include extending these results to horns (pipes of varying cross-section). The effects seen in the horn may be less pronounced, but may help to better understand radiation patterns produced by transient signals—which patterns can be very different from steady-state radiation patterns. Further work may also include using a time-dependent, three-dimensional numerical package to excite non-axisymmetric modes.

Chapter 4

Steady-State Analysis of Horns with Simplified Excitation Signals

4.1 Background

In 1919, Webster published a study on wave propagation through horns and on their acoustic impedance.³⁹ Webster realized that acoustical radiation properties of systems like the phonograph could be dramatically altered by the shape and size of the attached horn. It was his goal to change these parameters and increase the acoustical amplification of the system as much as possible. In many respects, his paper was the first modern attempt to quantify the acoustical effects of horns from a mathematically rigorous perspective. Webster gave an equation describing wave propagation through a tube of varying cross-sectional area (a horn), now known as Webster's horn equation:

$$\frac{\partial^2}{\partial x^2} p(x, y, z, t) + \frac{1}{S(x)} \frac{dS(x)}{dx} \frac{d}{dx} p(x, y, z, t) = \frac{1}{c^2} \frac{\partial^2}{\partial t^2} p(x, y, z, t), \quad (4.1)$$

where $p(x, y, z, t)$ is the acoustic pressure, $S(x)$ is the cross-sectional area at position x , and c is the speed of sound.

Since that time, several authors have revisited Webster's techniques and refined his theory.⁴⁰⁻⁴² For example, Webster originally assumed that the wavefronts traveling through the horn must be planar. This was later corrected to include any wavefront whose propagation could be defined by one coordinate of any three-dimensional coordinate system. This type of wavefront was termed a one-parameter wave. Although Eq. (4.1) has not changed in its form, its mathematical interpretation is better understood within this context. An insightful paper on one-parameter waves was published by Putland⁴³ in response to a related paper by Geddes.⁴⁴

Horns tend to "amplify" acoustic signals because they create a more efficient transfer of energy between mechanical and acoustical domains (by creating a gradual impedance match between the two domains). This improved energy transfer is due to the way its shape gradually introduces a wavefront into free space. The equivalent acoustic impedance of an un baffled horn driver, looking into the diaphragm, is much higher than the acoustic impedance of the radiation loading that the diaphragm sees. Additionally, the acoustic impedance of a pipe decreases with increasing cross-sectional area. Thus, if the diaphragm is presented with a horn possessing a smaller diameter opening that gradually increases towards its exit, then the acoustic impedance loading will also gradually decrease, thereby providing the desired gradual impedance match.

Horns not only efficiently transform mechanical energy to acoustic energy, they also channel the acoustic energy to create more directional radiation. Although amplification and directional radiation properties of horns have both been well studied, modern research has given

less attention to the amplification properties of horns due to the advent of powerful electrical amplifiers. Some of the prominent areas of horn research include throat and radiation impedance,⁴⁵⁻⁴⁶ far-field sound radiation,⁴⁷⁻⁵⁰ and numerical techniques for wave propagation.⁵¹⁻⁵⁴

One of the earlier studies on radiation impedance of horns was performed by Freehafer.⁴¹ He studied the analytical case of radiation impedance for an infinite, hyperbolic horn. Similar studies on radiation impedance for other shapes of horns have also been performed.⁴⁵ In early days, most horns used in the audio industry flared exponentially. This changed quickly with the introduction of constant-directivity (CD) horns,⁵⁵ where other geometries showed more consistent sound radiation over angle for larger bandwidths. After this, many different horn geometries were experimented with, which produced new ways to predict the extent of the far-field sound radiation. One method, comparable to the Rayleigh integral, uses the pressure distribution at the exit of the horn to calculate the far-field directivity pattern;⁴⁷ however, experimental specifications such as microphone size and measurement spacing are its biggest setbacks. Another method, more analytically inclined, was used by Gloukhov,⁴⁸ who predicted the directivity patterns based on the Huygens-Fresnel principle. He showed that directional manipulation of acoustic wavefronts is achievable when the aperture is comparable to a wavelength. Yet another technique was developed by Ureda to provide another way of looking at diffraction patterns.⁴⁹ However, his results only included plane-wave excitation at the entrance of the horn.

Since many horn geometries are not analytically definable, the majority of work done has been through either experiment or numerical simulation. Early computational research required analytical simplifications to a large degree as only minimal computations could be performed. One of the first to build a full computational model was Geddes⁵⁰ who created a computational

model of a horn-loaded compression driver. His simplifications included cylindrical symmetry of both the compression driver and horn, an exponential flare in the horn geometry, and encasement of the system within a sphere where the exit of the horn acts as a vibrating cap set in a sphere. Johansen was another to use computational models to compare radiation from conical horns.⁵¹ Similar to Geddes, Johansen's simplification was a pulsating spherical cap, which effectively showed that both radiation patterns from conical horns and a spherical cap were almost identical. This technique of computing the radiation from a spherical cap is very popular and has been used by many to correctly calculate directivity and pressure radiation, even without the need of a numerical model for simulation.⁴⁶ The drawback of the spherical-cap approach is that only certain frequencies will produce wavefronts that align with the radius of curvature specified by the spherical cap. Reference [46] includes a good overview of the additional research performed in this field.

As computer processing speed has increased and numerical schemes have become more robust, many numerical methods have been used to study horns. Geddes used the finite-element method (FEM) in his computational model of the horn-loaded compression driver.⁵⁰ More recently, Hladky-Hennion used the FEM more generically for evaluation of wave propagation in various two-dimensional waveguides.⁵² These results were numerically fundamental and could be extended to asymmetric models, similar to those studied in this chapter. The finite-difference method (FDM) was used in the work done by Noreland²⁶ and Dalmont *et al.*²⁴ Both researchers worked to better understand the radiation from horns used in musical acoustics. Noreland's work simplified the analysis by only assuming plane-wave excitation of the horn by creating a blend of analytical and numerical techniques. Dalmont *et al.* considered axisymmetric horns in steady state for multiple cases to better understand an instrument's acoustic loading. Lastly, the

boundary-element method (BEM) was used by Henwood⁵³ and Johansen.⁵¹ Although, both the results of Johansen and Henwood used analytical simplifications to reduce computational requirements, the BEM handled the problem of infinite radiation well as its formulation does not require any analytical simplifications for an artificial infinite boundary.

Although the use of horns is ubiquitous and the methods for analyzing them seem innumerable, numerical simulation with as little analytical assumptions as possible will help to reveal weaknesses of existing numerical methods. This work will more-fully explore the use of the BEM in determining directivity patterns produced by various three-dimensional horn designs. Additionally, different spatial profiles will be used as inputs at the entrance of the horn. The subsequent steady-state radiation for these profiles will be numerically simulated to better understand the optimal wavefront shape created by compression drivers. These input boundaries of different curvature will help to better understand the nature of acoustic wavefronts as they propagate through a horn of arbitrary cross-sectional area.

4.2 Modeling of Existing Horns

The geometries of the existing horns under test cannot be described by one coordinate in any given three-dimensional coordinate system. As a result, wave propagation within these horns cannot be described by Eq. (4.1). Thus, numerical simulations are an attractive alternative to solving the problem analytically. Simulations for this chapter were performed using Coustyx, a BE package which uses iterative methods to solve the system of equations created by the BEM, for several constant-directivity horns. Field points (computational receivers) were placed 2 degrees apart along arcs in the x - z and y - z planes (the z -axis being the axis along the length of

the horn), approximately 6 meters from the entrance of the horn. Each simulation calculates the pressure and particle velocity at the field points for the one-third octave band center frequencies between 200 Hz and 20 kHz, a total of 21 frequencies.

Because the mesh had to be fine enough to correctly simulate 20 kHz (using at least 6 points per wavelength), it was not computationally practical to model the entire horn. The remedy was to cut the model into a quarter of its original size and take advantage of the symmetry of each horn. Employing mathematical symmetry planes significantly reduces the computational burden for each model, while still maintaining the full and original geometry of each horn. These symmetry planes are used to recreate the pressure and normal velocity profiles of the missing parts of the original geometry to simulate the complete geometry with fewer elements. Each symmetry plane is defined in Cartesian coordinates, so any symmetry displayed by the horn must be defined over a Cartesian plane. The entrance of each horn was then spanned with a planar boundary, which was used as the excitation source for each simulation. After discretization, each mesh was approximately 40,000 elements. Figure 4.1 shows a typical model reduction performed to enhance computational speed. Figure 4.2 illustrates the approximate size of the elements used to represent existing horn geometries. The length of each horn is 0.3048 meters (12 inches).

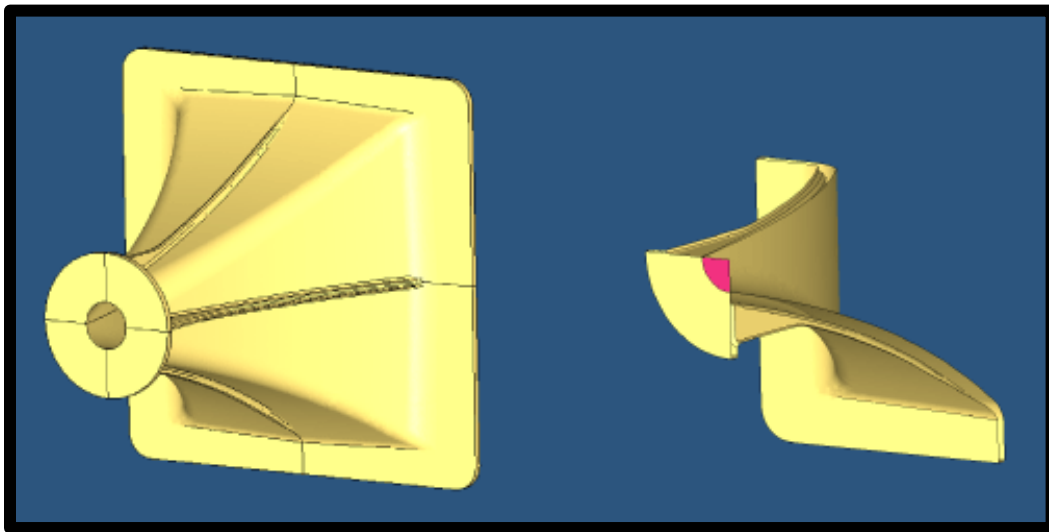


FIG. 4.1. Pictorial illustration of a full horn model and a reduced quarter of the model. Pink boundary represents excitation source.

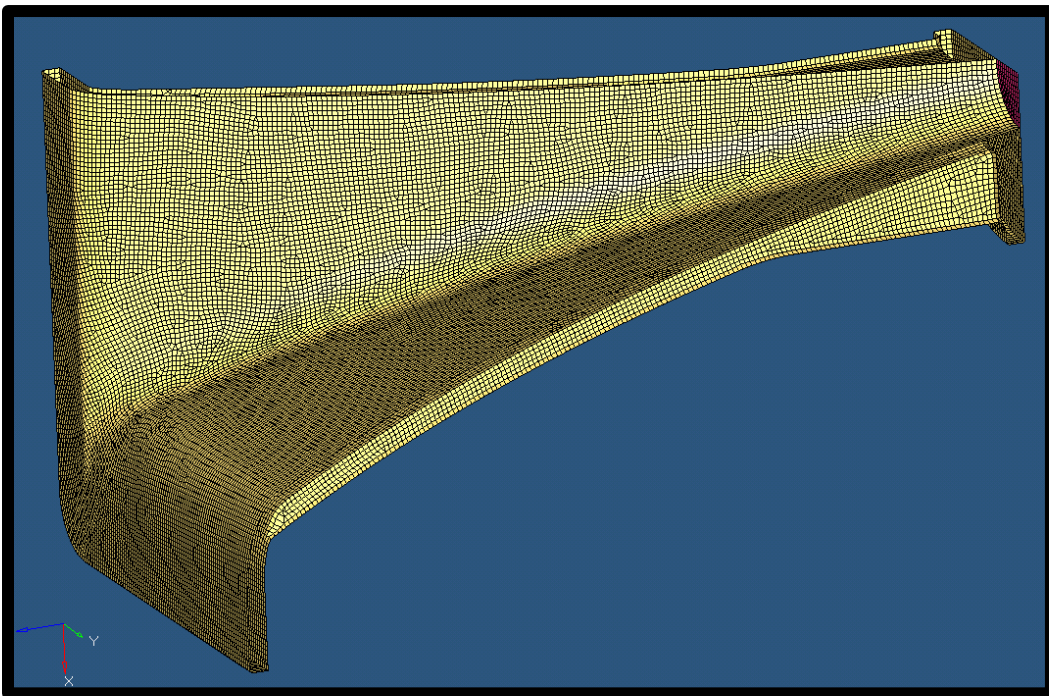


FIG. 4.2. Mesh of existing horn used in BE simulation.

This simplified excitation source is used because the planar boundary is much easier to numerically create than a compression driver. The models of each horn run faster computationally and help benchmark good numerical techniques for this first study, only involving horns. Additionally, it is generally assumed that the wavefronts emerging from the exit of the compression driver are planar. To simulate this condition, the excitation source is assigned a constant velocity in the z -direction. Since the BEM is used for steady-state analysis, the assumed wavefront could be produced at the entrance of the horn and, for the time being, the compression driver is eliminated from the numerical simulation. This planar boundary is illustrated in Fig. 4.1 (pink-colored boundary).

Experimental measurements of directivity (performed by others) are compared with their respective simulations to check the numerical directivity results. Experimental measurements were obtained by mounting each horn under test to a rotational system inside an anechoic chamber. For each field point, the rotational system moved to a certain angle, paused its movement as the system was measured, and the process was repeated for an entire polar slice (360 degrees). Slices in both the vertical and horizontal axes of the horn were taken.

Experimentally measured directivities did differ from numerical simulations in terms of averaging. Numerically simulated directivities for each horn were calculated at a single frequency (the center frequency of the one-third octave band of interest). However several frequencies were used to calculate experimental directivity (for a full one-third octave band), which essentially smoothed the resulting patterns. This difference should not be significant at low frequencies due to the lack of rapid variation in directivity at low frequencies. Although the design of each horn is to produce a similar directivity pattern over a large bandwidth, large variations can occur at high frequencies. Accordingly, values for one-twelfth octave center

frequencies within each one-third octave band are numerically computed at higher frequencies. The directivity for each horn is computed using these five frequencies (there are five one-twelfth octave band center frequencies within a given one-third octave band), though very minimal differences in the directivity patterns are observed between single frequency patterns (at the one-third octave center frequencies) and patterns obtained by averaging the data from all five frequencies. Thus, only the center frequencies for each one-third octave band are used to create simulated directivity patterns.

The horns under test are designed to have a constant directivity over a broad frequency range. The angular specifications listed for each horn are the rough approximations for its beamwidth, which is defined as the angular span in which the decibel value is not reduced by more than 6 dB. For example, a $30^\circ \times 45^\circ$ horn is designed to have a 30° vertical beamwidth and a 45° horizontal beamwidth. Figures 4.3 through 4.6 indicate the -6 dB down point with a bold line. The coverage pattern is the angle spanned by the portion of the directivity pattern greater than -6 dB. Figures 4.3 and 4.4 compare numerical and experimental results for a $30^\circ \times 45^\circ$ horn (part no. 702133). Figures 4.5 and 4.6 compare a $120^\circ \times 60^\circ$ horn (part no. 702135).

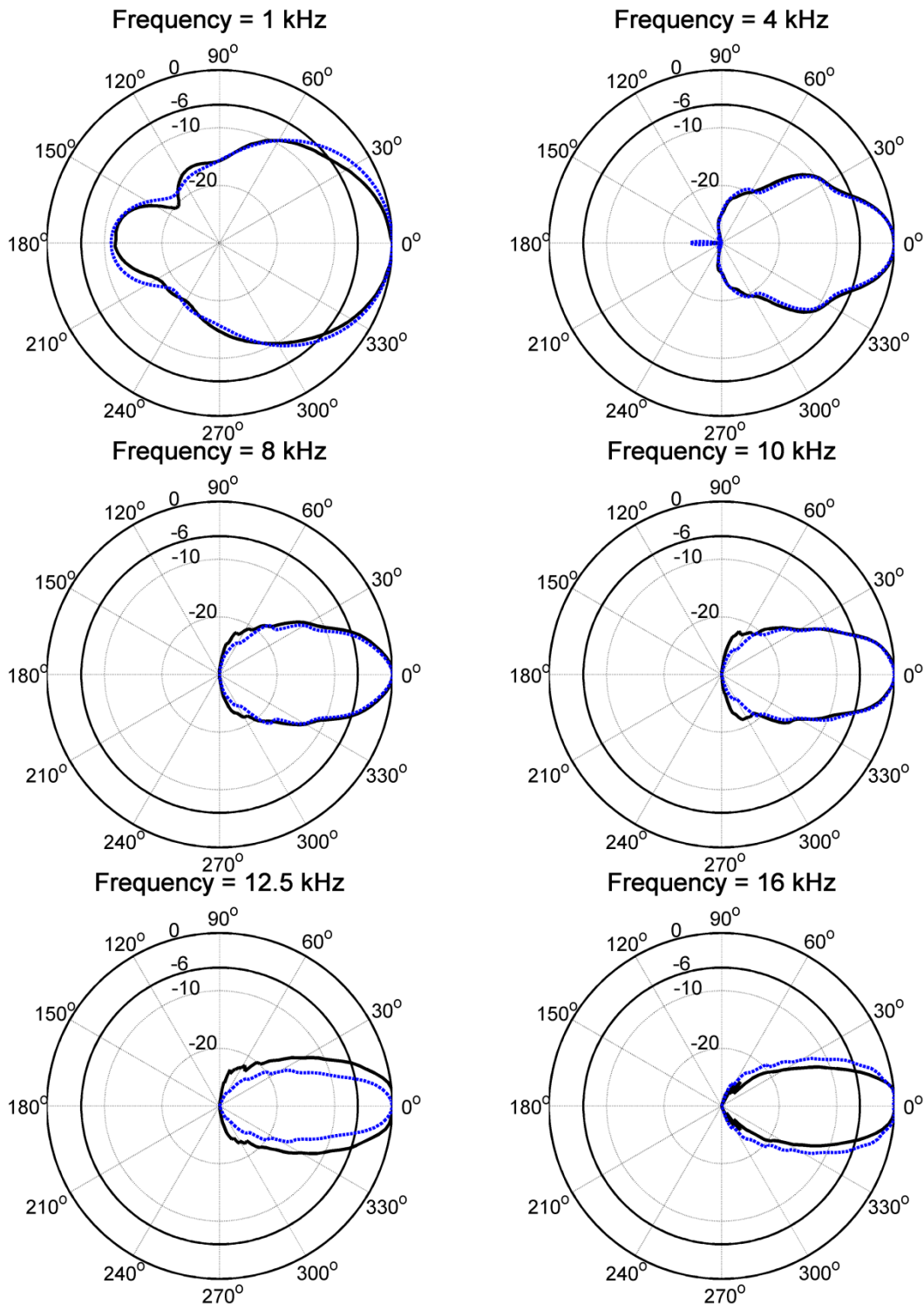


FIG. 4.3. Comparison of pressure directivity in dB (normalized to 0 dB) of a simulated $30^\circ \times 45^\circ$ horn (---) and experimental measurement (—). The decibel value is indicated radially and 0 degrees is on-axis with the horn. The 30° slice is shown.

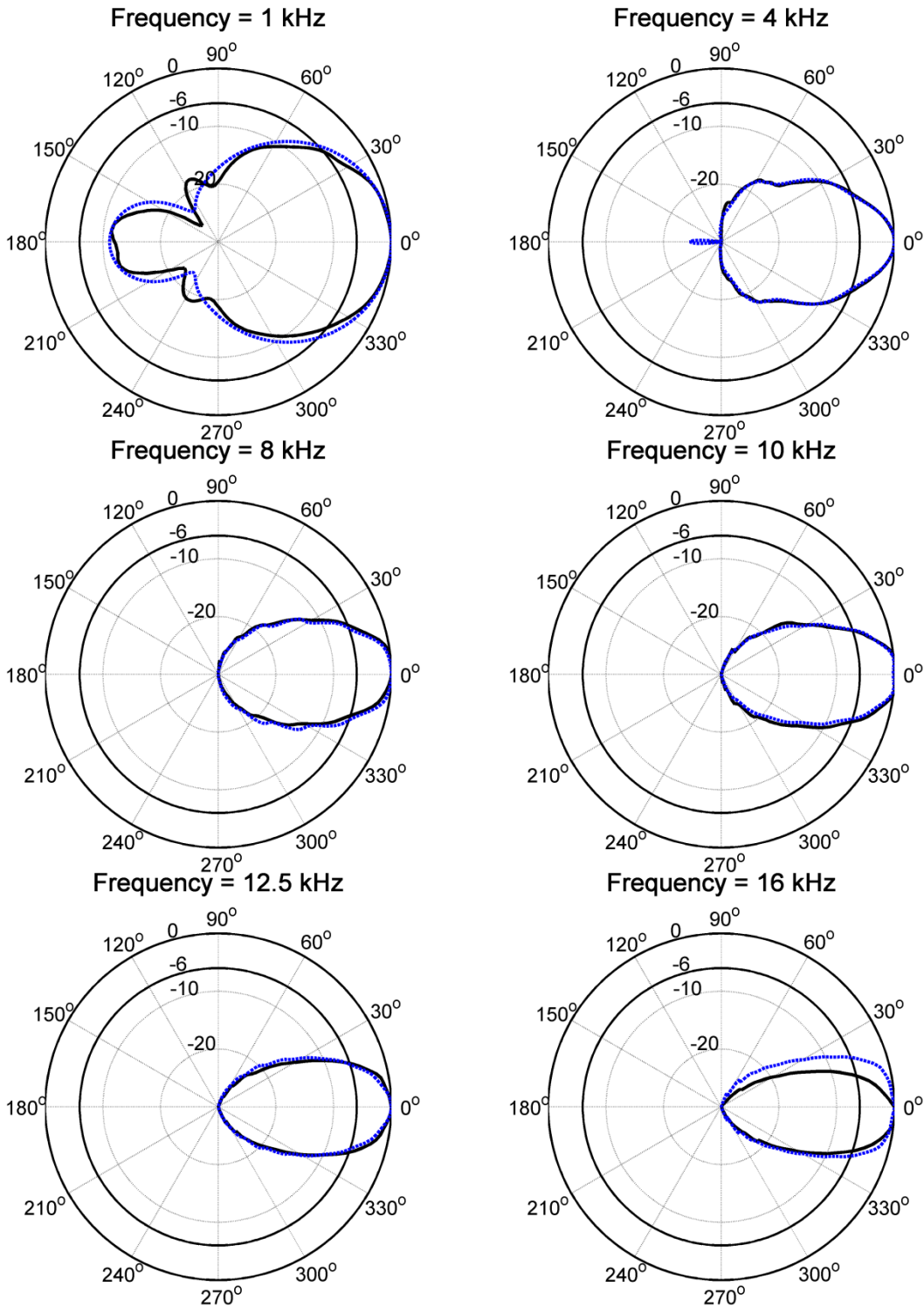


FIG. 4.4. Comparison of pressure directivity in dB (normalized to 0 dB) of a simulated $30^\circ \times 45^\circ$ horn (---) and experimental measurement (—). The decibel value is indicated radially and 0 degrees is on-axis with the horn. The 45° slice is shown.

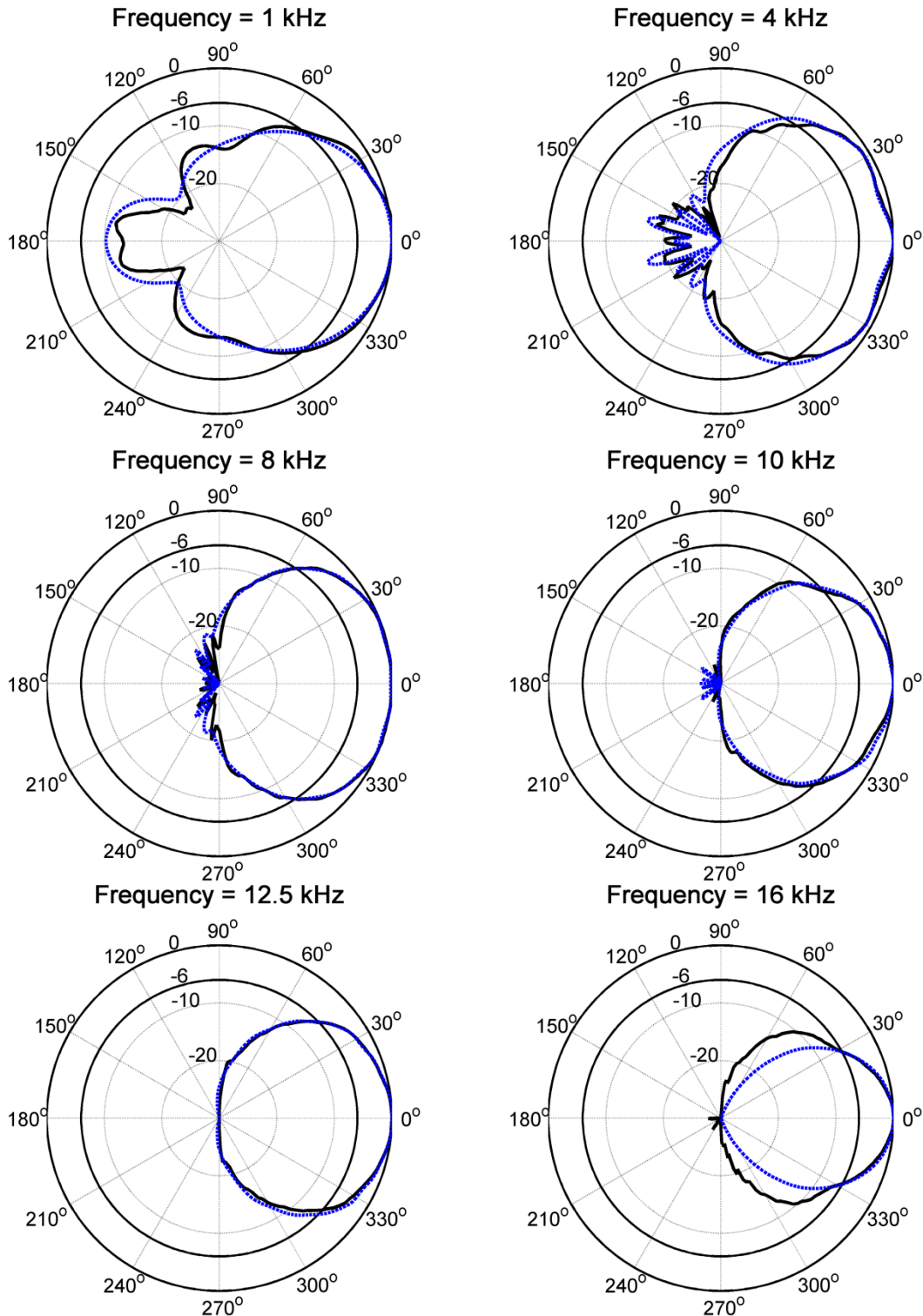


FIG. 4.5. Comparison of pressure directivity in dB (normalized to 0 dB) of a simulated $120^\circ \times 60^\circ$ horn (---) and experimental measurement (—). The decibel value is indicated radially and 0 degrees is on-axis with the horn. The 120° slice is shown.

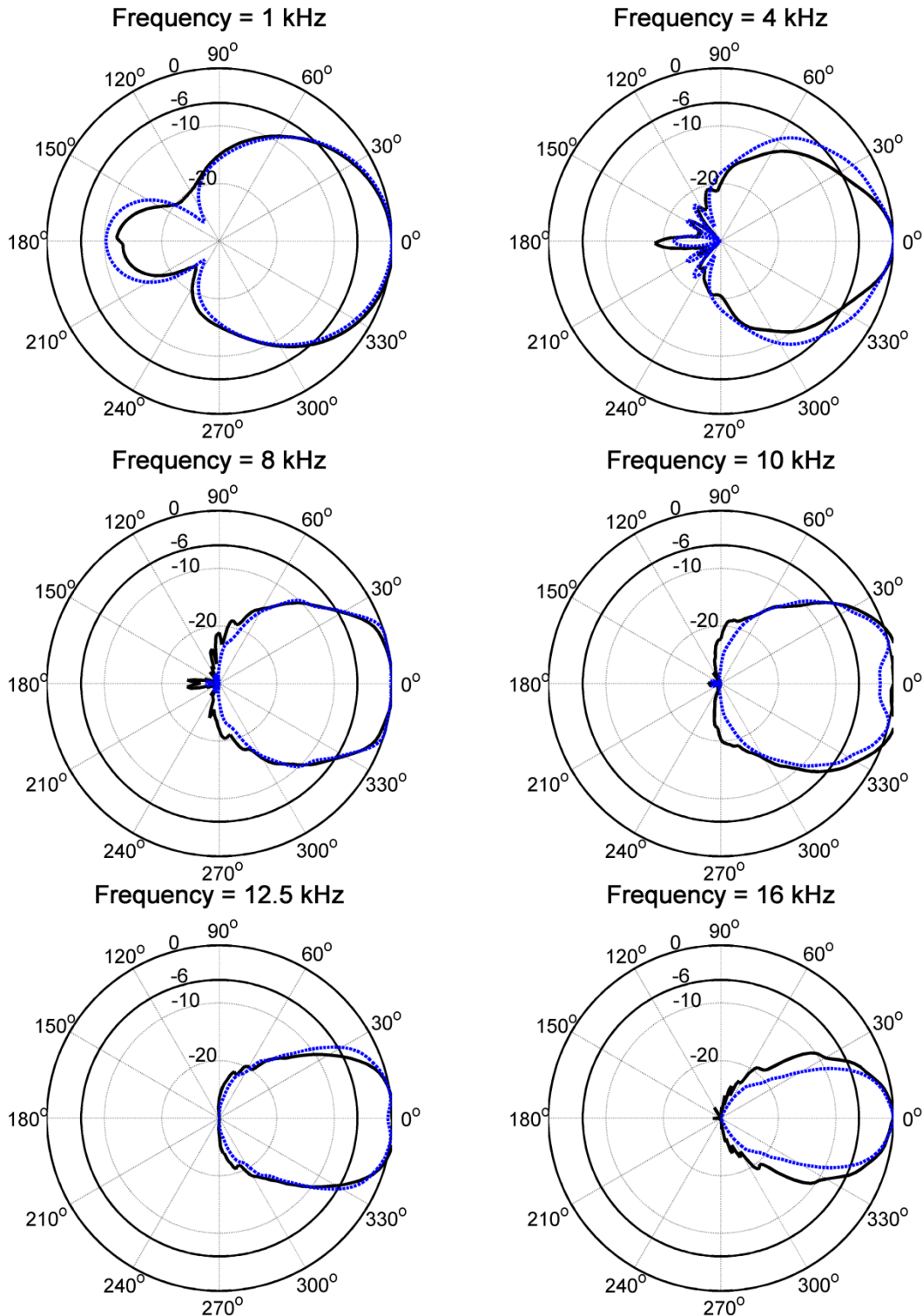


FIG. 4.6. Comparison of pressure directivity in dB (normalized to 0 dB) of a simulated $120^\circ \times 60^\circ$ horn (---) and experimental measurement (—). The decibel value is indicated radially and 0 degrees is on-axis with the horn. The 60° slice is shown.

For both horns, simulation data compare well with experimental data at 10 kHz and below. The disagreement may be due to the minimal changes due to including more frequencies in each directivity pattern (as done experimentally). Other factors such as potential rocking of the diaphragm at high frequencies and non-rigid horn boundaries for the experimental measurement may also contribute to some of the minor differences in off-axis radiation. Above 10 kHz, the simulation significantly diverges from the experimental measurements. To verify that higher-frequency discrepancies were not due to the coarseness of the model, the mesh was refined by increasing the number of elements by several thousand and the simulation was rerun for the $30^\circ \times 45^\circ$ horn. The refined model showed no difference in the far-field directivities, demonstrating that the less-refined mesh was sufficient. No difference in the directivities of the two meshes also confirmed the disagreements between simulation and experiment for frequencies above 10 kHz. Although complete agreement between simulation and experiment is not shown, the results presented in this section demonstrate the validity of the BEM simulations for most frequencies. The departure of numerical simulation with experimental measurements at higher frequencies is explained in more depth in [Sec. 4.4](#).

4.3 Input Wavefront Study

Once the limitations of BE simulations are understood (through comparison with respective experimental data), a study involving variation of the input wavefront and its effect on far-field pressure radiation is undertaken. The main idea of this study is to observe the changes in directivity and frequency response as a wavefront, constant in both magnitude and phase, is made nonplanar. Three different curvatures were studied: (1) an outward curvature, (2) no

curvature (planar), and (3) an inward curvature. The radius of curvature for both the inward and outward curvature was 2.54 cm (1 inch). The radius of the horn at this input boundary is approximately 1.75 cm (0.69 in.). A pictorial illustration of each curvature is shown in Fig. 4.7. They are not drawn to scale, but are intended to illustrate the general curvature orientations.

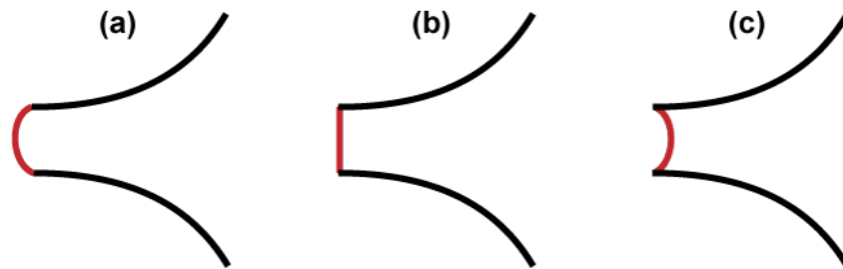


FIG. 4.7. Illustration of the different curvatures used for input wavefront study: (a) an outward curvature, (b) no curvature, and (c) an inward curvature. Not drawn to scale.

4.3.1 Comparative Study of Directivity

Wavefront curvature was studied using the BEM. Since the wavefronts produced by the diaphragm of the compression driver are ideally only moving in the direction along the length of the horn (the z -axis), a constant velocity in this direction is the prescribed boundary condition for all cases under study.

Figures 4.8 and 4.9 compare all cases for the $30^\circ \times 45^\circ$ horn. Figure 4.10 and 4.11 compare all cases for the $120^\circ \times 60^\circ$ horn. As seen in the previous study, the directivity patterns for all three cases are almost identical below 10 kHz. At 10 kHz and above, there are significant discrepancies. The directivities associated with all three cases for the $120^\circ \times 60^\circ$ horn do not diverge significantly until above 12.5 kHz for the 120° cross section (see Fig. 4.10). This is the only cross section between both horns that with a pipe-like geometry for part of its boundary.

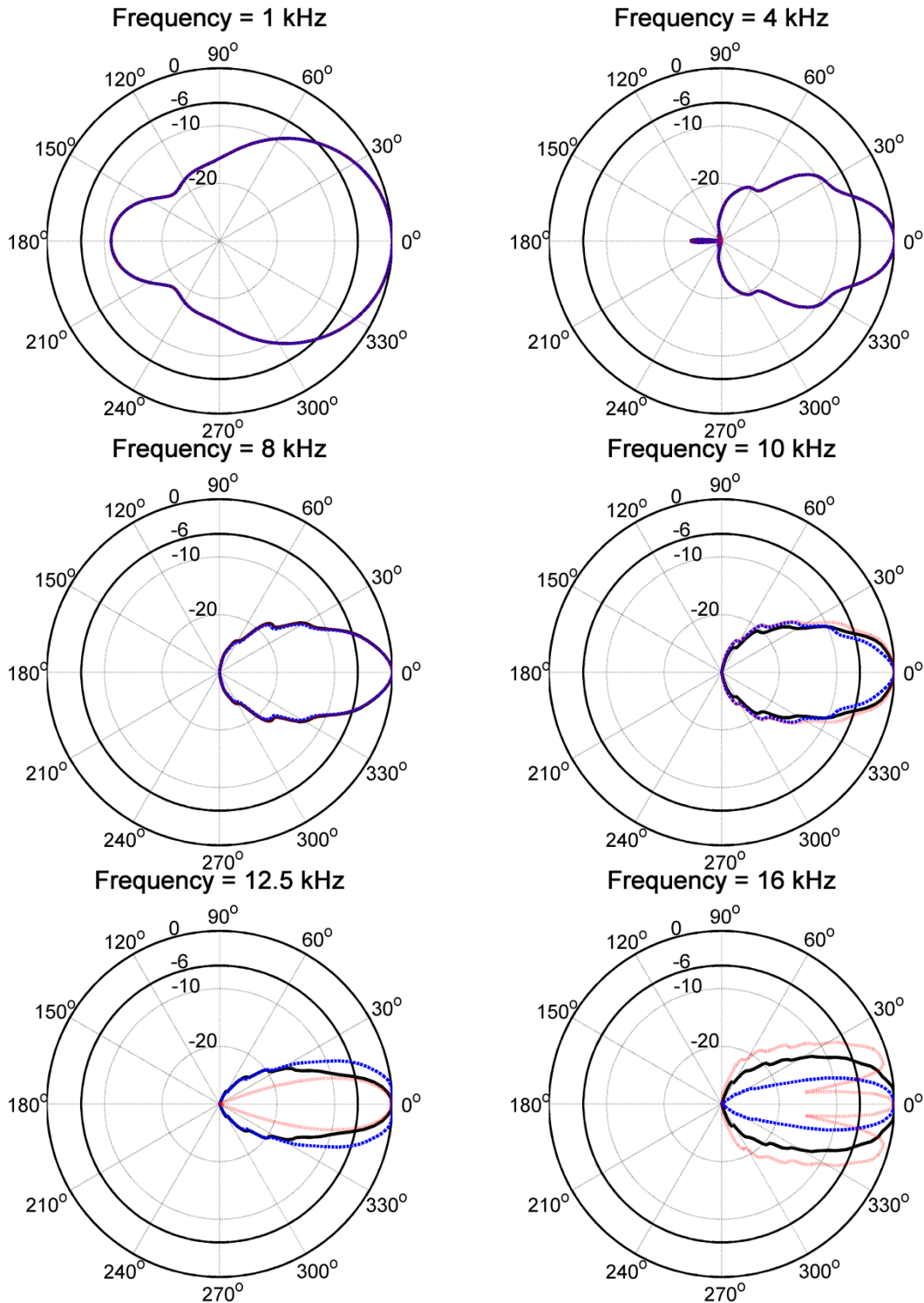


FIG. 4.8. Comparison of pressure directivity in dB (normalized to 0 dB) of a simulated 30° x 45° horn inward (---), outward (····), and no curvature (—). The decibel value is indicated radially and 0 degrees is on-axis with the horn. The 30° slice is shown.

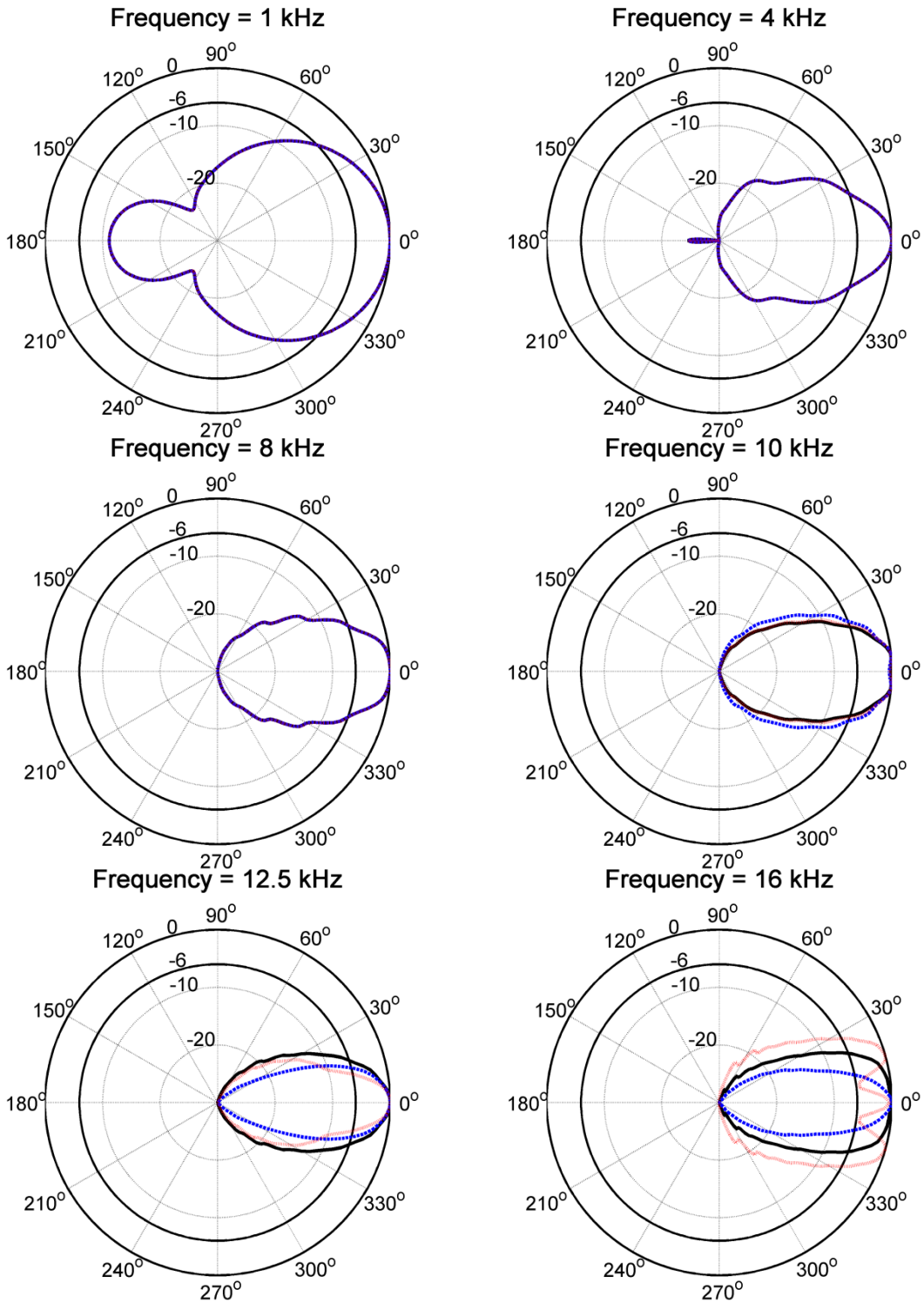


FIG. 4.9. Comparison of pressure directivity in dB (normalized to 0 dB) of a simulated 30° x 45° horn inward (---), outward (····), and no curvature (—). The decibel value is indicated radially and 0 degrees is on-axis with the horn. The 45° slice is shown.

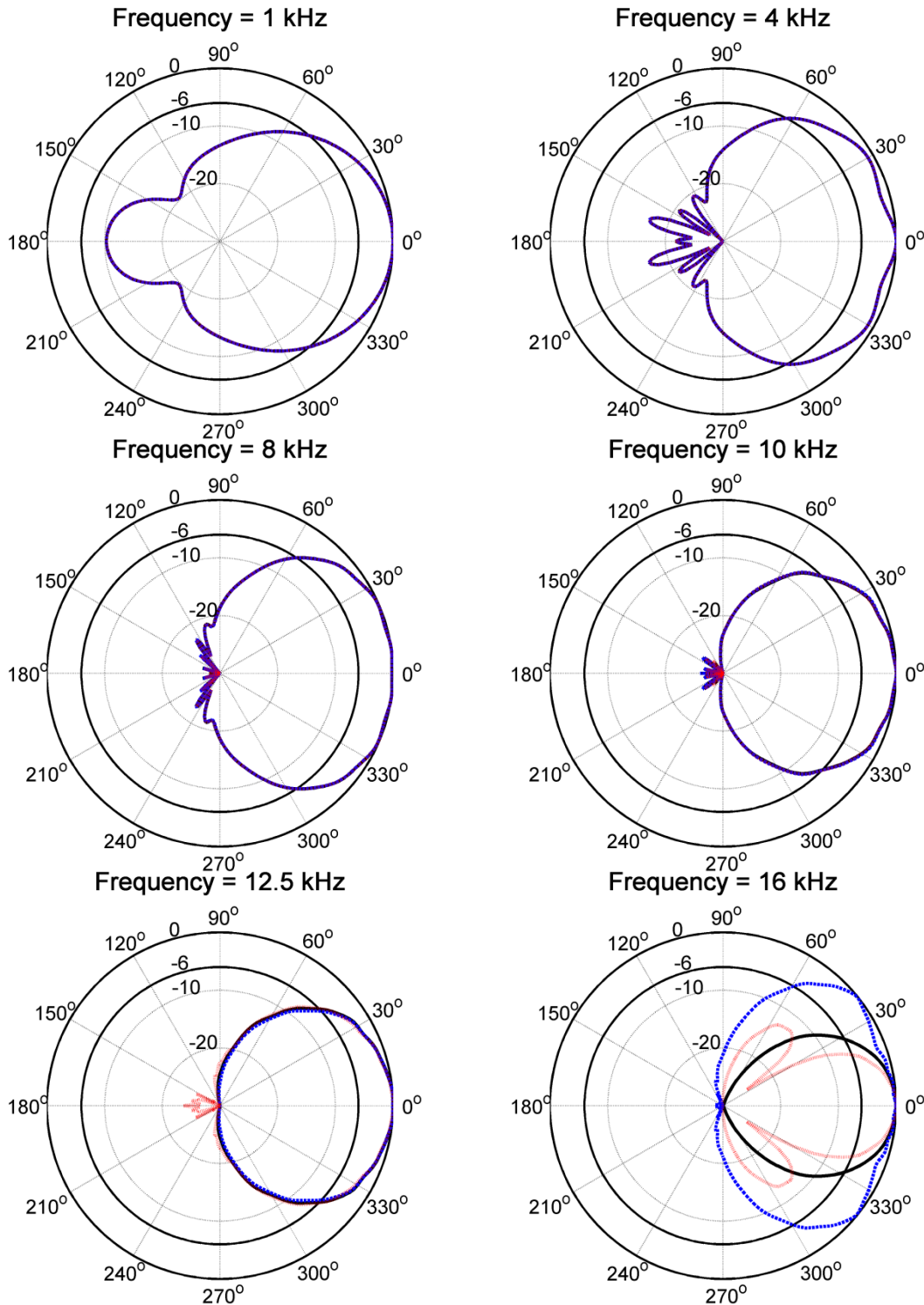


FIG. 4.10. Comparison of pressure directivity in dB (normalized to 0 dB) of a simulated $120^\circ \times 60^\circ$ horn inward (---), outward (....), and no curvature (—). The decibel value is indicated radially and 0 degrees is on-axis with the horn. The 120° slice is shown.

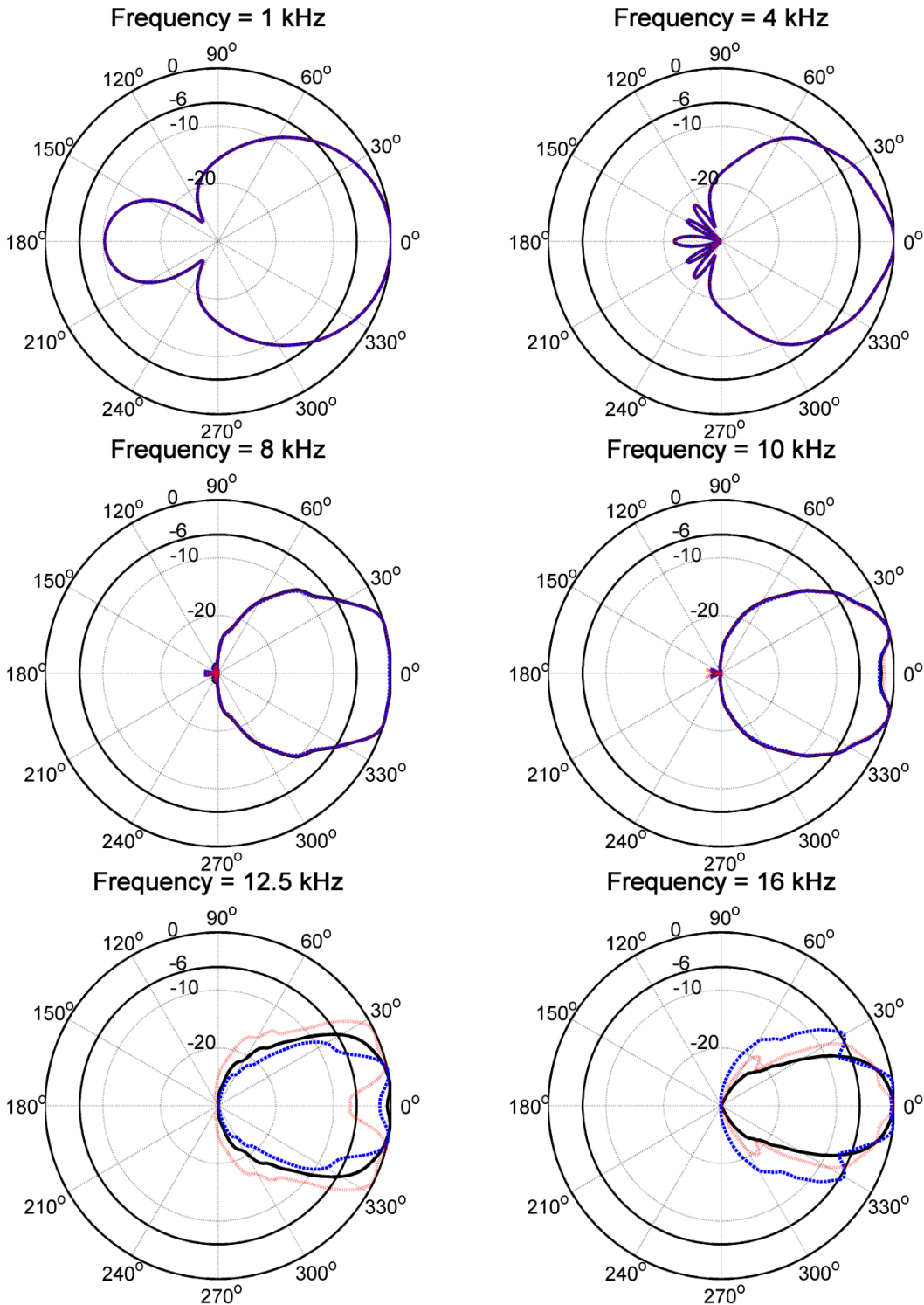


FIG. 4.11. Comparison of pressure directivity in dB (normalized to 0 dB) of a simulated $120^\circ \times 60^\circ$ horn inward (---), outward (....), and no curvature (—). The decibel value is indicated radially and 0 degrees is on-axis with the horn. The 60° slice is shown.

Although all of the directivity plots compared here are computed using only the center frequency for each one-third octave band, many of the discrepancies between different curvatures may be less significant if multiple frequencies were used.

As discussed in [Sec. 3.4](#), radiation from a pipe, or horn, is highly dependent on modal excitation. For all curvatures considered in this section, the transfer of energy to each mode of a given horn will most likely occur differently. Also, evanescence occurs in horns as it does in pipes. Excitation signals at frequencies below the cutoff frequency for the first higher-order mode will rapidly create wavefronts of constant magnitude as each one propagates down the horn. A far-field consequence of this phenomenon is that directivities look similar—even with different wavefront curvatures. Thus, normalized directivity patterns should appear similar until higher-order modes can significantly affect radiation. The frequency at which higher-order modes begin to propagate depends upon the horn geometry.

4.3.2 Comparative Study of Frequency Response

Although, no significant differences in the normalized directivity patterns were observed below 10 kHz, overall output levels did differ. Figure 4.12 compares the unnormalized on-axis frequency responses for the $30^\circ \times 45^\circ$ horn with each type of curvature. Figure 4.13 compares the unnormalized on-axis frequency response for the $120^\circ \times 60^\circ$ horn with each curvature. A constant excitation velocity of approximately 2.08 m/s was used for each simulation to compare acoustic radiation for a given source velocity. Results for the $30^\circ \times 45^\circ$ horn are louder by several dB than for the $120^\circ \times 60^\circ$ horn for much of the frequency range shown. This is likely due to the increased spreading of energy from the larger beamwidths of the $120^\circ \times 60^\circ$ horn.

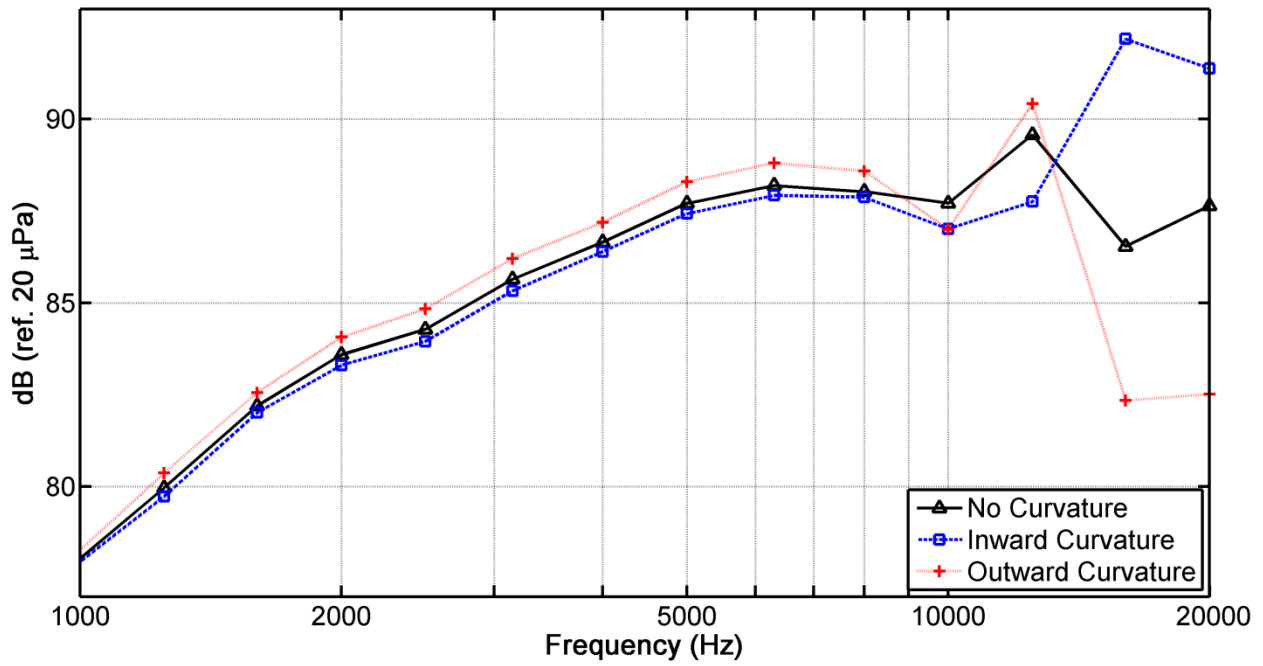


FIG. 4.12. Simulated results for on-axis frequency response of a 30° x 45° horn with different input wavefront curvatures.

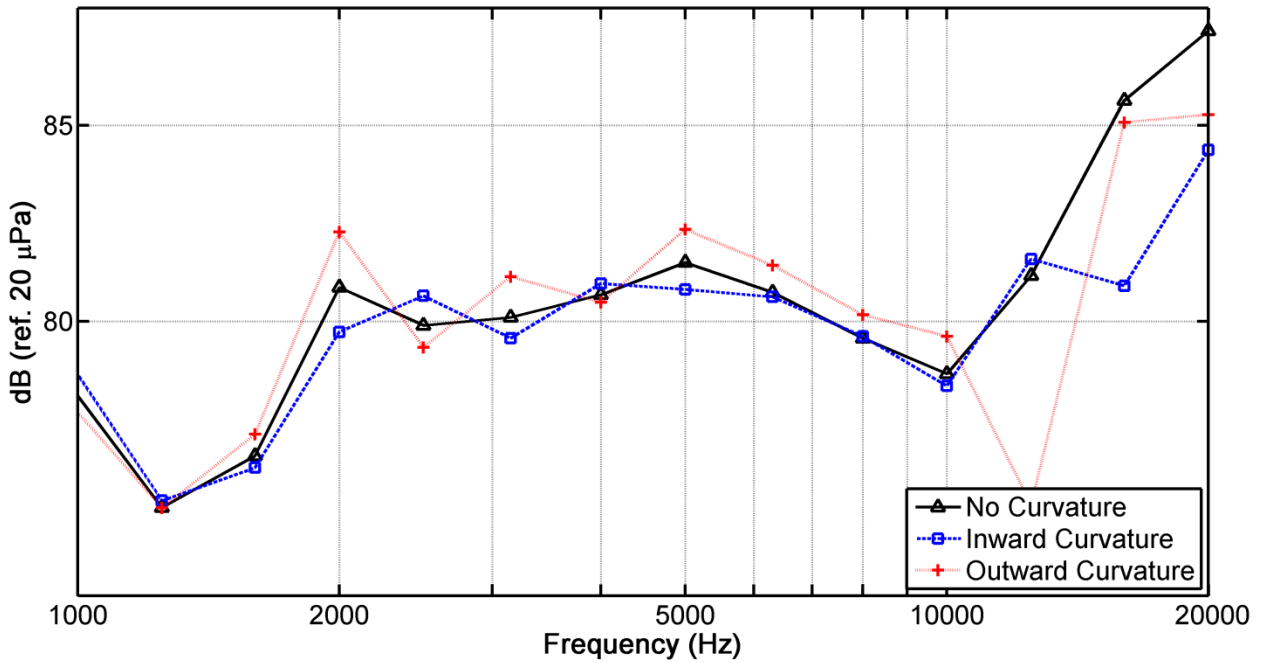


FIG. 4.13. On-axis frequency response numerical simulations of a 120° x 60° horn for different input wavefront curvatures.

The outward curvature (with the dome curving *away* from the mouth of the horn) generally performs better than flat and inward curvatures when comparing on-axis frequency response. The outward curvature performs consistently better for the $30^\circ \times 45^\circ$ horn below 10 kHz, and fluctuates considerably for the $120^\circ \times 60^\circ$ horn throughout the frequency band displayed. Similar results were also observed by Suzuki *et al.* in Refs. [56] and [57], who studied the difference in on-axis frequency response and directivity of inward and outward-curved domes in a semi-infinite pipe or infinite baffle, respectively. However, further work needs to be done to directly compare the current results with those done in Refs. [56] and [57] and apply them more generally to horns.

A possible application of these results may be in choosing a different “optimal” wavefront at the entrance of the horn. Traditionally, this wavefront is desired to be planar. However, the outward curvature profile, instead of the planar profile, gave greatest overall sound pressure level at the majority of frequencies simulated for one of the horns (the $30^\circ \times 45^\circ$ horn). On the other hand, each curvature may significantly affect the overall system by introducing large dips in the frequency response (as shown for the $120^\circ \times 60^\circ$ horn) and may significantly change the directivity.⁵⁷

4.4 Higher-Frequency Disagreement

For both the existing horn models and the models with a curved excitation source, BE simulations compare well with experimental data below 10 kHz. Normalized directivity patterns also look almost identical for all three curvatures under test below 10 kHz. In order to better understand this consistent divergence above this frequency, the horn may be compared to a pipe

at the entrance (throat) of the horn. If the pipe has the same radius as the entrance of the horn, then the approximate cutoff frequency for the first axisymmetric higher-order mode is approximately

$$f_N = \frac{c\alpha_{n_\phi, n_r}}{2\pi a} \approx 10,975.3 \text{ Hz}, \quad (4.2)$$

where the speed of sound c is 343 m/s, the radius of the pipe a is 19.05 mm (0.75 inches), and the α_{0, n_r} is approximated as 3.83 for the first higher-order mode. Additionally, if we consider a pipe the same length as the horn, the normalized contribution of the first higher-order mode is defined to be

$$A_{0,1} = e^{-i\sqrt{\left(\frac{2\pi f}{c}\right)^2 - \left(\frac{\alpha_{0,1}}{a}\right)^2} z}, \quad (4.3)$$

where f is the frequency of the excitation signal and z is the distance that the evanescent mode has traveled. Considering an excitation frequency of 10 kHz, the first higher-order mode will decay by about a factor of 10^{11} after 0.3048 meters (12 inches), the length of the hypothetical pipe. Hence, it is easily seen for a pipe that any higher-order modal contributions would be insignificant in the far field at and below 10 kHz.

Figure 4.14 shows the geometric differences of the two horns used for the simulations presented in this thesis. The $30^\circ \times 45^\circ$ horn is illustrated on the left and the $120^\circ \times 60^\circ$ horn is illustrated on the right. As previously explained, the $30^\circ \times 45^\circ$ horn deviates from experimental measurement around 10 kHz, and its geometry flares immediately. On the other hand, the $120^\circ \times 60^\circ$ horn does not deviate from the experimental measurement until after 12.5 kHz, and its flare does not occur until half way down through the horn.

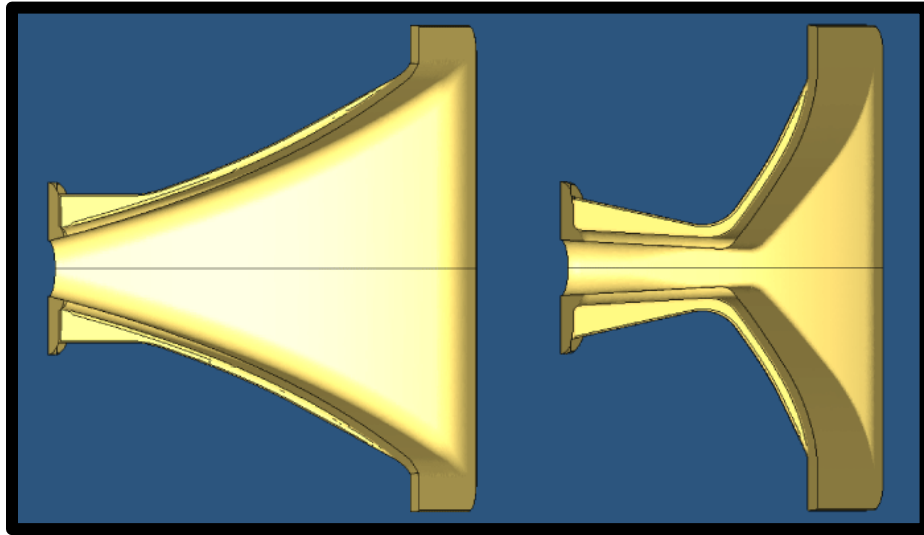


FIG. 4.14. Side view of the horns simulated in Sec. 4.3. The 30° cross section of the $30^\circ \times 45^\circ$ horn is shown on the left and the 120° cross section of the $120^\circ \times 60^\circ$ horn is shown on the right.

Although pipe modes and cutoff frequencies can be very different than those for a similar length horn, their analytical analysis is helpful as a horn can be thought of as a composition of several very small-length pipes. As the radius of the pipe gets larger, the amount of evanescence imposed on higher-order modes decreases. Thus, the amount of higher-order modal decay caused by a pipe will be larger than that caused by a horn. Figure 4.15 through 4.20 show the magnitude of the interior pressure field for both cross sections of the $120^\circ \times 60^\circ$ horn. The 120° cross section is similar to a pipe for the beginning portion of its geometry and prevalent decay of higher-order modes are observed at and below 10 kHz (see Fig. 4.15). In contrast, the 60° cross section opens up very quickly (similar to both cross sections of the $30^\circ \times 45^\circ$ horn) and higher-order modes contribute much sooner. Significant amounts of higher-order modes appear to propagate much farther down the length of the horn for the 60° cross section even at 4 kHz (see Fig. 4.17).

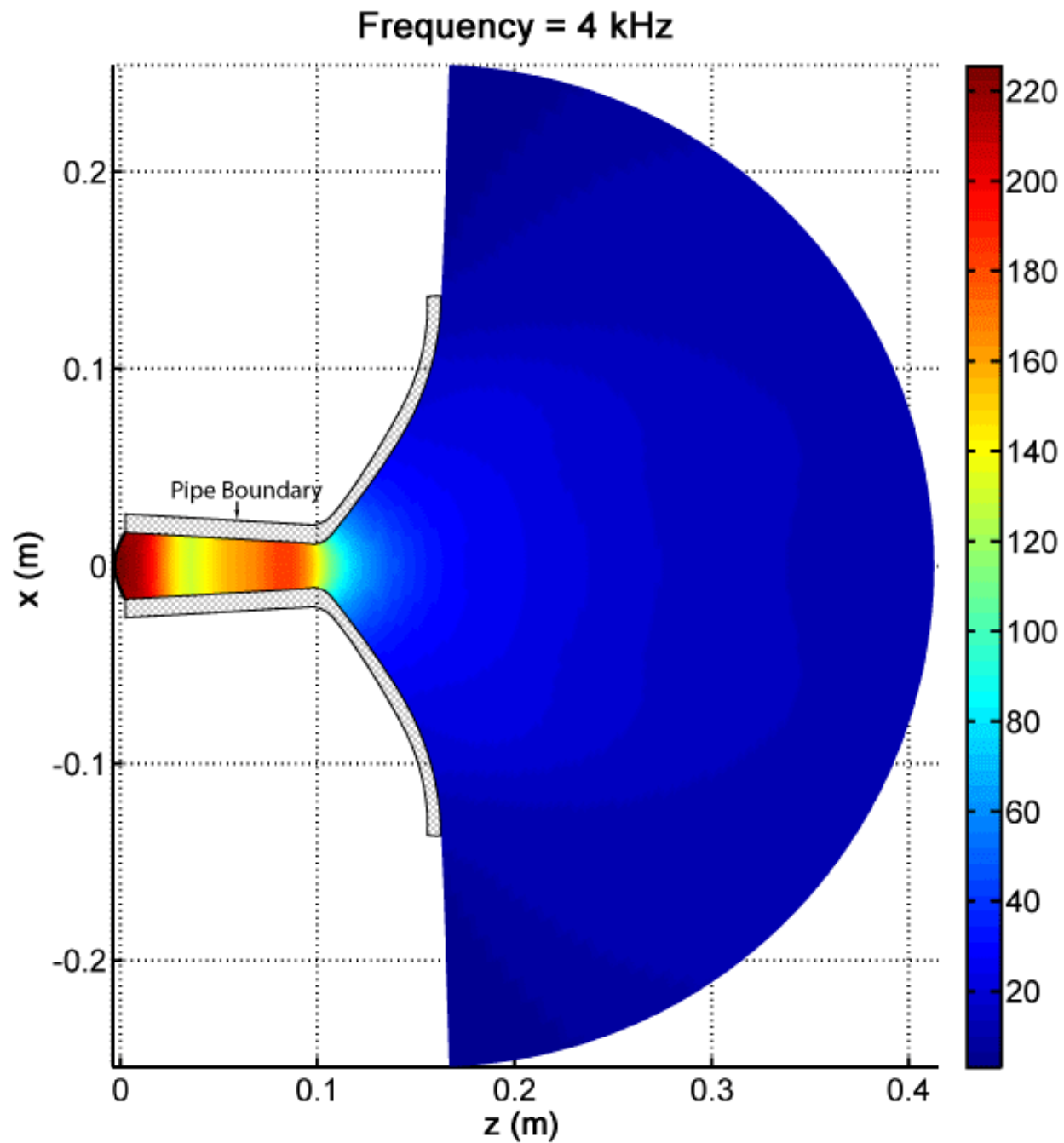


FIG. 4.15. Pressure magnitude of the interior pressure field for the 120° x 60° horn along the 120° cross section at 4 kHz.

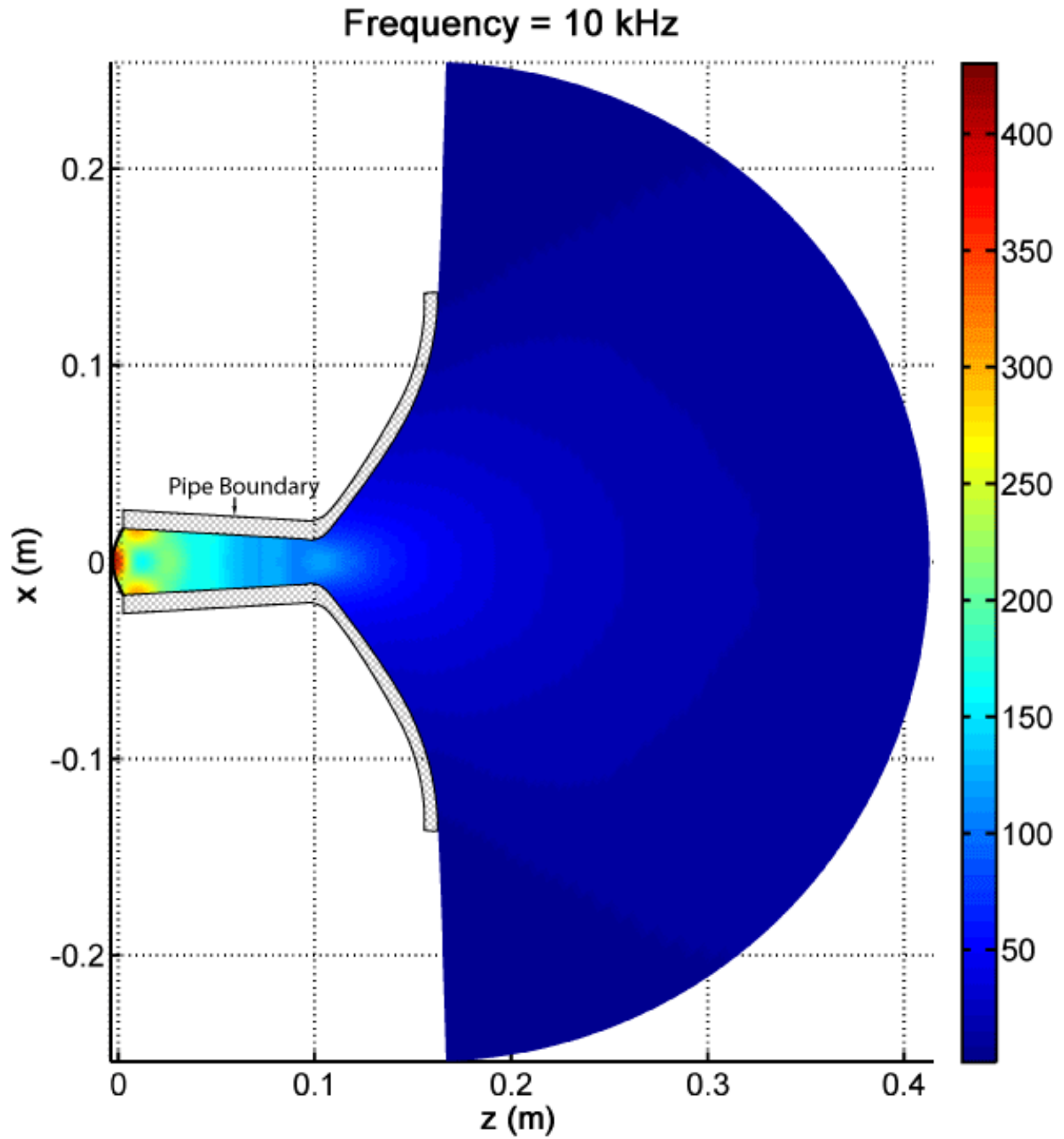


FIG. 4.16. Pressure magnitude of the interior pressure field for the $120^\circ \times 60^\circ$ horn along the 120° cross section at 10 kHz.

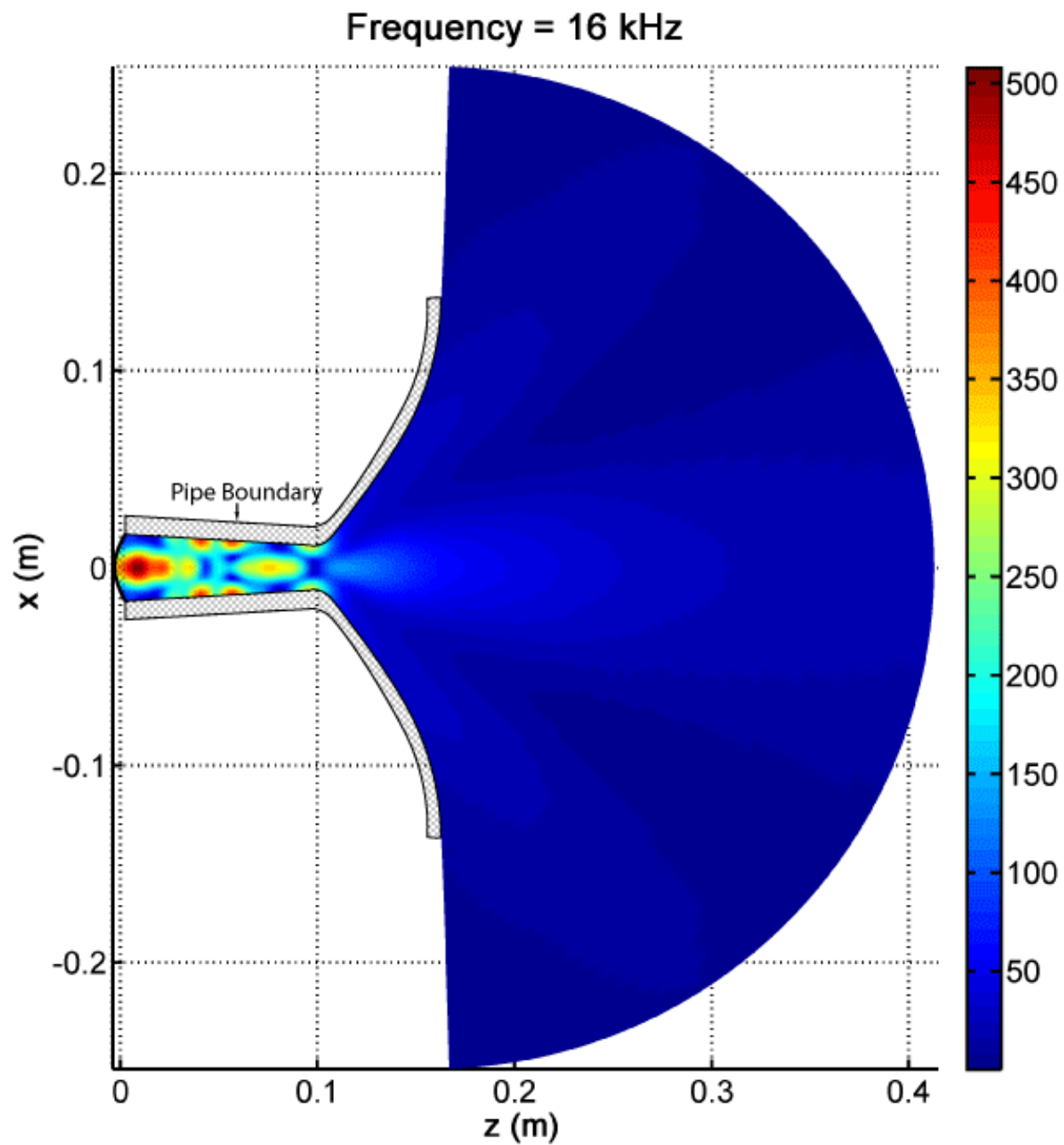


FIG. 4.17. Pressure magnitude of the interior pressure field for the $120^\circ \times 60^\circ$ horn along the 120° cross section at 16 kHz.

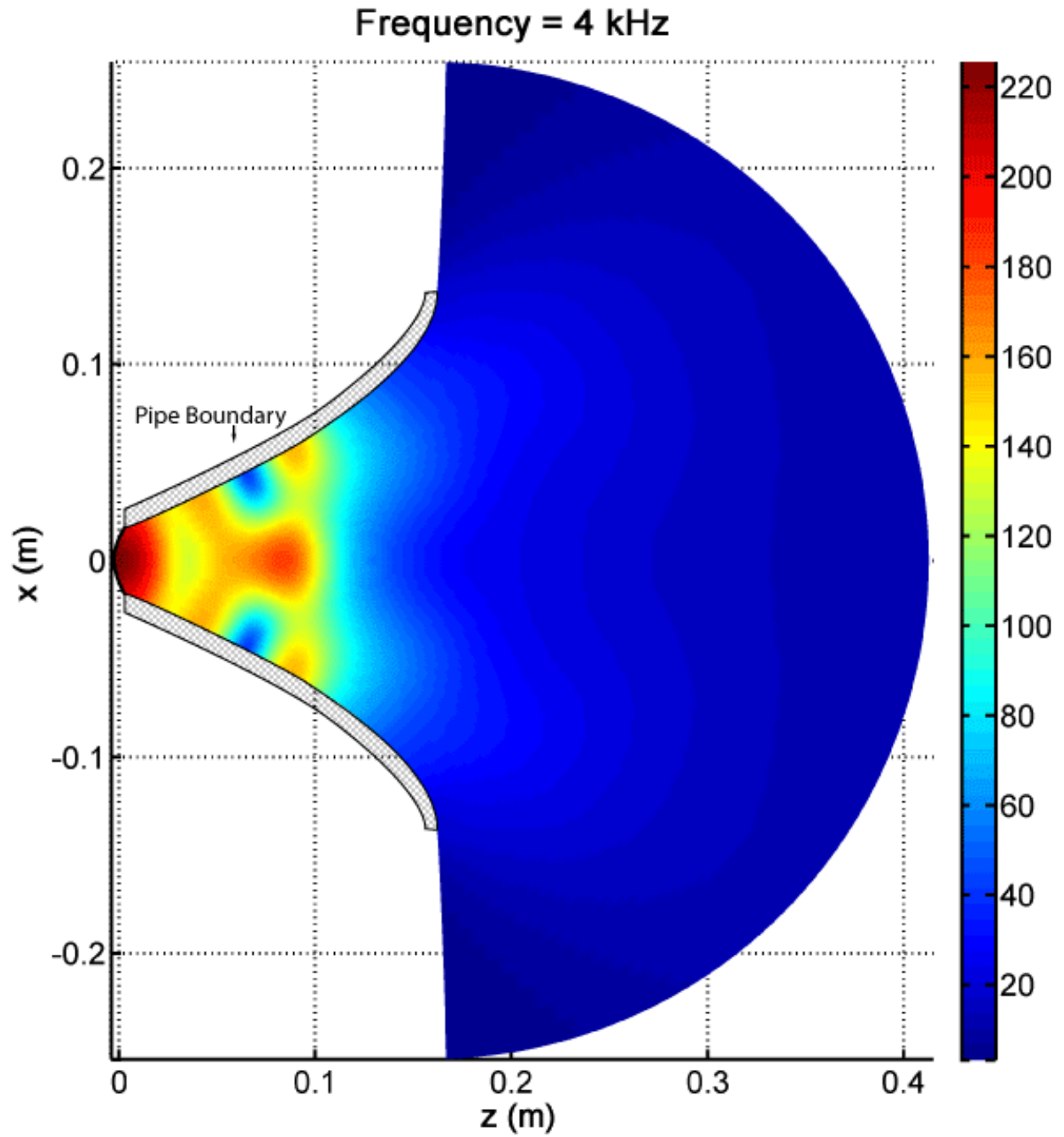


FIG. 4.18. Pressure magnitude of the interior pressure field for the $120^\circ \times 60^\circ$ horn along the 60° cross section at 4 kHz.

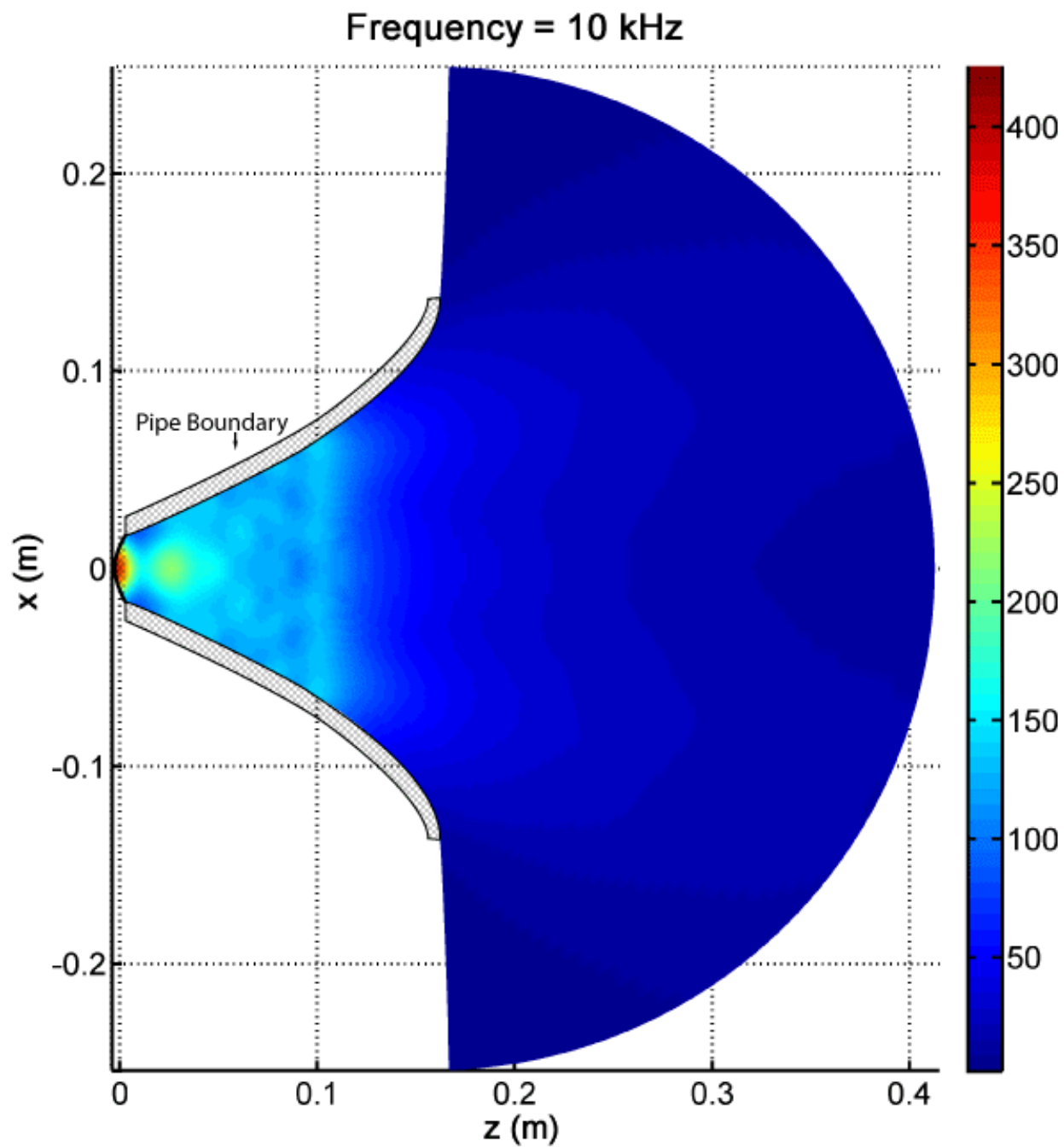


FIG. 4.19. Pressure magnitude of the interior pressure field for the $120^\circ \times 60^\circ$ horn along the 60° cross section at 10 kHz.

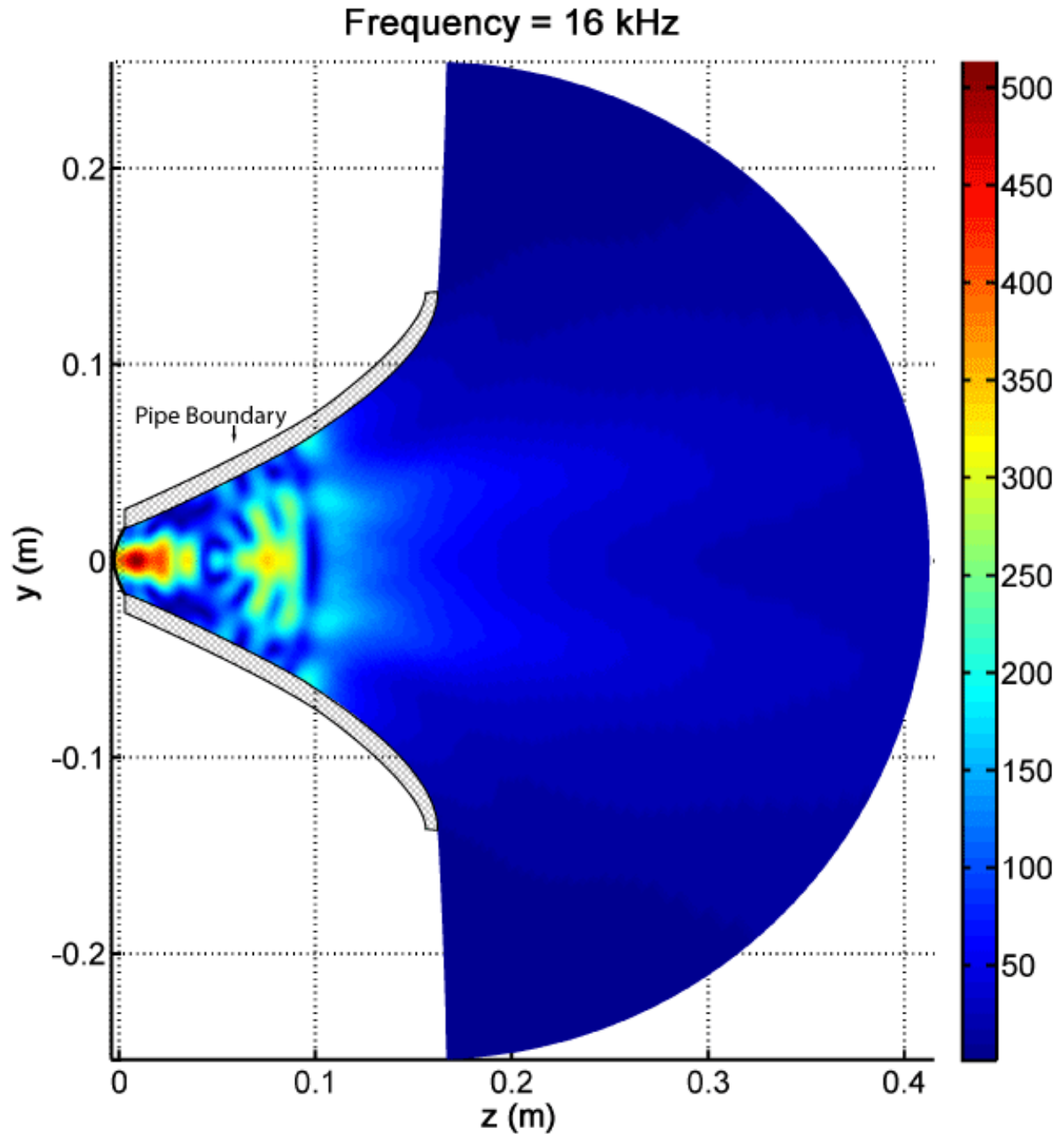


FIG. 4.20. Pressure magnitude of the interior pressure field for the $120^\circ \times 60^\circ$ horn along the 60° cross section at 16 kHz.

As seen in the preceding figures, higher-order modes are seen to be computationally insignificant at a frequency well below the cutoff frequency for the first higher-order mode,

where only the plane-wave mode contributes to far-field pressure radiation. Although higher-order modes do not evanesce as much within a horn, a similar phenomenon is observed. The $120^\circ \times 60^\circ$ horn agrees with the experimental measurement at higher frequencies, likely because of the pipe-like effects of the first half of its geometry, causing more rapid higher-order evanescence than in the $30^\circ \times 45^\circ$ horn.

Higher-frequency disagreement may also be a manifestation of the incorrect representation of physical excitation source. The excitation source used in the BE simulations is piston like where a physical diaphragm would break up into modes, coincidentally, at frequencies around the cutoff frequency for higher-order pipe modes. As a result, when the excitation signal is well below the cutoff frequency, such that experimental measurement and numerical simulation are reduced to single-mode propagation, simulation and experiment agree. Otherwise, the simulation cannot accurately assign relative amplitude and phase to propagating pipe modes, without an accurate displacement profile for the diaphragm, which results in incorrect far-field pressure predictions for higher frequencies.

4.5 Conclusions

The results presented in this chapter highlight several important features that should be emphasized in horn design. First, the modal components of wave propagation through the horn greatly affect the far-field pressure radiation. This has been shown for steady-state analysis and is likely also true in transient analysis (as seen from the results shown in Ch. 3). While unnormalized radiation levels for different wavefront curvatures may change for low frequencies, normalized directivity patterns are not altered until higher-order modes contribute

significantly in the overall radiated energy. At high enough frequencies, when higher-order modes do propagate, the effect of each mode is significant enough that even a slight change in the coefficients of the propagating modes produces notable changes in the far-field response of the system.

A more in-depth study of various excitation wavefronts may challenge the long-held belief that a planar wavefront is most desirable at the entrance of the horn. The outward curvature produced larger sound pressure levels over a significant range of frequencies for one of the cases presented. However, the results for a more pipe-like horn suggest that radiation efficiency will heavily depend on horn geometry. Comparisons of frequency response were only presented on-axis; off-axis frequency response, though not shown here, does not produce the same result. Further research will need to be done to confirm the general application of this result.

It may be tempting for a designer to decrease the size of the entrance of the horn to only allow plane wave (zeroth order) mode propagation through the horn throat over the entire audio bandwidth. Though not addressed in this thesis, a smaller horn entrance introduces distortion due to acoustic nonlinearities sooner for lower amplitude signals, which debilitates the sound reproduction system. Thus, real progress in horn design will need to control radiation patterns while incorporating higher-order cross-sectional modes of the horn.

Finally, it must be remembered that the results presented in this chapter were obtained by modeling horns only. The compression driver was not included in the models. Chapter 5 will present results including the coupling of a compression driver to a horn. Chapter 5 will also show that the modes of a diaphragm greatly affect the radiation from a horn-loaded compression driver.

Chapter 5

Steady-State Analysis of Horn-Loaded Compression Drivers

5.1 Background

The compression driver is commonly employed by many sound reproduction systems, and is generally used for reproducing frequencies above about 1 kHz. A compression driver is composed of several parts. The most pertinent components to this research are the diaphragm (a spherical cap typically made of titanium, aluminum, etc.) and the phase plug. Although these components vary in size and relative proportion, almost every compression driver design uses them. From an acoustical standpoint, the channels in the phase plug are not the only important aspects of the compression driver. The throat of the compression driver (volume of air from the phase plug exit to the compression driver exit) and the compression chamber (volume of air

between the diaphragm and the entrance of the phase plug) are also important when analyzing the acoustic qualities of the compression driver. Figure 5.1 depicts an illustration of the cross section of a compression driver. Each of the aforementioned components in the compression driver is indicated numerically.

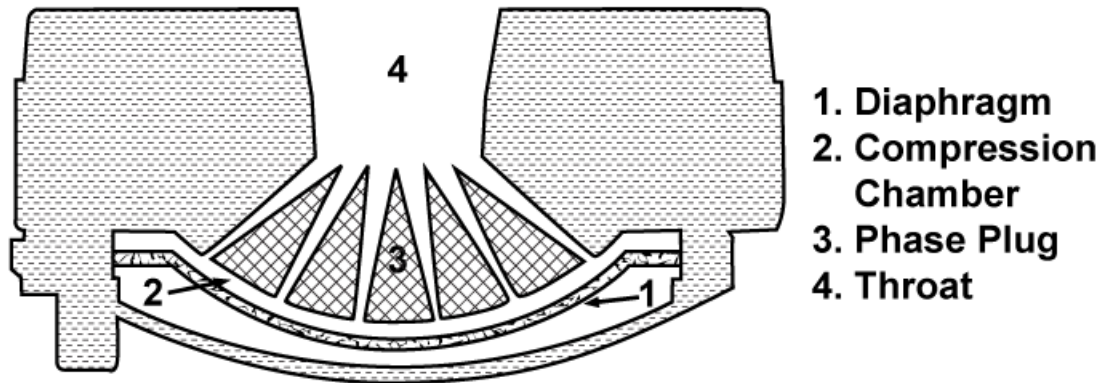


FIG. 5.1. Illustration of the cross section of a compression driver. The illustration is motivated by an Electrovoice ND6 compression driver schematic. Drawing not to scale.

The compression driver transforms electric energy to mechanical energy then to acoustic energy. The research on compression drivers in this thesis separately considers some of their mechanical and acoustical properties.

The study of the mechanical properties focuses on the modal vibrations of the diaphragm. For low-frequency excitation, the vibration of the diaphragm is spatially coherent (piston like), similar to the boundary condition assigned in an ideal numerical simulation. As frequency increases, however, the diaphragm begins to vibrate in its higher-order modes. When this occurs, spatial coherence is reduced and acoustic radiation fluctuates considerably.

In order to create more accurate models, necessary coupling of these domains should be incorporated into the numerical studies performed. As seen in previous chapters, popular

numerical simulations showing promise in this area of research include the finite-difference methods (FDM),⁵⁸ finite-element methods (FEM)⁵⁸⁻⁵⁹, and boundary-element methods (BEM).⁶⁰ Barlow used both the FDM and FEM to better design both coned and metal diaphragms such that prominent modal breakup would occur at different frequencies, outside of the audible bandwidth [58]. While understanding of mechanical vibration of diaphragms with certain shapes and materials has progressed, acoustic radiation was not included in these models.⁵⁸⁻⁵⁹ Others were more concerned with the radiation modes exiting from a compression driver, but simplification of the source (similar to Ch. 4), gaining a better understanding of acoustic radiation without taking into account mechanical vibrations of the dome.⁶⁰⁻⁶¹ Even experimental procedures like laser vibrometer were used to scan diaphragm vibrations to obtain mode shapes, but an understanding of these vibrations on subsequent radiation was not addressed.⁶² Other aspects of research on diaphragms have included curvature (typically spherical) affects acoustic radiation,^{57,61} or how the small chambers housing the voice coil cause problematic resonances (i.e., parasitic resonance dips in the overall system frequency response).⁶³ Two-port networks to model the radiation from both the compression driver and horn as individual components has also been shown to help speed up design of each component with fairly good agreement to experimental data.⁶⁴

This work attempts to use laser vibrometry scans to increase accuracy of modal vibrations in the numerical models (isolated within the mechanical domain), while eventually incorporating them into a boundary-element (BE) simulations to understand the mechanical effects on far-field radiation. Some laser vibrometry scans are presented that were used to extract the natural modes of the diaphragm. And BE simulation of the analytical reconstruction of the mechanical vibrations is shown as well.

Additionally, this chapter will help to better understand the role of the phase plug in terms of the subsequent acoustic radiation. One of the earliest pioneers in phase plug research was Smith. He compared several frequency response measurements of compression drivers and found that annular-ring channels in phase plug design suppressed higher-order modes of the diaphragm best (and produced the smoothest frequency response).⁶⁵ Though one can find earlier research publications on the phase plug,⁶⁶ the industry has had success with the original design proposed by Smith.⁶⁷⁻⁶⁹ Murray gave much recognition to Smith's work within the loudspeaker community upon his own research in this field of study.⁶⁷ Both Henricksen⁶⁸ and Dodd *et al.*⁶⁹ compared many of Smith's original proposed designs to their own proposed designs. Of the many designs tested, Smith's annular-ring design consistently performed better. All of the designs simulated in this chapter are annular-ring designs.

The phase plug is incorporated into the compression driver to improve radiation efficiency and wavefront coherence. The radiation efficiency is greatly improved because it reduces the overall amount of movable fluid within the compression driver, thereby providing a higher impedance loading to match the high mechanical impedance (of the diaphragm). Wavefront coherence is improved due to the consistent geometric path length between the diaphragm and the exit of the compression driver. If a wavefront arrives at the exit of the phase plug and adds with another wavefront destructively, radiation is severely reduced. Thus, the goal of the phase plug is to provide equal path lengths for the sound to travel from the various points of the diaphragm to the exit of the driver,⁷⁰ ideally creating a constant-phase wavefront at the exit of the phase plug.

Traditionally, researchers have focused only on the phase of the emerging wavefront from the compression driver. However, Geddes points out that this is not sufficient for a planar

response at the exit of the compression driver.⁷¹⁻⁷² In order for a wavefront to aggregate as a plane wave, both the phase *and magnitude* must be equal for a given cross section.

The phase plug study performed in this chapter uses the BEM to analyze seven different designs. The numerical simulation of each prototype may help to design a more coherent acoustic pathway, which may also increase acoustical radiation. Because any changes in the cross-sectional area of the acoustic pathway must be included in the analysis, the entire acoustic pathway of the compression driver and horn are part of the BE simulations. The purpose of this study is not only to determine whether these modifications improve upon the performance of an existing design, but to also demonstrate the how the use of numerical simulations improves upon traditional prototyping procedures. A major benefit of conducting numerical simulations of phase plug designs is the savings in cost and time in comparison to building and testing them experimentally, since changes can more easily be made to numerical models. Mechanical vibrations are not included in this experiment, although both horns and compression drivers are part of each simulated model.

5.2 The Diaphragm

The excitation source of the compression driver is the diaphragm. Attached to the diaphragm is a coil of wire through which an alternating current (the audio signal) flows. Because of its interaction with a fixed magnetic field, this induces a force which pushes the diaphragm back and forth, creating sound. Ideally, the diaphragm moves coherently, its entire geometry oscillating at a constant amplitude and phase. This, however, is not the case over the entire frequency range under consideration due to modal breakup of the diaphragm.

The diaphragm design under consideration (see Fig. 5.2) is complex. It is not well defined by a single coordinate system, and thus is extremely difficult to evaluate analytically. The corrugations that line the edge of the spherical dome make the analytical definition of the geometry intractable. For analytical analysis purposes, the diaphragm geometry is simplified to a spherical cap alone.

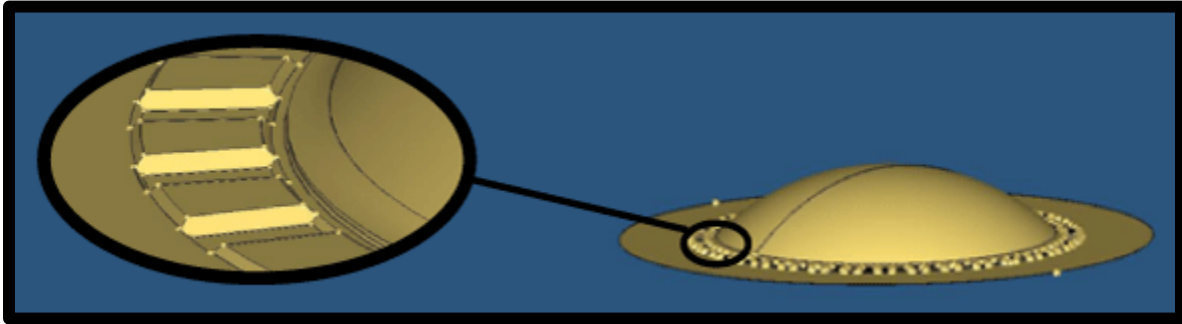


FIG. 5.2. Illustration of the compression driver diaphragm.

5.2.1 Natural Modes

The natural modes of a spherical cap may be derived analytically. The following is based on the derivation found in Ref. [73], but with additional explanations.

Using thin plate theory, the partial differential equation for a circular plate is

$$D\nabla^4 u_3 + \rho h \frac{\partial^2 u_3}{\partial t^2} = 0, \quad (5.1)$$

where D is the bending stiffness, and ρ and h are the density and thickness of the given plate respectively. The variable u_3 is the displacement normal to the surface of the plate at a given location and time, and is the variable we wish to solve for.

If the radius of curvature of a spherical cap is large enough, its geometry and vibrational behavior approach that of a circular plate. The governing equations of motion are similar. For a spherical cap, a stiffness term Eh/R_c^2 is included, where E is Young's modulus, h is the thickness of the plate, and R_c is the radius of curvature. If this extra term is included in Eq. (5.1) and u_3 is assumed to be time harmonic, the expression for a spherical cap is approximated as

$$D\nabla^4 U_3 + \left(\frac{Eh}{R_c^2} - \rho h \omega^2 \right) U_3 = 0, \quad (5.2)$$

where $u_3 = U_3 e^{j\omega t}$. Thus, Eq. (5.2) must be solved for U_3 , the displacement component moving normal to the plane in which the geometry of the *circular plate* was defined (the z -axis).

In order to solve the equation, the fourth-order derivative must first be simplified. This is accomplished by factoring U_3 from each term of Eq. (5.2), and then creating two useable terms with second-order derivatives. By doing so, Eq. (5.2) becomes

$$\begin{aligned} D\nabla^4 U_3 + \left(\frac{Eh}{R_c^2} - \rho h \omega^2 \right) U_3 &= \left[\nabla^4 - \frac{1}{D} \left(\rho h \omega^2 - \frac{Eh}{R_c^2} \right) \right] U_3, \\ &= [\nabla^4 - \lambda^4] U_3, \\ &= [\nabla^2 + \lambda^2][\nabla^2 - \lambda^2] U_3 = 0, \end{aligned} \quad (5.3)$$

where $\lambda^4 = \frac{1}{D} \left(\rho h \omega^2 - \frac{Eh}{R_c^2} \right)$.

Each bracketed term in Eq. (5.3) renders specific and solvable equations. They are solved by assuming U_3 has two independent solutions for its motion in each direction of its coordinate system, $U_3 = R(r)\Theta(\theta)$. This method is known as *separation of variables*. Thus, expanding Eq. (5.3) in terms of r and θ gives

$$\begin{aligned}
[\nabla^2 \pm \lambda^2]U_3 &= [\nabla^2 \pm \lambda^2]R\Theta, \\
&= \left(\frac{\partial^2}{\partial r^2} + \frac{1}{r} \frac{\partial}{\partial r} + \frac{1}{r} \frac{\partial^2}{\partial \theta^2} \pm \lambda^2 \right) R\Theta = 0, \\
&= \frac{r^2}{R} \frac{\partial^2 R}{\partial r^2} + \frac{r}{R} \frac{\partial R}{\partial r} + \frac{1}{\Theta} \frac{\partial^2 \Theta}{\partial \theta^2} \pm \lambda^2 r^2 = 0. \tag{5.4}
\end{aligned}$$

After variables R and Θ are separated, Eq. (5.4) is solved. First, the Θ component is solved since it is grouped into one term. Since r and θ have been completely separated from one another, their complete terms in Eq. (5.4) must equal a constant. Thus,

$$\frac{1}{\Theta} \frac{\partial^2 \Theta}{\partial \theta^2} = -n^2, \tag{5.5}$$

where n^2 is a constant. The normalized solution for Θ is

$$\Theta = \cos n(\theta - \phi), \tag{5.6}$$

where ϕ is a phase factor so that the nodal lines can be shifted in θ depending on the boundary conditions.

The complete solution for R from Eq. (5.4) [after substitution of Eq. (5.5)] is

$$\frac{r^2}{R} \frac{\partial^2 R}{\partial r^2} + \frac{r}{R} \frac{\partial R}{\partial r} \pm \lambda^2 r^2 = n^2. \tag{5.7}$$

Equation (5.7) is Bessel's equation and provides four different solutions. Bessel functions of the first and second kinds, $J_n(\lambda r)$ and $Y_n(\lambda r)$ respectively, are solutions when the $+\lambda^2 r^2$ term is used, and the modified Bessel functions $I_n(\lambda r)$ and $K_n(\lambda r)$ are solutions when the $-\lambda^2 r^2$ term is used. Thus, the complete solution for R is written as

$$R = A_1 J_n(\lambda r) + A_2 Y_n(\lambda r) + A_3 I_n(\lambda r) + A_4 K_n(\lambda r), \tag{5.8}$$

where $A_1, A_2, A_3,$ and A_4 are constants. Thus, the expression for U_3 is given as

$$\begin{aligned}
U_3 &= R\theta \\
&= (A_1 J_n(\lambda r) + A_2 I_n(\lambda r) + A_3 Y_n(\lambda r) + A_4 K_n(\lambda r)) \cos(n(\theta - \phi)). \quad (5.9)
\end{aligned}$$

Equation (5.9) is simplified through the application of boundary conditions. First, the amplitude of the spherical cap must be finite at the origin. Because both $Y_n(\lambda r)|_{r=0}$ and $K_n(\lambda r)|_{r=0}$ are undefined, A_3 and A_4 must be zero. Second, because this method is to be used for higher frequencies, where laser vibrometer scans of the dome have revealed minimal displacement and velocity at the edge of the spherical cap, the boundary condition at $r = a$ (where a is the radius of the spherical cap) is roughly approximated as being rigid. In order for a rigid condition to be applied at $r = a$, the displacement and velocity in the z -axis are specified to be zero at this boundary.

To solve for coefficients A_1 and A_2 by mere substitution is difficult. Instead, the linear system of equations is solved by matrix analysis. The matrix is formed by including both the boundary condition for zero displacement and its derivative,

$$\begin{bmatrix} J_n(\lambda a) & I_n(\lambda a) \\ \frac{\partial J_n(\lambda a)}{\partial r} & \frac{\partial I_n(\lambda a)}{\partial r} \end{bmatrix} \begin{bmatrix} A_1 \\ A_2 \end{bmatrix} = \begin{bmatrix} 0 \\ 0 \end{bmatrix}. \quad (5.10)$$

This expression is satisfied if the determinant of the matrix of Bessel functions is zero. Hence, the determinant must satisfy the relationship

$$J_n(\lambda a) \frac{\partial I_n(\lambda a)}{\partial r} - \frac{\partial J_n(\lambda a)}{\partial r} I_n(\lambda a) = 0. \quad (5.11)$$

The roots of this equation indicate when the system undergoes resonance (the system's natural frequencies). They are found by putting the expression for λ in terms of ω . Therefore,

$$\frac{1}{D} \left(\rho h \omega^2 - \frac{Eh}{R_c^2} \right) = \lambda^4,$$

$$\rho h \omega^2 = D \lambda^4 + \frac{Eh}{R_c^2},$$

$$\omega^2 = \frac{1}{\rho h} \left(D \lambda^4 + \frac{Eh}{R_c^2} \right). \quad (5.12)$$

Since $\omega^2 = D\lambda^4/\rho h$ for a flat, circular plate, Eq. (5.12) can be viewed as an expression for the natural frequencies of a flat plate plus a correction term based on the radius of curvature and material properties of the spherical cap. Recall that this equation is only valid when the spherical cap only has slight curvature. Because the diaphragm of the compression driver used in this chapter extends to $\pi/4$ in our polar angle, this approximation may be insufficient.

The natural modes derived for the spherical cap closely resemble those of a circular plate. Figure 5.3 shows a few of these modes, which are later compared to experimental data from an actual diaphragm, obtained using a Scanning Laser Doppler Vibrometer (SLDV).

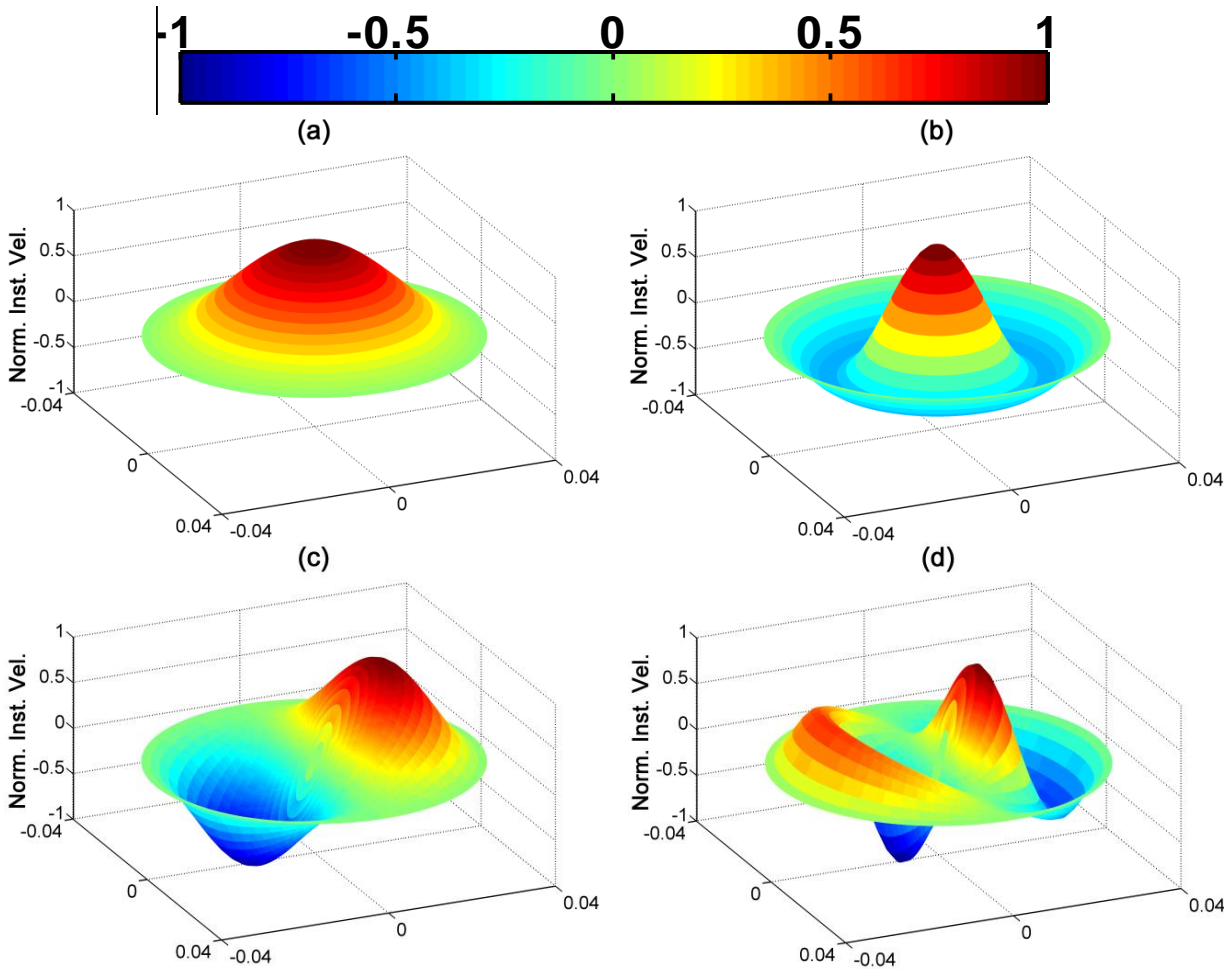


FIG. 5.3. Predicted modes for a spherical cap. Mode: (a) (0,0); (b) (0,1); (c) (1,0); (d) (1,1).

This derivation may be improved by deriving the natural modes in spherical coordinates. This would require fewer approximations and would place no restriction on the curvature of the dome. Another possible improvement would result by refining the boundary condition at $r = a$. Because the voice-coil, which is located near $r = a$, is moving with the diaphragm, it may be more appropriate to have a small, non-zero displacement and/or velocity at the boundary, instead of the rigid condition assumed in the derivation, or to model this diaphragm boundary as a free boundary (with the second and third derivatives of the geometric slope into the boundary equaling zero).

5.2.2 SLDV Scans

The SLDV is used to measure vibration (displacement, velocity, or acceleration) of a given structure perpendicular to a user-defined plane. It may be used to find frequencies where a single natural mode dominates the systems response, or it may be used to decompose a system's complex vibrational response into its analytical modes. In order for the SLDV to extract structural velocity information, a laser beam shines on the structure of interest. The diaphragm, the structure to be measured, is enclosed within the outer casing of a standard compression driver and its view is obstructed to the laser. Thus, the back of one compression driver is cut away to allow an unobstructed view for the SLDV's laser. This alters the acoustic loading seen by the diaphragm, and the natural modes extracted with the SLDV are altered. Although the acoustic loading may significantly change the modal contributions of the structural vibration, the diaphragm still vibrates as a summation of natural modes which allows the derived natural modes to be tested. Further work, proposed at the end of this section, suggests other ways to maintain the proper acoustic loading and still allow experimental extraction of the modes with the SLDV.

After the data are extracted from the SLDV, a least-squares fitting is conducted using the previously derived natural modes. The problem is constructed in a least-squares sense,⁷⁴

$$\Psi \bar{x} = \bar{b}, \quad (5.13)$$

where vector \bar{x} represents the unknown coefficients for each natural mode in matrix Ψ . Each element in \bar{x} can be complex and is the desired information from Eq. (5.13). Vector \bar{b} is formed by organizing the data measured with the SLDV. Matrix $\Psi = \{\psi_1, \psi_2, \dots, \psi_n\}$, where each column of the matrix Ψ represents a natural mode. Each column is m points long, which

corresponds to the total number of scan points from the SLDV. Although formation of vector \bar{b} does not require any particular order, the discrete spatial location for the i^{th} entry must be the same for all columns in matrix Ψ . In other words, each row for Ψ and \bar{b} must correspond to the same spatial location on the spherical cap. Usually, the first dozen modes are more than enough for most problems within the audio bandwidth. This was observed experimentally as modes above lowest twelve had very small coefficients. Other times, the number of natural modes used to formulate Ψ after the SLDV scans were observed visually.

Equation (5.13) is solved by applying an orthogonality condition. For a surface, this condition is written as

$$\int_s \psi_n \psi_m dS = \begin{cases} 1, & n = m \\ 0, & n \neq m, \end{cases} \quad (5.14)$$

for a continuous system, or

$$\Psi^* \Lambda \Psi = I, \quad (5.15)$$

for a discrete system, where I is the identity matrix, Ψ^* is the Hermitian of Ψ , and Λ represent the discrete differentials,

$$\Lambda = \begin{bmatrix} r dr d\theta & 0 & \dots & 0 \\ 0 & r dr d\theta & 0 & \vdots \\ \vdots & 0 & \ddots & 0 \\ 0 & \dots & 0 & r dr d\theta \end{bmatrix}. \quad (5.16)$$

By using the discrete form of orthogonality, Eq. (5.13) is solved for \bar{x} as follows:

$$\begin{aligned} \Psi \bar{x} &= \bar{b}, \\ \Psi^* \Lambda \Psi \bar{x} &= \Psi^* \Lambda \bar{b}, \\ \bar{x} &= \Psi^* \Lambda \bar{b}. \end{aligned} \quad (5.17)$$

The first attempt to reconstruct the data with the analytically derived natural modes was with a scan centered around 12.8 kHz. The scan was taken of an existing ND6 compression driver diaphragm (see Fig. 5.1) while producing white noise. It was mounted to a vibration-free table, oriented such that the diaphragm and exit of the compression driver were parallel with the table (oriented as if mounted in a loudspeaker box). The back of the driver is removed and the driver does not have any front loading.

Figure 5.4(a) compares the instantaneous velocity data obtained with the SLDV, and Fig. 5.4(b) shows the reconstructed instantaneous velocity using Eq. (5.17). The modes in the SLDV data seem well defined at this frequency, and appear similar to the modes used for the fitting.

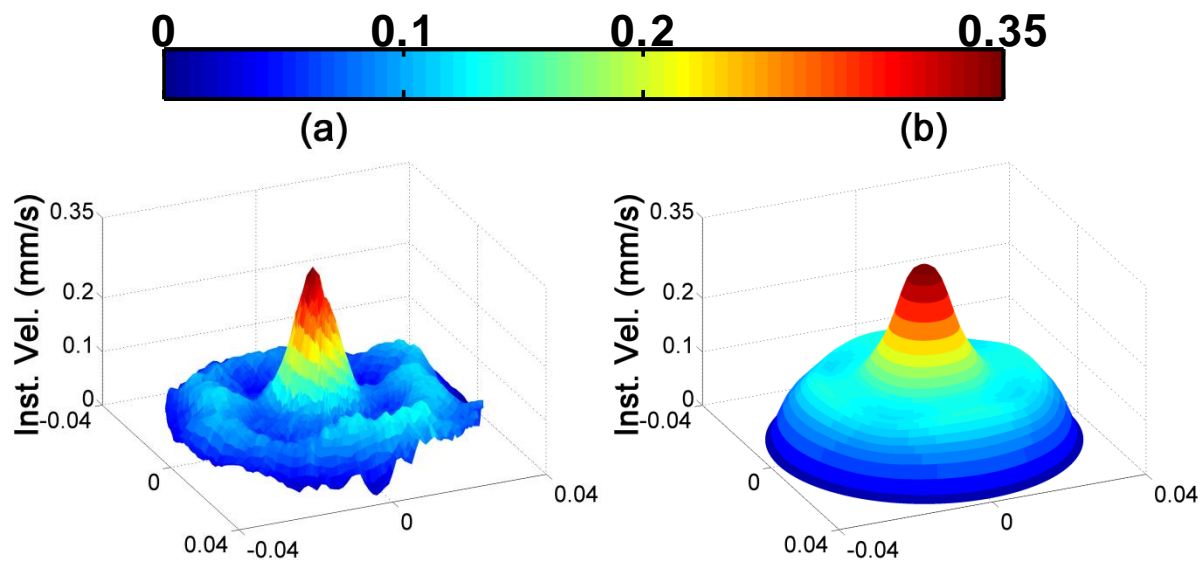


FIG. 5.4. Spatial velocity profiles of a compression driver diaphragm driven at 12.8 kHz. (a) SLDV data used for reconstruction. (b) Reconstruction of Scanning Laser Doppler Vibrometer (SLDV) data using natural modes.

With moderate accuracy, the excitation pattern at 12.8 kHz from the SLDV is reconstructed with the analytically derived natural modes. To determine whether this

reconstruction technique is reproducible with different acoustical loadings, other scans at 12.5 kHz, 16 kHz, and 20 kHz with different acoustical loads were performed. These scans show how changes in acoustical loading might affect the vibrational response of the diaphragm. Four different scans were performed at each frequency, changing the front loading but keeping the back open for the scans. The four different acoustical loads mounted to the front of the compression driver are as follows: (1) with no additional loading, (2) mounted to a 30° x 45° horn, (3) with clay loaded around the entire edge of the exit of the driver (completely blocking the outside channel of the phase plug), and (4) with clay loaded around half the edge of the exit of the driver. The scans with different acoustical loadings were intended to provide some insight into the effect of removing the back cap of the compression driver with regard to the diaphragm vibrations. Although removal of the back cap may change the vibrational information of the diaphragm much differently, drastic changes in the front loading may suggest the rough magnitude of change that one might expect with removal of the back cap. Differences in modal contributions are illustrated in Figs. 5.5 and 5.6 after complex instantaneous velocities of various SLDV scans are subtracted from one another. Prominent modal patterns still exist where the acoustic loading closer to the diaphragm changes more drastically. While the maximum error between the compression driver with the horn and alone is 4%, error up to 30% was observed between the compression driver with clay and alone. Errors for the other measurements fall between these two extremes. Larger differences occur as the changes in acoustical loading draw nearer to the diaphragm. If the modal contributions are the same, the magnitude of their difference is constant. These results are shown in Figs. 5.5(c) and 5.6(c). Figure 5.5 shows a comparison of the compression driver with and without clay in the outside channel of the driver

exit. Figure 5.6 shows a comparison of the compression driver with and without the horn mounted to it.

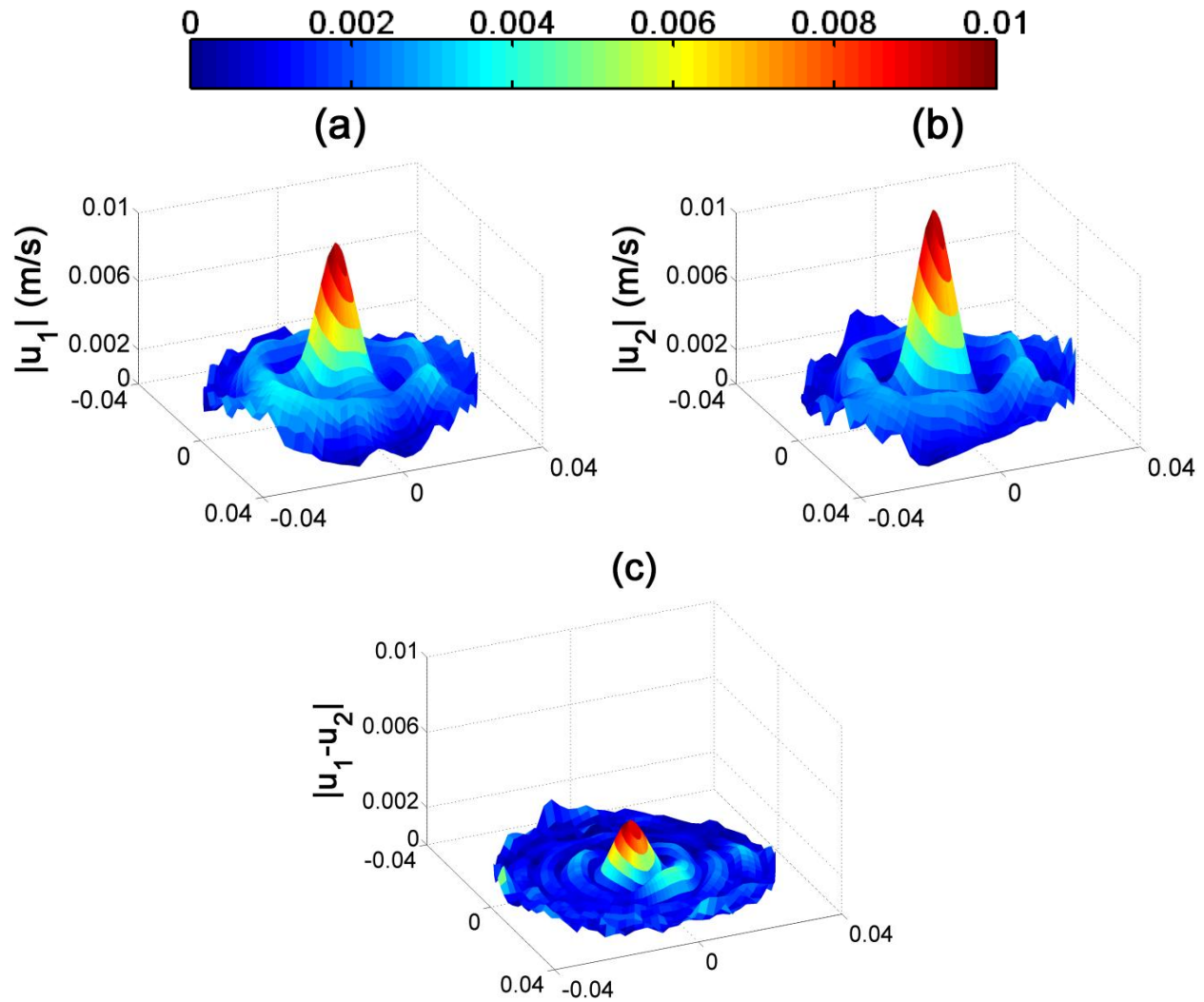


FIG. 5.5. (a) Scanning Laser Doppler Vibrometer (SLDV) measurement with no additional loading. (b) SLDV measurement with clay fit into outside edge of compression driver exit. (c) The magnitude of the difference of both velocity profiles.

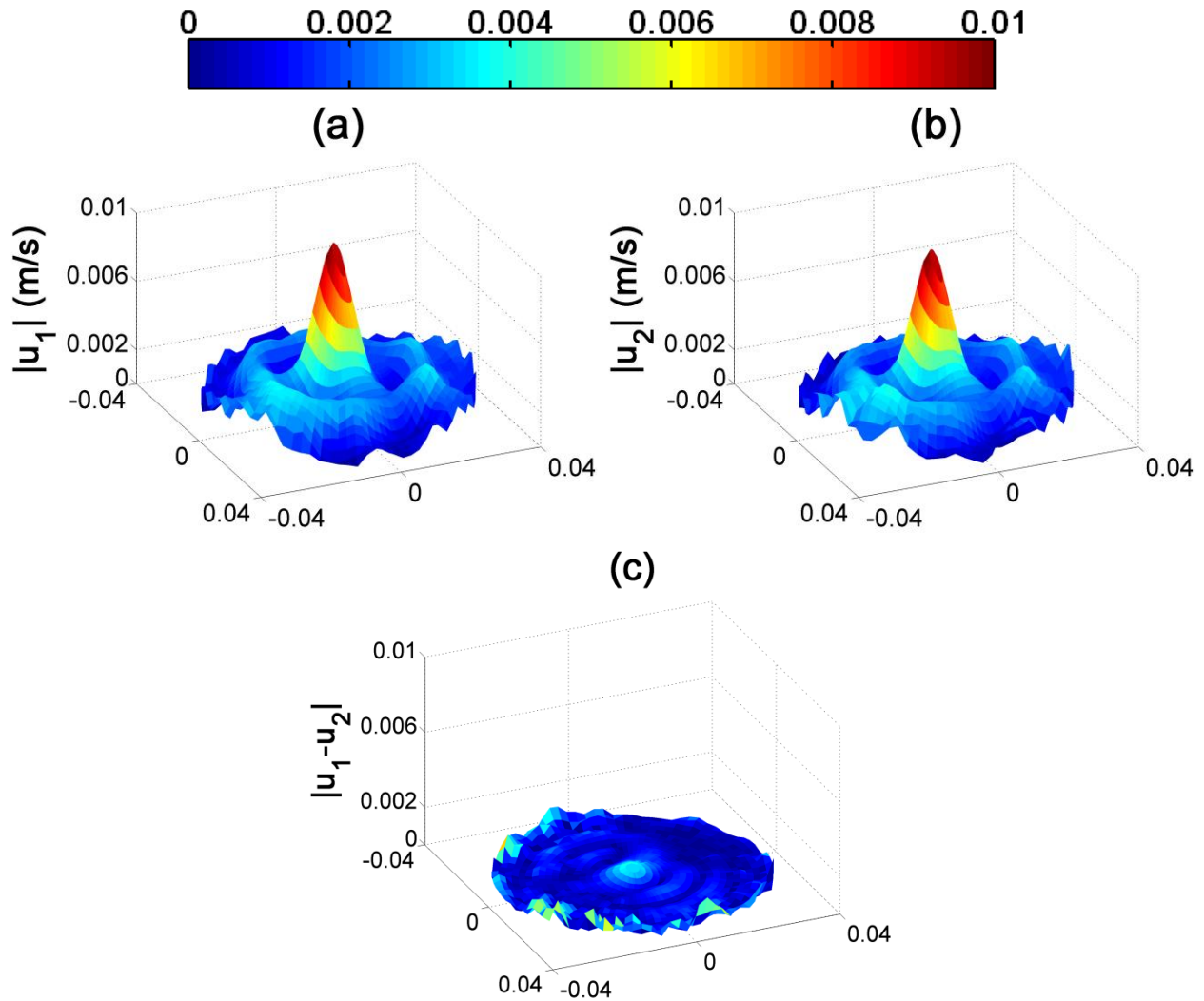


FIG. 5.6. (a) Scanning Laser Doppler Vibrometer (SLDV) measurement with no additional loading. (b) SLDV measurement with a $30^\circ \times 45^\circ$ horn mounted to the compression driver. (c) The magnitude of the difference of both velocity profiles.

The SLDV scans provide evidence that the vibrational modes of the diaphragm do change due to moderate acoustical loading changes. To better understand how much the vibrational response of the diaphragm has changed due to the removal of the back cap, BE

simulations are performed to compare experimentally measured radiation with simulated radiation using the diaphragm vibrations of the SLDV scan. Because the SLDV scans are not symmetric, as required for inputs into the BE models, the analytically reconstructed velocity is used instead. Figure 5.7 shows that the modal pattern input for the BE simulation does not match what is happening physically.

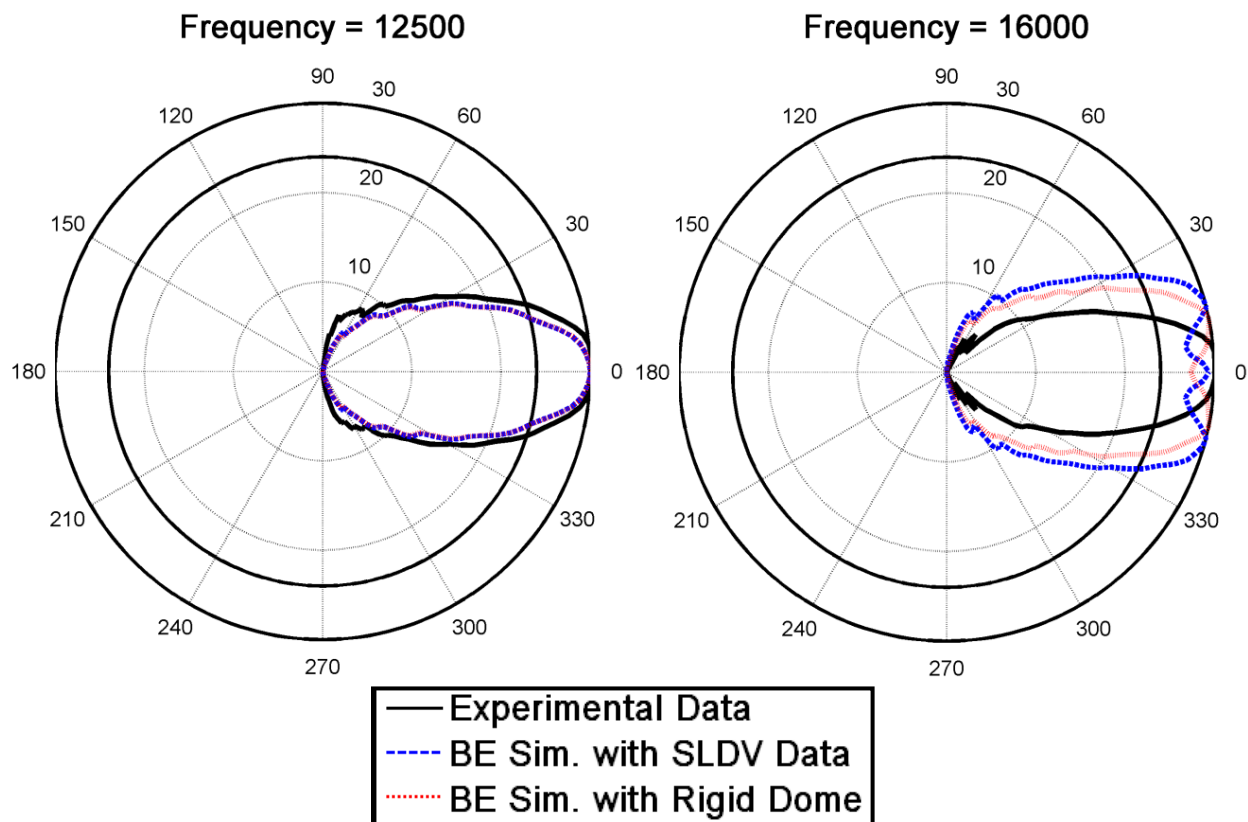


FIG. 5.7. Directivity results of Boundary-Element (BE) simulations run with, and without, the reconstructed Scanning Laser Doppler Vibrometer data. Both results are compared to experimental data of the physical system. The BE simulations are mounted to a $30^\circ \times 45^\circ$ horn.

These simulations serve as additional evidence that if modes are to be correctly extracted analytically, the radiation loading needs to be taken into account. To do this experimentally, would require an optically-precise, transparent back cap for the compression driver. SLDV

measurements have been taken through glass before, but measurements require the transparent cap to have no vibration. This may be difficult for the back cap due to its proximity to the acoustic source. It is also possible that the disagreement in directivity is due to errors in the approximate natural modes that were derived for the reconstruction. These modes are perhaps not similar enough to the actual modes (as seen in Fig. 5.4), and therefore do not reconstruct the SLDV data sufficiently well. The experimental data prove to be more useful for the simulation; however, the absence of the back cap seems to be the cause of the largest error. Thus, this is a possible area of future work as better modes can be derived and the experimental procedures for understanding modal breakup can be greatly improved.

5.3 Phase Plugs

The acoustical analysis of compression drivers in this chapter is focused on the phase plug. With each new pathway created in the phase plug, the potential for destructive interference and inefficient radiation is also created. The goal of the research was to discover what geometric model will produce the highest sound pressure levels without destroying the uniformity of the frequency response. The frequency responses trend upwards most likely because these simulations do not account for voice-coil inductance or modal breakup of the diaphragm.

The presentation style of the study is very similar to the presentation style for the study done on horns described in Ch. 4. First, an existing compression driver is simulated using the BEM to determine the validity of the simulation procedure. Next, the acoustical pathways of the existing compression driver are altered such that several different prototypes can be compared before being manufactured.

5.3.1 Modeling of Existing Compression Driver

Before simulating any new phase plug designs, an existing model is simulated to check the accuracy of the BEM. Since the compression driver is not usually used as a sound source by itself, simulations of each compression driver include a reference horn. Previous unpublished work recommended that the compression driver be mounted to an infinitely-long, “anechoically-terminated” pipe. Because the modal composition of the pressure wavefronts at a given cross section of the pipe cannot be analytically derived, the BEM has difficulty correctly prescribing an absorbing boundary condition at the nodal locations of the artificial infinite boundary (see [Sec. 2.2.1](#)). Additionally, due to the limitations of the available numerical package, the BEM was only used for steady-state analysis.

5.3.1.1 Model Specifications

In order to mesh both the horn *and the compression driver* fine enough for correct analysis within the entire audio bandwidth, the size of the mesh is necessarily twice the size of those in the previous studies of Ch. 4. Average models contained upwards of 60,000 elements, which significantly increased computation time. While previous models ran overnight, the computation time for these models was on the order of a few days. Computation time also depends on the available computing power. For this work a 64-bit computer with 48 GB of RAM, 16 processors at 2.4 GHz each, and a Windows Server 2008 operating system was used. Figure 5.8 shows the full mesh used to simulate an existing compression driver mounted to a reference horn (recall that, due to symmetry, only a quarter of the horn is necessary to model).

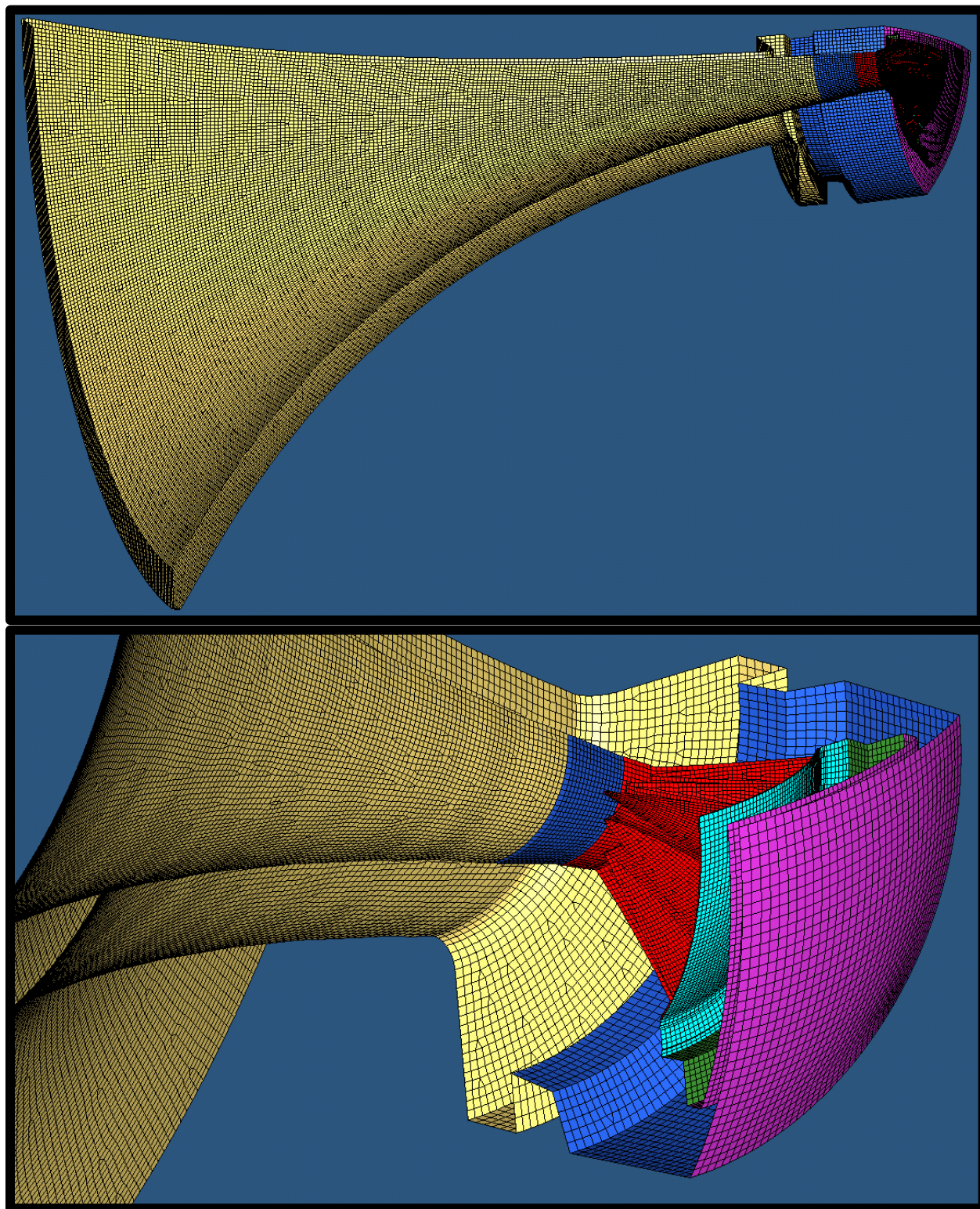


FIG. 5.8. Mesh used in simulation. A side view (top) and a back view (bottom) are shown.

Another change to the computational run time was increasing the number of evaluated frequencies to 33, where only 21 frequencies were simulated in the Ch. 4 computations. Because of parasitic resonances and increased variation at higher frequencies, an additional 12 frequencies were added to each computation. Thus, for these simulations the one-third octave center frequencies are evaluated from 200 Hz to 8 kHz, and then the one-twelfth octave center frequencies are evaluated between 8 kHz and 20 kHz. The increase in model size and frequencies rendered an approximate run time of about 4 to 5 days.

Another issue resulting from the addition of the compression driver boundaries in the BE simulations was poor convergence. Matrices can either be solved directly or iteratively. Coustyx, the BE package used in this work, uses an iterative solver (GMRES) to arrive at an approximate solution more quickly.⁶² However, the size of the mesh and possibly the proximity of the diaphragm boundary to the boundary of the phase plug (about 0.33 mm) causes the problem to converge slowly. Convergence is eventually obtained, but these simulations need approximately 2 to 8 times more iterations for accurate results than the previous Ch. 4 models.

As illustrated in Fig. 5.9, pressure and velocity values for many of these computations were computed at a distance of 3.048 meters (10 ft.) from the exit of the compression driver for the first 45° of the specified arc. The field points outside of the horn-loaded compression driver are considered to be in the far field ($kr \gg 1$) for frequencies above 200 Hz and allow general assessment of the system directivity and on-axis frequency response. Additional field points at the exit of the compression driver provide more information about the system frequency response before propagation into the far field.

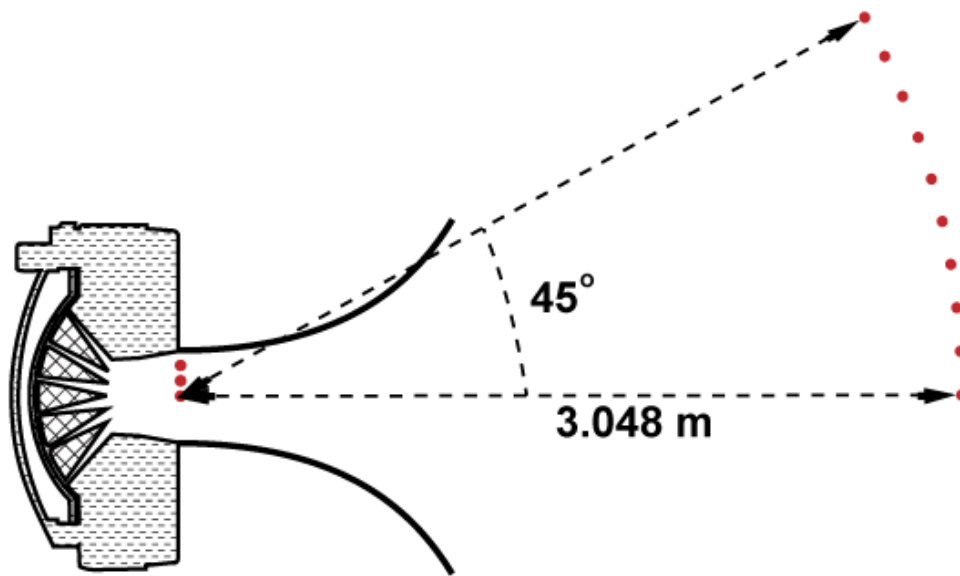


FIG. 5.9. Drawing indicating receiver locations (red dots) found in each numerical simulation where the compression driver is mounted to the reference horn. This drawing is not to scale.

For experimental verification, the existing compression driver was mounted to the $30^\circ \times 45^\circ$ and $120^\circ \times 60^\circ$ horns and the on-axis frequency response for each system was obtained at 3.048 meters (10 ft.) from the entrance of the horn. Experimental measurements were obtained previously by others in an anechoic chamber at approximately the same distance. Figure 5.10 compares simulation and experimental results for the $30^\circ \times 45^\circ$ horn. Figure 5.11 compares results for the $120^\circ \times 60^\circ$ horn. The reference pressure for both the experimental and simulated data is $20 \mu\text{Pa}$, and the excitation velocity of the simulated diaphragm mounted to both horns was approximately 1.66 m/s.

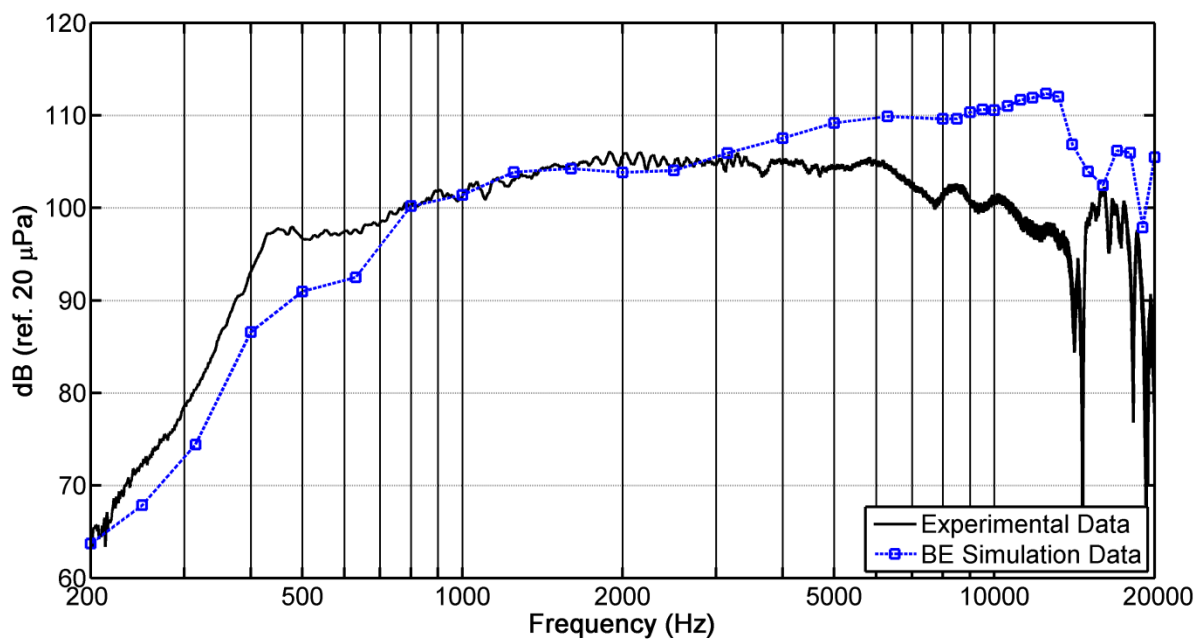


FIG. 5.10. Frequency response results for simulation and experiment of an ND6 compression driver on a 45° x 30° horn. Measurement is on-axis, 3.048 m from the entrance of the horn.

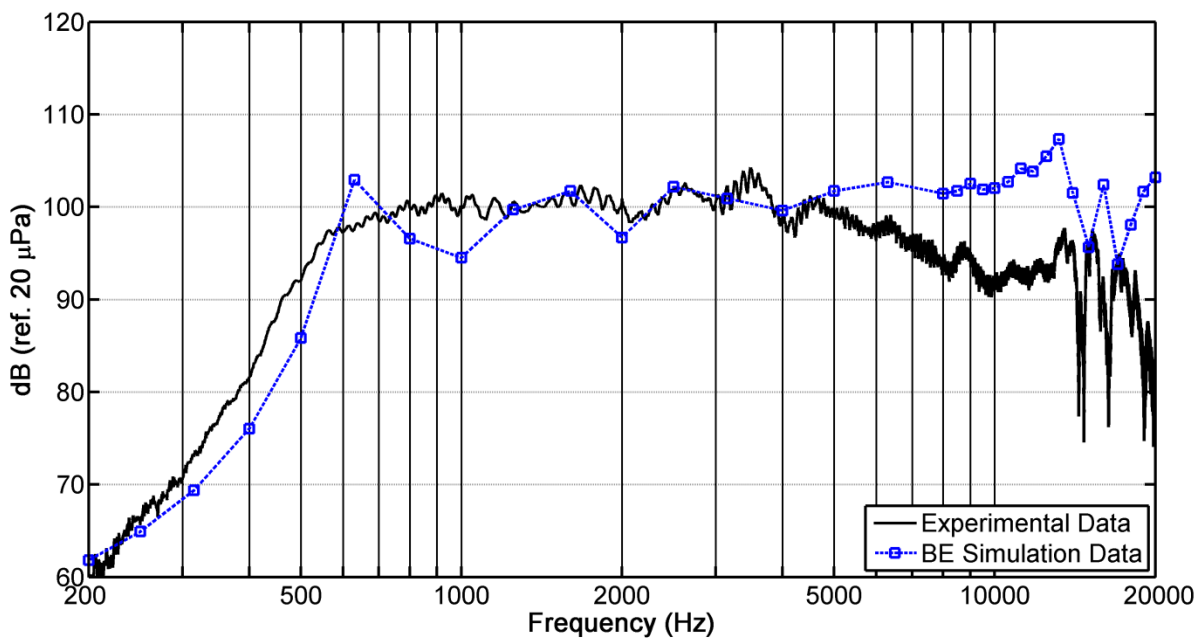


FIG. 5.11. Frequency response for simulated and experimental results of an ND6 compression driver on a 120° x 60° horn. Measurement is on-axis, 3.048 m from the entrance of the horn.

As seen in these figures, fairly significant disagreement exists between the results of the numerical simulations and experimental measurements, particularly at higher frequencies. For the simulations, the diaphragm of the compression driver is prescribed a constant velocity over frequency. However, this boundary condition is not physical, as discussed in [Sec. 5.2](#) since the diaphragm vibrates in higher-order modal patterns. The diaphragm undergoes a mass-spring mechanical resonance (usually around 400 to 700 Hz), which increases its excursion and subsequent radiation. Incorporation of the electrical domain of the compression driver will also provide some differences. Since the impedance of the voice coil increases with frequency, less current is drawn at higher frequencies. With less current, excursion and subsequent radiation decreases. Other electro-mechano-acoustical effects also may affect its vibration. Figures 5.10 and 5.11 illustrate these differences as the simulations tend to produce less radiation at lower frequencies without the resonance of the diaphragm, and more radiation for higher frequencies due to a lack of modal break-up of the diaphragm and electrical inductance.

The peak in Fig. 5.11 at 630 Hz does not correlate with the preceding analysis. This resonance appears to be associated with the fundamental frequency of a closed-open pipe of about 12 to 15 cm in length. The throat of the $120^\circ \times 60^\circ$ horn measured in Fig. 5.11 flares in one direction, but maintains a pipe-like geometry in the other. The diaphragm acts as the closed end, the cross section of the pipe-like geometry is the pipe, and the open end is created when the horn begins to rapidly flare. When the system undergoes resonance, radiation increases. The acoustical resonance is more pronounced in BE simulation, possibly because of the lack of damping within the model. Another reason that this resonance does not appear in experiment may be due to the non-constant velocity boundary condition of the diaphragm. In simulation, this boundary does not alter its velocity component and is not affected by increased radiation.

Incorporation of the electrical inductance into the model would improve agreement between the simulated and measured data. With this incorporation, the diaphragm velocity would be specified as a function of frequency. Incorporation of this parameter is difficult as both the mechanical and acoustical domains couple with the electrical domain. Thus, the mechanical and acoustical loading of the compression-driver model would need to be known to incorporate these loadings into an electro-mechano-acoustical equivalent circuit. An accurate equivalent circuit would allow extraction of a velocity correction due to the voice coil impedance. The diaphragm velocity might be extracted experimentally, but this is beyond the scope of this work.

Regardless of the discrepancies seen in Figs. 5.10 and 5.11, general trend of increasing radiation with frequency is followed in both simulations of the existing compression driver. This provides some confidence in the BEM and since none of the prototypes include the electrical or mechanical domains, these simulations provide a meaningful first look at the acoustical performance of various prototype designs.

5.3.1.2 Parasitic Resonances

Before the BE simulations were able to be verified, a gap (for the voice-coil) in the geometry of the compression driver was eliminated. This gap provided an additional cavity where air could compress, decreasing overall radiation. This phenomenon has been termed a parasitic resonance.⁵⁰ These interior-cavity resonances are not apparent in physical measurements if the majority of the gap is filled. For the experimental results presented, these gaps have been filled with a plastic ring. The voice coil also takes up space in this cavity. There is also a finite amount of viscous and/or thermal damping in this cavity that is not accounted for in the model. Since this boundary is mostly filled physically, elimination of it in the model is a

valid assumption. Although these parasitic resonances will not appear in the frequency response, their resonances fall within the audio bandwidth of interest and thus merit some attention.

Figure 5.12 shows the original mesh used to calculate the frequency response of the existing compression driver containing parasitic resonances. The bottle-shaped cross-sectional gap (in red) causes a significant acoustical resonance (as confirmed by a simple Helmholtz resonance calculation). Since these gaps were filled for the compression drivers tested experimentally, these gaps are removed from the models to better simulate the filling of the gaps. Once this gap is removed from the model, the resonance is eliminated and far-field radiation is more well behaved. The magnitude of the dip in the simulated frequency response is due, in part, to the fact that the cavity under resonance is undamped, since damping is not included in the BE simulations. Both the bottle-shaped gap and the straight gap below the surround of the diaphragm are removed in the final simulation geometry. Thus, a fictitious boundary is placed at the beginning of the spherical curvature of the diaphragm and the edge of the phase plug. Figure 5.12 shows the different geometries which produced the frequency response data with and without the boundary in the simulation.

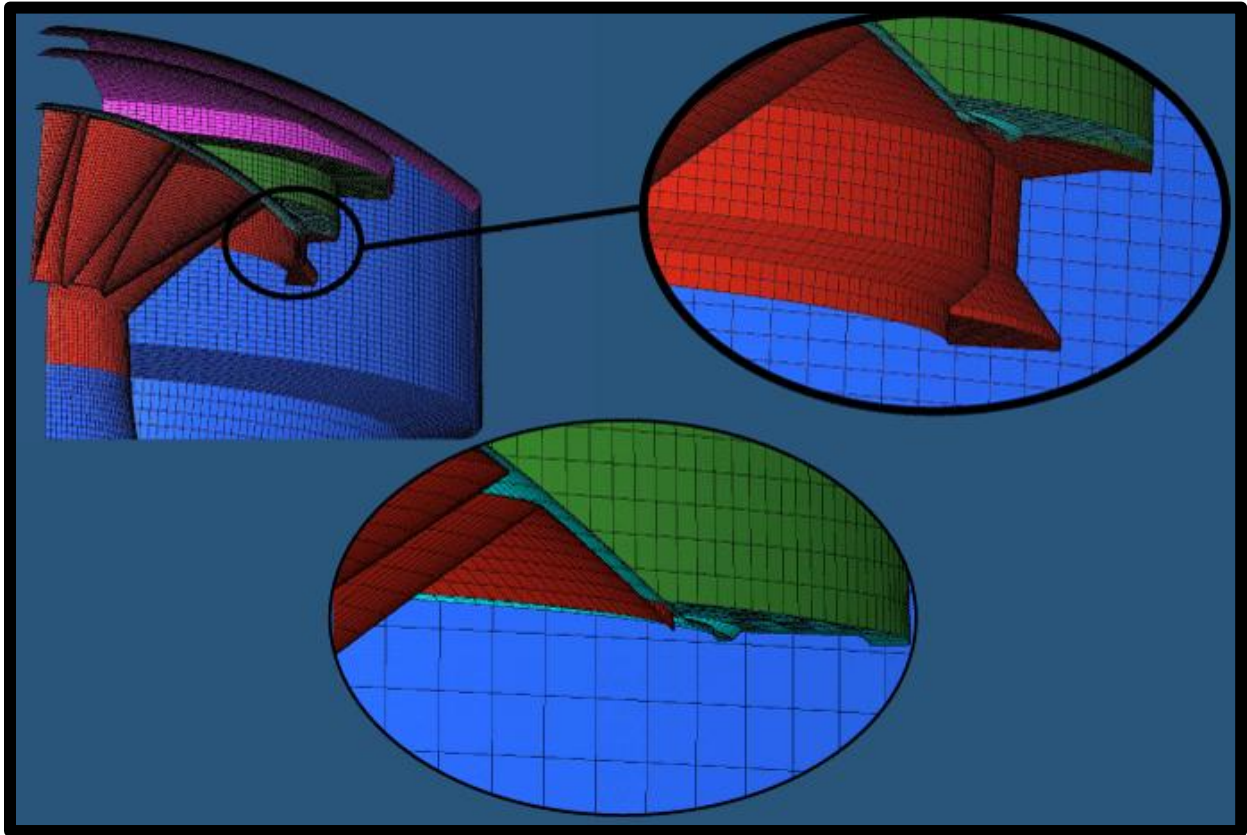


FIG. 5.12. Illustration of the gap in the BE mesh (top) that causes a parasitic resonance, and the reduced boundary (bottom) used to eliminate it.

Depending on the size and shape of the cavity, the resonance can occur anywhere within a broad range of frequencies. For the existing compression-driver model, resonance occurs around 2.5 kHz. Once the gap is removed, the resonance is eliminated. Other models show similar resonances as high as 5 kHz (model 5 of Sec. 5.3.2). As expected, when the gap is removed, the resonance (along with other resonances at higher frequencies) disappears.

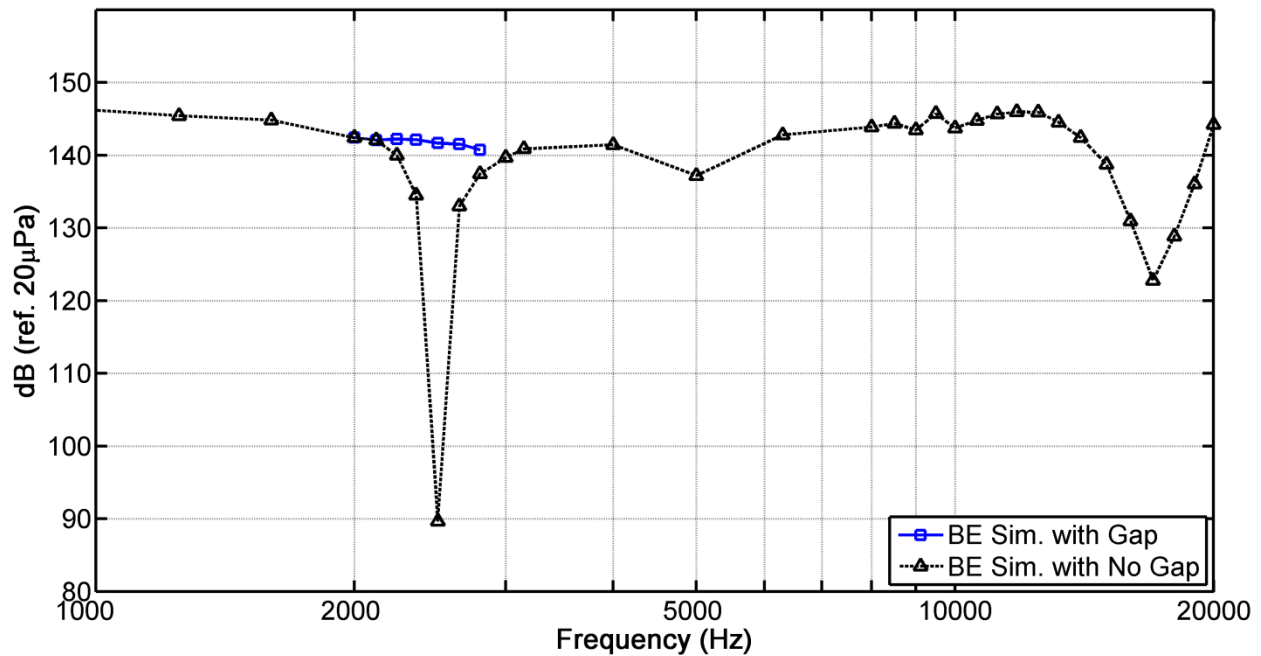


FIG. 5.13. Frequency response comparison at compression driver exit of an existing model with and without the boundary causing a parasitic resonance at 2.5 kHz.

Care must be taken when analyzing this plot. Many of the dips seen in a discrete frequency response may be more pronounced if alternate discrete frequency values are chosen, which is why only an approximate value is known for the parasitic resonance in Fig. 5.13. Although a continuous spectrum would be more insightful (if it were possible to simulate numerically), these discrete frequency-response measurements do help to understand the significant acoustical effects of the compression chamber, phase plug, and throat of each compression-driver model.

5.3.2 Phase Plug Study

Since the BEM provides reasonable agreement throughout most of the audio bandwidth for on-axis pressure radiation, the phase plug can be altered several different ways in an attempt to better understand where the current phase-plug design might be improved. Seven different phase-plug models were studied to determine which phase plug characteristics may render better next-generation products. The boundaries of the phase plug channels and the lengths of the phase plug exits are the altered features in these prototypes. All seven compression drivers are loaded to a cylindrically-symmetric reference horn for their BE simulations. The reference horn is 0.3048 meters (12 inches) long and flares exponentially. This horn was used instead of the constant directivity horns (horns used in previous sections) to provide an axisymmetric model, which reduces computation time.

For this study, each model is referred to by a number. Table 5.1 describes the basic geometric differences for each. Model 1 is the existing compression driver that was used in [Sec. 5.3.1](#) to validate the BE simulation and is also the standard with which other prototypes are compared. None of the models have the boundary surrounding the voice-coil so that parasitic resonances were eliminated. Each model diaphragm is given the same velocity boundary condition for each simulation. The results were not normalized, so any acoustical differences in overall radiated pressure are observable. Figures 5.14 through 5.16 allow observation of the differences in the frequency responses of the seven models.

TABLE 5.1. Description of the seven compression driver models used in the study of phase plug designs.

Model #	Model Description
1	Standard driver.
2	Increased spacing between standard driver diaphragm and phase plug.
3	Shortened driver with quicker channel expansion. Straight phase plug paths.
4	One wavy phase plug channel (outside channel) and two straight channels.
5	Two wavy phase plug channels and one straight channel (inside channel).
6	Standard driver with a shorter distance between phase plug exit and compression driver exit.
7	Standard driver with a longer distance between phase plug exit and compression driver exit.

Although most of the changes with each of the prototypes are in the phase plug, this is not the only component that was changed in these models. The compression chamber and compression driver throat length were changed as well. These models will help to better understand the effects on radiation performance for each component varied. Much of this is addressed as each prototype is compared to the existing compression-driver model. It should also be noted that while these frequency response measurements contain many points at high frequencies, large gaps still exist between each discrete frequency. Many features of these models may be hidden between the chosen frequencies.

Figure 5.14 shows the on-axis pressure radiation in dB for models 1, 2, and 3. The most notable difference is that model 2 has significantly lower radiation output above 8 kHz. It may be an undesirable design since the BE simulation does not account for the electrical inductance or modal breakup of the diaphragm. Therefore, the frequency response of a physical model 2 likely decreases rapidly at high frequencies. Model 3 compares well with the existing compression driver; however, its frequency response seems less smooth, with possible resonances that may

not be detected with the discrete frequencies chosen. Lower radiation from model 3 is observed in some of the lower and mid frequencies.

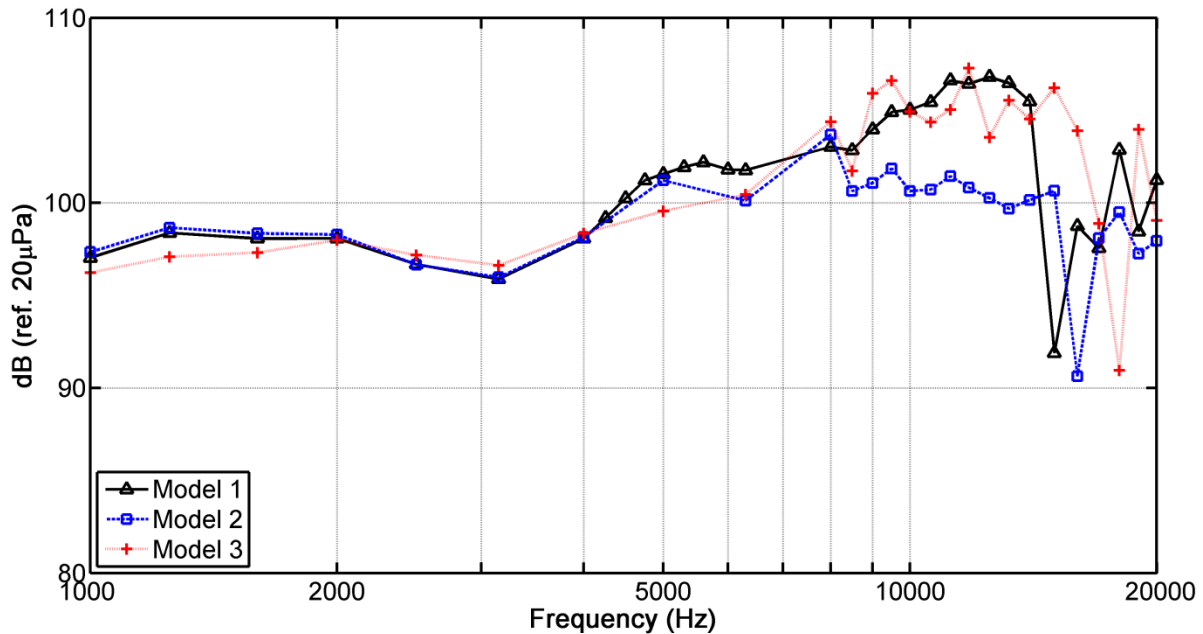


FIG. 5.14. Comparison of on-axis frequency response radiation for models 1, 2, and 3.

Figure 5.15 compares on-axis pressure radiation in dB for models 1, 4, and 5. Models 4 and 5 both have wavy-shaped phase plug channels, but the characteristics of these waves are different. Two of the three channels of the model 4 phase plug are wavy, while only the outside channel is wavy for model 5. Apart from a dip in the response at 11.8 kHz, model 4 outperforms model 1 in level at several frequencies. Once again, these results may change when electrical and mechanical domains are included in the simulations. However, these results show a general increase in on-axis pressure radiation for higher frequencies.

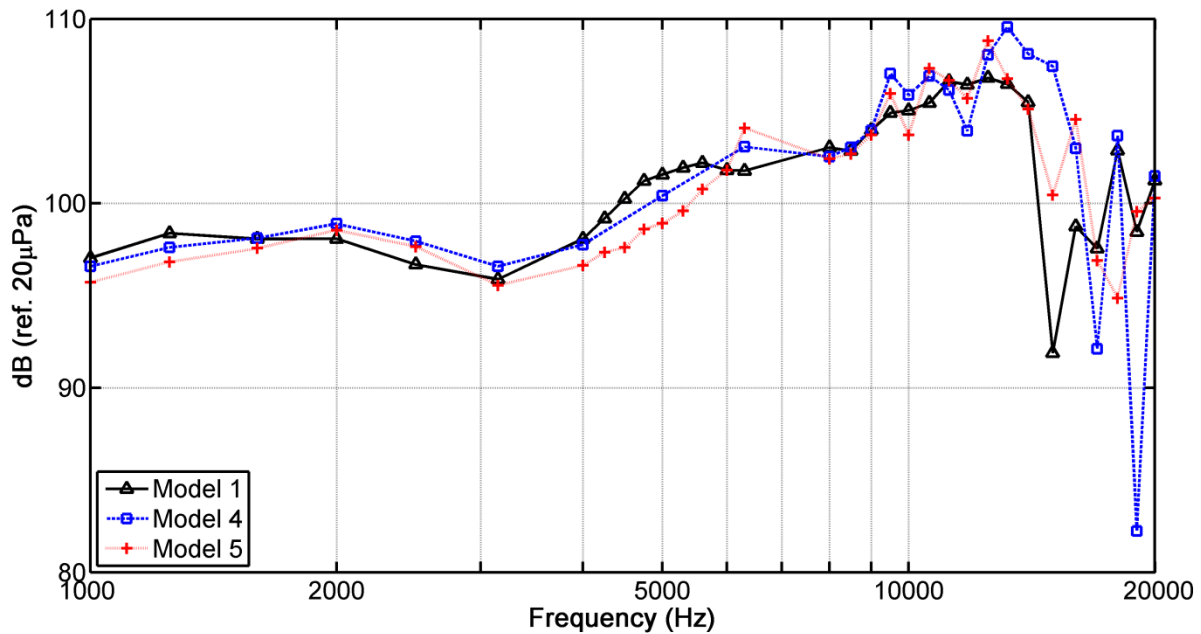


FIG. 5.15. Comparison of on-axis frequency response radiation for models 1, 4, and 5.

Figure 5.16 compares on-axis pressure radiation in dB for models 1, 6, and 7. The frequency responses of models 6 and 7 are not much different than that of the existing compression driver, model 1. The low and mid frequencies reproduced by model 6 outperform those reproduced by model 7, but only by about 1 dB. Although most likely not the major contributor, the diaphragm is farther away from the measurement points since the origin of measurement is always at the exit of the compression driver. Additionally, model 7 allows for slightly more evanescence of higher-order modes at lower frequencies. This may also have an effect on the overall on-axis, far-field radiation for each prototype.

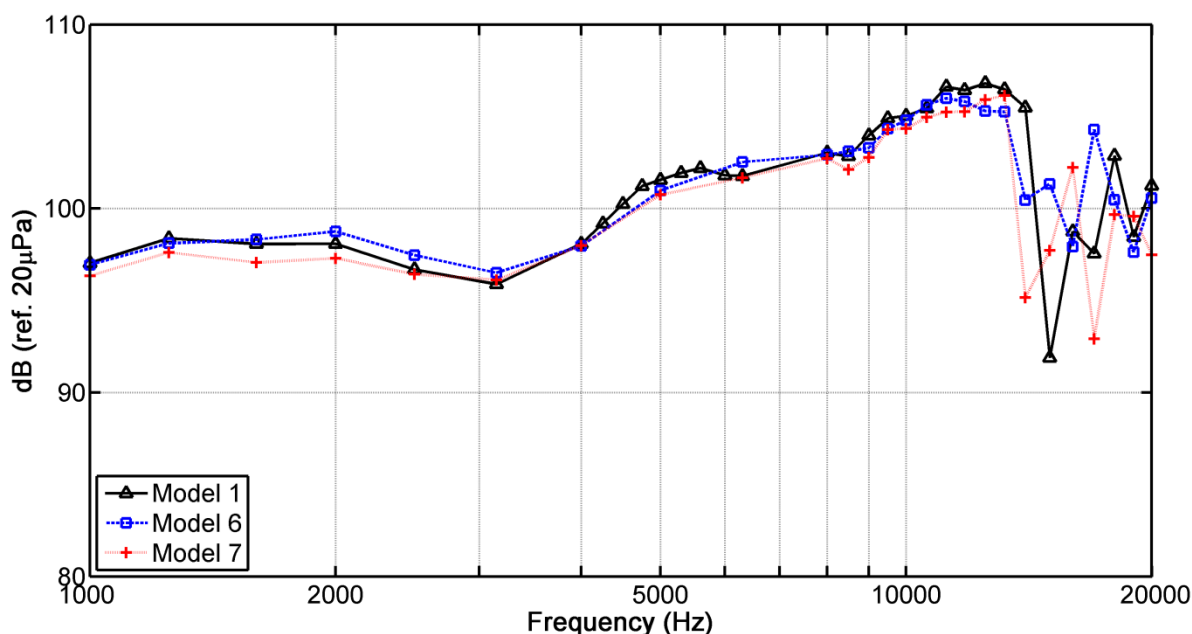


FIG. 5.15. Comparison of on-axis frequency response radiation for Model 1, 6, and 7.

5.4 Conclusions

Mechanical vibrations of the diaphragm were quantified in terms of analytically-derived natural modes of a spherical cap. However, these modes are only moderately capable of reconstructing the measured dome vibrations. In order to acquire laser vibrometer scans of the diaphragm, the back cap of the compression driver was cut away. This changed the acoustical loading on the diaphragm significantly. Altered acoustic loading on the front of the dome was observed to cause differences in vibration. The difference in acoustic loading was also made manifest in BE simulations that used the reconstructed modal vibration patterns. In order to experimentally obtain modal patterns of the diaphragm, to subsequently use as a more accurate model of diaphragm motion in simulations, one must maintain the proper acoustic loading.

Acoustical analysis of the horn-loaded compression driver included BE simulations of several different compression driver models. Generally speaking, no prototype outperformed the existing model (model 1). However, the results of the simulations should be analyzed carefully. Many of the high-frequency resonances appear reduced or eliminated from certain models, while they are very obvious with others. It is possible that these resonances exist in all of the models, but lie in between the frequency data points displayed. If a resonance lies between two discrete simulation frequencies, it may not be apparent in the frequency response. Although many of these resonances would not be as extreme if damping were included in the model, care must be taken when comparing the results, since the BE simulations only analyzed the acoustical domain. A full picture of a horn-loaded compression driver's frequency response would require coupling of the electrical and mechanical domains.

Future work in this area may involve a more numerically rigorous approach to the problem of incorporating diaphragm modes into the modeling. While the analytically-derived natural modes of a spherical cap may be improved upon for the model used in this chapter, the method of reconstruction described in the chapter required the back cap to be removed from the compression driver—changing the vibrational modes of the diaphragm. An alternative may be to construct a transparent back cap, which must remain rigid, to allow laser imaging while maintaining the acoustic loading. A numerical alternative would be to use a finite element model of the entire compression driver, since it may be better able to simulate the correct modal vibrations of the diaphragm.

Chapter 6

Conclusions

6.1 Conclusions

Numerical simulations for a horn-loaded compression driver and an infinitely baffled finite-length pipe have been presented and analyzed. For the compression driver, simulations were used as a comparative tool between various computer-drafted models. Horns were simulated individually and then with the compression driver as a composite systems. The majority of these simulations were done with the boundary-element method (BEM). For the pipe, the simulations were computed using the finite-difference method (FDM). Because such a variety topics were covered in the thesis, summaries and conclusions are given for Chapters 3, 4, and 5 individually.

In Chapter 3, numerical simulations of transient wave propagation and subsequent radiation for a constant cross-section pipe were presented and analyzed. As stated previously,

these simulations used the FDM, which helped produce better understanding of transient radiation for pulse-like signals from a finite-length pipe. This analysis also served as a basis for understanding transient radiation from other geometries like horns. Independent natural modes of the pipe were excited individually and compared with one another. The plane-wave mode was noted to have maximum radiation on axis, where higher-order modes have their maximum radiation off axis. When pipe modes were excited individually, a fair amount of coupling of the pipe modes with the half-space modes was observed and should not be ignored in future analytical models. This work also gives insight into some of the differences between transient and steady-state radiation, and lays the groundwork for possible analysis of transient radiation from horn-loaded compression drivers. However, convergence issues of the FDM with non-analytically defined geometries would need to be ironed out.

In Chapter 4, the numerical simulations and experimental results for two existing horns, in terms of directivity and frequency response, were compared. The horns were first modeled to ensure better understand the limitations of the boundary-element (BE) simulations. A study was subsequently performed in which the curvature of the input wavefront was varied. Moderate differences in the overall frequency responses were observed as the amount of energy imparted to the higher-order modes changed, depending on the curvature of the excitation boundary. In one case, the simulated planar wavefront did not produce as much radiation as the simulated outward-curvature wavefront, possibly challenging the long-held belief that a planar wavefront is most desirable at the entrance of the horn. No differences in the horn directivity patterns were observed until above 10 kHz. The horn geometry governs the propagation of low-frequency wavefronts. It was shown that the horn geometry causes evanescence of higher-order modes below 10 kHz, producing similar directivity results for many different excitation sources. Above

10 kHz, significant contributions from higher-order modes (mostly the first higher-order mode) affected the far-field pressure radiation such that the directivity no longer agreed with experimental results. Any estimation of the combination of multiple modes propagating through the horn and the subsequent radiation into the far-field needs to be very precise.

In Chapter 5, the compression driver was analyzed. Two components of the compression driver were looked at in depth: (1) the diaphragm and (2) the phase plug. In the analysis of the diaphragm, approximate natural modes of a spherical cap were derived and fit to experimental laser vibrometer scans of the diaphragm. The scans were performed by cutting off the back of the compression driver—to provide the necessary visible access to the surface of the dome. Several different scans were performed while the front acoustic loading was changed in several different ways. The acoustic loading significantly affected the coefficients used to determine the appropriate linear combination of the natural modes comprising the vibration of the diaphragm. This was verified with more scans. A BE simulation used the reconstructed profile for the vibration of the diaphragm but it resulted in poor agreement between the simulated and experimental directivities. Possible reasons for this disagreement were given and more work will need to be done to accurately use this type of technique.

In the analysis of the phase plug, seven different models were numerically constructed and tested via BE simulations. One of the seven was an existing compression driver. Thus, a comparative analysis with this model was performed to better understand how the other six designs differed from the existing design. Problems with parasitic resonances were discovered and overcome to give more accurate frequency responses for each model. These models took very long to run and seemed to be pushing the limits of available computational power. None of the models seemed to clearly perform better than the others. The existing design seemed to be

the smoothest, though a higher density of frequency points may need to be run to confirm this result.

6.2 Future Work

One of the most exciting areas of future work is that of extending the transient analysis to horn-loaded compression drivers. Since many signals reproduced by these systems are transient in nature, a better understanding of the transient effects of horn radiation is necessary and may provide meaningful breakthroughs in fundamental horn design. The methods were developed in this thesis with the FDM, but stability is difficult to achieve when signals are short transients (as many higher frequencies are excited). Further research may be able to perfect the FDM to better handle transient signal stability in three-dimensional models. The FEM may be a viable option as the stability problems can be avoided due to more flexible meshing requirements; the drawback to the FEM is that numerical inversions are required for each temporal step, which would greatly increase the necessary computation time.

While individual studies of horn and compression driver components could carry on indefinitely, it is in the coupling of these problems that more meaningful analysis will likely occur. The numerical solution most readily accessible for solving multi-domain problems is the FEM. As discussed briefly in Ch. 2, this method is very popular and has been commercialized by several companies. Irregular geometries are handled easily and meshing does not have the analytical complications associated as with the FDM. The FEM can also solve multi-domain models. It may be that coupling numerical solvers, such as FEM and BEM solvers, will allow further progress in this area of research. Modern technology will only continue to improve,

making the transition to numerical studies an increasingly attractive and beneficial method for product development.

The question of electrical, mechanical, and acoustical nonlinearity present in the physical model will eventually need to be addressed. Analyzing these systems with linear numerical methods may overlook some of the signal distortion that is present physically. Figures 4.14 through 4.19 show that peak pressures of between 200-500 Pa (140-148 dB sound pressure levels) are necessary in horn throats to produce typical radiation output levels from the horn. With systems producing very high sound pressure levels, nonlinear acoustical effects can easily occur and is something designers must be aware of. Numerical models will eventually need to investigate possible nonlinear effects as these problems will not be detected using current linear numerical techniques. For example, one may incorrectly ascribe some experimentally measured distortion to other sources such as coil rub or voice coil excursion outside of the linear range of the magnetic field when it may be the case that the operator drove the compression driver at amplitudes such that acoustic nonlinearity (or distortion) was generated within the horn and/or in the radiated field. The FDM may in fact prove to be a useful method for handling this problem due to its ability to handle complex nonlinear wave equations.

Bibliography

- ¹ D. J. Chappell, G. Geaves, D. J. Henwood, P. J. Harris, and R. Chakrabarti, “Modeling the Transient Acoustic Field Radiated by a Loudspeaker,” *J. Audio Eng. Soc.*, **56**, 956-971 (2008).
- ² R. D. Ciskowski and C. A. Brebbia, *Boundary Element Methods in Acoustics* (Computational Mechanics Publications, Boston, 1991).
- ³ G. Beer, *Programming the Boundary Element Method: An Introduction for Engineers* (John Wiley & Sons, England, 2001).
- ⁴ L. C. Wrobel, *The Boundary Element Method: Applications in Thermo-Fluids and Acoustics* (John Wiley & Sons, England, 2001).
- ⁵ F. Magoules, *Computational Methods for Acoustics Problems* (Saxe-Coburg Publications, Scotland, 2008).
- ⁶ T. W. Wu, *Boundary Element Acoustics: Fundamentals and Computer Codes* (WIT Press, Boston, 2000).
- ⁷ P. K. Kythe, *An Introduction to Boundary Element Methods* (CRC Press, Florida, 1995).

- ⁸ L. G. Ireland, “Numerical Modeling of Multi-Mode Active Control of Turbofan Tonal Noise Using a Boundary Element Method,” Ph.D. dissertation, Brigham Young University, 2000.
- ⁹ A. Pierce, *Acoustics* (Acoust. Soc. of America, Melville, 1989).
- ¹⁰ G. B. Arfken and H. J. Weber, *Mathematical Methods for Physicists 6th Ed.* (Elsevier, California, 2005).
- ¹¹ R. J. LeVeque, *Finite Difference Methods for Ordinary and Partial Differential Equations* (SIAM, Philadelphia, 2007).
- ¹² F. Fahy and J. Walker, *Advanced Applications in Acoustics, Noise and Vibration* (Routledge, New York, 2004).
- ¹³ S. Marburg and B. Nolte, *Computational Acoustics of Noise Propagation in Fluids: Finite and Boundary Element Methods* (Springer, Berlin Heidelberg, 2008).
- ¹⁴ Lord Rayleigh, *The Theory of Sound, vol. II* (Dover Publications, New York, 1945), pg. 72-74.
- ¹⁵ J. D. Pearson, “The transient motion of sound waves in tubes,” *Quart. J. Mech. and Appl. Math.*, **6**, 313 (1953).
- ¹⁶ J. M. Proud, P. Tamarkin, and E. T. Kornhauser, “Propagation of sound pulses in a dispersive medium,” *J. Acoust. Soc. Am.*, **28**(1), 80-85 (1956).

- ¹⁷ K. J. Baumeister, "Finite Difference Solutions of Transient acoustic Mode Propagation in Ducts," *J. of Eng. for Industry*, **104**, 113-120 (1982).
- ¹⁸ H. Levine and J. Schwinger, "On the radiation of sound from an unflanged circular pipe," *Physical Review*, **73**(4), 383-406(1948).
- ¹⁹ Y. Nomura *et al*, "Radiation from a flanged circular pipe," *J. Phys. Soc. Jap.*, **15**(3), 510-517 (1960).
- ²⁰ N. Amir and H. Matzner, "Acoustics of a flanged cylindrical pipe using singular basis functions," *J. Acoust. Soc. Am.*, **107**(2), 714-724 (2000).
- ²¹ Y. Tsubakishita, H. Hamana, and T. Yoshikawa, "Finite Difference Solutions to Sound Radiation from Cylindrical Ducts," *JSME International*, **38**(1), 60-65 (1995).
- ²² K. J. Baumeister, "Time-Dependent Wave Envelope Finite Difference Analysis of Sound Propagation," *AIAA Journal*, **24**(1), 32-38 (1986).
- ²³ A. A. Osipov and I. A. Shirkovskii, "Finite-element calculation of sound fields radiated from the open end of an axisymmetric duct," *Sov. Phys. Acoust.* **30**(4), 307-310 (1984).
- ²⁴ J. P. Dalmont, C. J. Nederveen, and N. Joly, "Radiation Impedance of Tubes with Different Flanges: Numerical and Experimental Investigations," *J. of Sound and Vib.*, **244**(3), 505-534 (2001).
- ²⁵ K. J. Baumeister, "Numerical Techniques in Linear Duct Acoustics—A Status Report," *J. of Eng. for Industry*, **103**, 270-281 (1981).

- ²⁶ D. Noreland, "A Numerical Method for Acoustic Waves in Horns," *Acta Acust.*, **88** 576-586 (2002).
- ²⁷ S. Davis, "Low-dispersion finite difference methods for acoustic waves in a pipe," *J. Acoust. Soc. Am.* **90**(5), 2775-2781 (1991).
- ²⁸ P. Stepanishen and R. A. Tougas, "Transient acoustic pressure radiated from a finite duct," *J. Acoust. Soc. Am.*, **93**(6), 3074-3084 (1993).
- ²⁹ D. Givoli, "Non-reflecting boundary conditions: a review," *J. Comp. Phys.*, **94**, 1-29 (1991).
- ³⁰ D. Givoli, *Numerical Methods for Problems in Infinite Domains* (Elsevier Science Publishers, Amsterdam, 1992).
- ³¹ S. Acosta and V. Villamizar, "Coupling of Dirichlet-to-Neumann Boundary Condition and Finite Difference Methods in Curvilinear Coordinates for Multiple Scattering," *J. Comp. Phys.*, **229**, 5498-5517 (2010).
- ³² V. Villamizar and O. Rojas, "Time-Dependent Numerical Method with Boundary-Conforming Curvilinear Coordinates Applied to Wave Interactions with Prototypical Antennas," *J. Comp. Phys.*, **177**, 1-36 (2002).
- ³³ V. Villamizar and S. Acosta, "Elliptic grids with nearly uniform cell area and line spacing," *Electronic Trans. on Num. Analysis*, **34**, 59-75 (2009).

- ³⁴ V. Villamizar and M. Weber, "Boundary-Conforming Coordinates with Grid Line Control for Acoustic Scattering from Complexly Shaped Obstacles," *J. Num. Meth. for Partial Diff. Eqs.*, **23**(6), 1445-1467 (2007).
- ³⁵ S. Acosta and V. Villamizar, "Finite Difference on Grids with Nearly Uniform Cell Area and Line Spacing for the Wave Equation on Complex Domains," *J. Comp. and Appl. Math.*, **234**(6), 319-325 (2010).
- ³⁶ V. Villamizar and S. Acosta, "Generation of smooth grids with line control for scattering from multiple obstacles," *Math. and Comp. in Sim.*, **79**, 2506-2520 (2009).
- ³⁷ D. Blackstock, *Fundamentals of Physical Acoustics* (John Wiley & Sons, New York, 2000).
- ³⁸ L. Kinsler and A. Frey, *Fundamentals of Acoustics 4th Ed.* (John Wiley & Sons, New York, 2000).
- ³⁹ A. G. Webster, "Acoustical Impedance, and the Theory of Horns and of the Phonograph," *Proc. Nat. Acad. Sci.*, **5**, 275-282 (1919).
- ⁴⁰ E. Eisner, "Complete Solutions of the 'Webster' Horn Equation," *J. Acoust. Soc. Am.*, **41**, 1126-1145 (1967).
- ⁴¹ J. E. Freehafer, "The Acoustical Impedance of an Infinite Hyperbolic Horn," *J. Acoust. Soc. Am.*, **11**, 467-476 (1940).

- ⁴² P. M. Morse and H. Feshbach, *Methods of Theoretical Physics* (McGraw Hill, New York, 1953).
- ⁴³ G. R. Putland, "Every One-Parameter Acoustic Field Obeys Webster's Horn Equation," *J. Audio Eng. Soc.*, **41**, pp. 435-451 (1993).
- ⁴⁴ E. Geddes, "Acoustic Waveguide Theory," *J. Audio Eng. Soc.*, **37**, 554-569 (1989).
- ⁴⁵ J. S. McLean, J. T. Post, and E. L. Hixson, "A theoretical and Experimental Investigation of the Throat Impedance Characteristics of Constant Directivity Horns," *J. Acoust. Soc. Am.*, **92**, 2509-2520 (1992).
- ⁴⁶ T. Helie and X. Rodet, "Radiation of a Pulsating Portion of a Sphere: Application to Horn Radiation," *Acta Acustica united with Acustica*, **89**, 565-577 (2003).
- ⁴⁷ M. Di Cola, D. Doldi, and D. Saronni, "Horn's Directivity Related to the Pressure Distribution at their Mouth: part 2," AES Convention Paper, 110th Conv. (2001).
- ⁴⁸ A. Gloukhov, "A Method of Loudspeaker Directivity Prediction Based on Huygens-Fresnel Principle," AES Convention Paper, 115th Conv. (2003).
- ⁴⁹ M. Ureda, "Directivity Phase Response of Horns," AES Convention Paper, 94th Conv. (1993).
- ⁵⁰ E. Geddes, "Computer Simulation of Horn-Loaded Compression Drivers," *J. Audio Eng. Soc.*, **35**, 556-566 (1987).

- ⁵¹ T. F. Johansen, "On the Directivity of Horn Loudspeakers," *J. Audio Eng. Soc.*, **42**, 1008-1019 (1994).
- ⁵² A. C. Hladky-Hennion, "Finite Element Analysis of the Propagation of Acoustic Waves in Waveguides," *J. Sound and Vib.*, **194**, 119-136 (1996).
- ⁵³ D. J. Henwood, "The Boundary-Element Method and Horn Design," *J. Audio Eng. Soc.*, **41**, 485-496 (1993).
- ⁵⁴ B. Locanthi, "Application of Electric Circuit Analogies to Loudspeaker Design Problems," *J. Audio. Eng. Soc.*, **19**, 778-785 (1971).
- ⁵⁵ D. B. Keele, "What's so sacred about exponential horns?" presented at the 51st convention of the AES, Los Angeles, preprint 1038 (1975).
- ⁵⁶ H. Suzuki, "Sound Radiation from a Concave or a Convex Dome in a Semi-Infinite Tube," *Jo. Audio Eng. Soc.*, **33**, 956-962 (1985).
- ⁵⁷ H. Suzuki and J. Tichy, "Radiation and Diffraction Effects by Convex and Concave Domes," *J. Audio Eng. Soc.*, **29**(12), 873-881 (1981).
- ⁵⁸ D. A. Barlow, "The Resonances of Loudspeaker Diaphragms," *J. Audio Eng. Soc.*, **29**, 699-704 (1981).
- ⁵⁹ K. Takada and A. Matsuda, "On the Vibrational Analysis of Dome-Type Loudspeakers by the Finite Element Method," presented at the 60th AES Convention, Los Angeles, preprint 1346 (1978).

- ⁶⁰ T. Shindo, T. Yoshioka, and K. Fukuyama, "Calculation of Sound Radiation from an Unbaffled, Rectangular-Cross-Section Horn Loudspeaker Using Combined Analytical and Boundary-Element Methods," *J. Audio Eng. Soc.*, **38**, 340-349 (1990).
- ⁶¹ E. Geddes, J. Porter, and Y. Tang, "A Boundary-Element Approach to Finite-Element Radiation Problems," *J. Audio Eng. Soc.*, **35**(4), 211-229 (1987).
- ⁶² D. Bie, "Vibration Resonances of a Titanium Loudspeaker Diaphragm," presented at the 104th AES Convention, Amsterdam, 4642 (1998).
- ⁶³ S. Kinoshita and B. Locanthi, "The Influence of Parasitic Resonances on Compression Driver Loudspeaker Performance," presented at the 61st AES Convention, New York, preprint 1422 (1978).
- ⁶⁴ G. K. Behler and M. Makaraski, "Two-Port Representation of the Connection between Horn Driver and Horn," *J. Audio Eng. Soc.*, **51**, 883-897 (2003).
- ⁶⁵ B. H. Smith, "An Investigation of the Air Chamber of Horn Type Loudspeakers," *J. Acoust. Soc. Am.*, **25**, 305-312 (1952).
- ⁶⁶ E. Wente and A. Thuras, "A High-Efficiency Receiver for a Horn-Type Loudspeaker of Large Power Capacity (Reprint)," *J. Audio Eng. Soc.*, **26**, 139-144 (1978, *Originally published in 1928*).
- ⁶⁷ F. Murray, "An Application of Bob Smith's Phasing Plug," presented at the 61st convention of the AES, New York, preprint 1384 (1978).

- ⁶⁸ C. A. Henricksen, “Phase Plug Modeling and Analysis: Radial versus Circumferential Types,” presented at the 59th AES Convention, Hamburg, preprint 1328 (1978).
- ⁶⁹ M. Dodd and J. Ocle-Brown, “A New Methodology for the Acoustic Design of Compression Driver Phase Plugs with Radial Channels,” presented at the 125th AES Convention, San Francisco, Convention Paper 7532 (2008).
- ⁷⁰ E. C. Wente, “Sound Translating Device,” US Patent No. 2037187 (1933).
- ⁷¹ E. Geddes, “Compression Driver Plug,” US Patent No. 2006/0034475 A1 (2006).
- ⁷² E. Geddes, *Audio Transducers*, (GedLee Publishing, 2002).
- ⁷³ W. Soedel, *Vibrations of Shells and Plates 3rd Ed.* (Marcel Dekker, New York, 2004).
- ⁷⁴ L. N. Trefethen and D. Bau, *Numerical Linear Algebra* (SIAM, Philadelphia, 1997).

Appendix

MATLAB Code

The code used to compute the finite-difference computations of Ch. 3 is given here. Each function called by MainWave.m is given in as a different section of the appendix

A.1 MainWave.m

```
%-----  
% FD code used to compute transient radiation from a finite-length,  
% infinitely-baffled pipe.  
%  
% Created By Daniel Tengelsen and Sebastian Acosta  
%  
% Stepanishen and Tougas' model reduced by a factor of 4. Hence,  
% Stepanishen Frequencies: 200, 2000, 2500, 4000, 5000, 10000  
% Our Frequenceis:      800, 8000, 10000, 16000, 20000, 40000  
%-----  
clear all; close all; clc;  
  
%-----  
%                               Global Variables  
%-----  
global x y;  
global u v vrms;  
global jacobian delta;  
global alpha beta gamma;
```

```

global xxi xeta xxixi xetaeta xxieta yxi yeta yxixi yetaeta yxieta;
global axi geta;
global lambda kappa;
global R;
global i1 i3;
global Xc Yc;
global P_dt P_field;

%-----
%                               Initial Data
%-----

% Grid Parameters
%-----
N1 = 51;                               % Number of Xi-curves
N2 = 31;                               % Number of Eta-curves
TOL = 1e-6;                            % Tolerance grid
N = 10000;                             % Max number of SOR iterations
w = 1.9;                                % SOR parameter

% Field Parameters
%-----
freq = 8000;                            % Frequency [Hz]
dt = 3.0e-7;                            % Time step [s]
brk = round(1/(freq*dt));
dt = 1/(freq*brk);
TimeMax = 0.0042;                       % Physical Time [s]
Tmax = TimeMax/dt;                      % Maximum Number of time steps
C = 343;                                 % Wave speed [m/s]
imag = 1i;                               % Imaginary unit

% Initializing Variables
%-----
x = zeros(N1,N2);                       % X-coordinates
y = zeros(N1,N2);                       % Y-coordinates
u = zeros(N1,N2);                       % Grid plotter
v = zeros(N1,N2,3);                     % Pressure Field
vrms = zeros(N1,N2);                    % RMS Pressure Field
jacobian = zeros(N1,N2);                 % jacobian
delta = zeros(N1,N2);                   % jacobian
alpha = zeros(N1,N2);                   % alpha metric factor
gamma = zeros(N1,N2);                   % gamma metric factor
beta = zeros(N1,N2);                    % beta metric factor
xxi = zeros(N1,N2);                     % Coord Deriv
xeta = zeros(N1,N2);                    % Coord Deriv
yxi = zeros(N1,N2);                     % Coord Deriv
yeta = zeros(N1,N2);                    % Coord Deriv
xxieta = zeros(N1,N2);                  % Coord Deriv
yxixi = zeros(N1,N2);                   % Coord Deriv
xetaeta = zeros(N1,1);                  % Coord Deriv
yetaeta = zeros(N1,1);                  % Coord Deriv
axi = zeros(N1,N2);                     % metric factor derivatives
geta = zeros(N1,N2);                     % metric factor derivatives

```

```

lambda = zeros(N2,1);           % Auxiliary variables
kappa = zeros(N2,1);           % Auxiliary variables
R = zeros(N2,1);               % Absorbing Radius

%-----
%                               Grid Generation Algorithm
%-----
fprintf('\n***** \n');
fprintf('***** GENERATING ELLIPTIC GRIDS ***** \n');
fprintf('***** \n\n');

% Choose the grid to be created
%-----
i1 = Horn_Step(N1,N2,-0.000);   Go to Horn Step

% Create Initial Grid for SOR
%-----
InitialGrid(N1,N2,i1);        Go to InitialGrid

% Okay Initial Grid
%-----
figure
mesh(x,y,u,'EdgeColor','black');
xlabel('x','FontSize',18);
ylabel('y','FontSize',18);
axis equal;
set(gca,'FontSize',18)
view(0,90);
title('INITIAL GRID - Press Enter to Continue','FontSize',18);
pause

% Calling Grid Generator
%-----
time1 = cputime;
[iter,err] = gridgen(N1,N2,TOL,N,w); Go to gridgen
time2 = cputime;

% Reporting Grid Generation Results
%-----
fprintf('\n\t\tNumber of Iterations:\t%.0f \n',iter);
fprintf('\t\tMaximum Point-Error: \t%e \n',err);
fprintf('\t\tTime Lapse: \t%0.2f sec\n\n',time2-time1);

% Plotting Final Grid
%-----
mesh(x,y,u,'EdgeColor','black');
xlabel('x','FontSize',18);
ylabel('y','FontSize',18);
axis equal;
view(0,90);
title('FINAL GRID - Press Enter to Continue','FontSize',18);

%-----

```

```

%                               Leapfrog Finite-Difference Scheme
%-----

% Computing Metric Factors
%-----
Metrics_Step(N1,N2);                               Go to Metrics Step

% Computing the Courant Number
%-----
CFL = min(min(delta(1:N1-1,1:N2-1)))/C;
fprintf('\n\t The Courant Number is: \t %.2e \n',CFL);

% Initial Conditions
%-----
for i=1:N1,
    for j=1:N2,
        v(i,j,1) = 0;
        v(i,j,2) = v(i,j,1);
    end
end

% Initial Field
%-----
figure,
surf(x,y,v(:,:,2));
shading interp;
caxis([-1 1]);
xlabel('x','FontSize',18);
ylabel('y','FontSize',18);
title('INITIAL FIELD - Press Enter to Continue','FontSize',18);
axis([x(1,1) x(N1,1) min(min(y(1,1))) max(max(y)) -2 2]);
set(gca,'FontSize',18)
view(0,90)

%Starting Leapfrog Scheme
%-----
fprintf('\n***** \n');
fprintf('***** IMPLEMENTING LEAPFROG SCHEME ***** \n');
fprintf('***** \n');
fprintf('\nPRESS ENTER TO CONTINUE ... \n ');
pause

LeapFrog_Step(freq,C,dt,Tmax,N1,N2);               Go to LeapFrogHigher

%-----
%                               Plotting Results
%-----
figure
dir = [P_dt(end:-1:2,1:end); P_dt(:,1:end)];
t = linspace(0,dt*length(dir(1,:)),length(dir(1,:)));
th = [-pi/2:pi/(length(dir(:,1))-1):pi/2]*180/pi;
surf(t(7500:end),th,abs(dir(:,7500:end)));

```

```

xlim([2.8e-3, 4.2e-3])
ylim([-90, 90])
view(0,90)
shading interp
xlabel('time (sec)','FontSize',18)
ylabel('angle (rad)','FontSize',18)
title(['Directivity vs. Time at f = ' num2str(freq)],'FontSize',18)

figure
surf(t(7500:end),th,abs(dir(:,7500:end)));
xlim([2.8e-3, 4.2e-3])
ylim([-90, 90])
view(45,50)
shading interp
xlabel('time (sec)','FontSize',18)
ylabel('angle (rad)','FontSize',18)
title(['Directivity vs. Time at f = ' num2str(freq)],'FontSize',18)

% Final Field
figure,
surf(t(7500:end),th,abs(dir(:,7500:end)));
xlim([2.8e-3, 4.2e-3])
ylim([-90, 90])
view(-68,74)
shading interp
xlabel('time (sec)','FontSize',18)
ylabel('angle (rad)','FontSize',18)
title(['Directivity vs. Time at f = ' num2str(freq)],'FontSize',18)

fprintf('\n***** \n');
fprintf('***** END OF PROGRAM ***** \n');
fprintf('***** \n');

```

A.2 LeapFrog_Step.m

```

%-----
% This function is used in MainWave
% It computes Leapfrog algorithm for any acceleration profile,
% specifically higher-order modes of the pipe.
%
% Created by Daniel Tengelsen and Sebastian Acosta
%-----

function LeapFrog_Step(freq,C,dt,Tmax,N1,N2)

%-----
%
%                               Global Variables

```

```

%-----
global x y v vrms;
global jacobian;
global alpha beta gamma;
global xxi xeta xxixi xetaeta xxieta yxi yeta yxixi yetaeta yxieta;
global axi geta;
global lambda kappa;
global R;
global P_dt P_field;

%-----
%
%                               Initial Data
%-----
ghostw = zeros(N1,1);
ghosta = zeros(N1,1);
ghosts = zeros(N2,1);

% Field Parameters
%-----
w = 2*pi*freq;           % Angular Frequency
rad = 0.75*0.0254;      % Pipe radius
r = linspace(0,rad,N2); % Grid points along pipe radius
rho = 1.21;             % Density of Air

k = 0;                  % Index for pressure magnitude
iter = 1;               % Index for pressure at infinite boundary
n=1;                    % Index for Leapfrog algorithm
mi = 1;                 % Index for pressure field snapshots

%-----
%                               Leapfrog Algorithm
%-----
while (n <= Tmax),
    % Constant velocity boundary condition
    %-----
    if n <= 1/(freq*dt)
        uN = 1e-2;
        mc = 3.83;           % Mode coefficient (zeros of BesselJ_1)
        %
        ES = uN*besselj(0,0/rad*r)*sin(w*(n-1)*dt); %Excitation Signal
        dES = -w*uN*besselj(0,mc/rad*r)*cos(w*(n-1)*dt); %Time Deriv. of ES
    else
        ES = 0;             %Excitation Signal
        dES = zeros(size(r)); %Time Deriv. of ES
    end

    % Advance in time inner points
    %-----
    for i = 2:N1-1,
        for j = 2:N2-1,
            vxi = (v(i+1,j,2)-v(i-1,j,2))/2;
            veta = (v(i,j+1,2)-v(i,j-1,2))/2;
            vxixi = v(i+1,j,2)-2*v(i,j,2) +v(i-1,j,2);
            vetaeta = v(i,j+1,2)-2*v(i,j,2)+v(i,j-1,2);

```

```

vxieta = (v(i+1,j+1,2)-v(i+1,j-1,2)-v(i-1,j+1,2)+v(i-1,j-1,2))/4;

v(i,j,3) = (C*dt)^2*((alpha(i,j)*vxixi ...
- 2*beta(i,j)*vxieta ...
+ gamma(i,j)*vetaeta ...
+ 0.5*axi(i,j)*vxi + 0.5*geta(i,j)*veta)/jacobian(i,j)^2 ...
+ (veta*xxi(i,j) - vxi*xeta(i,j))/(y(i,j)*jacobian(i,j)) ...
+ 2*v(i,j,2) - v(i,j,1);
end
end

% Solve for Ghost Points for the Source boundary
%-----
for j = 2:N2-1,
veta = (v(1,j+1,2)-v(1,j-1,2))/2;
ghosts(j) = v(2,j,2) ...
- 2/alpha(1,j)*(beta(1,j)*veta...
+ jacobian(1,j)*sqrt(alpha(1,j))*dES(j)*rho);
end

% Bottom Left
veta = -(3*v(1,1,2) - 4*v(1,2,2) + v(1,3,2))/2;

ghosts(1) = v(2,1,2) ...
- 2/alpha(1,1)*(beta(1,1)*veta...
+ jacobian(1,1)*sqrt(alpha(1,1))*dES(1)*rho);

% Top Left (this is rigid)
veta = (3*v(1,N2,2) - 4*v(1,N2-1,2) + v(1,N2-2,2))/2;

ghosts(N2) = v(2,N2,2) ...
- 2/alpha(1,N2)*(beta(1,N2)*veta...
+ jacobian(1,N2)*sqrt(alpha(1,N2))*dES(N2)*rho);

% Solve for Ghost Points for the wall and absorbing boundaries
%-----
for i=2:N1-1,
ghostw(i) = beta(i,N2)/gamma(i,N2)*(v(i+1,N2,2)-v(i-1,N2,2)) ...
+ v(i,N2-1,2);
ghosta(i) = v(i,2,2);
end
ghostw(1) = beta(1,N2)/gamma(1,N2)*(v(2,N2,2)-ghosts(N2)) + v(1,N2-1,2);
ghosta(1) = v(1,2,2);

% Advance in time at rigid wall
%-----
for i=2:N1-1,
vxi = (v(i+1,N2,2)-v(i-1,N2,2))/2;
veta = (ghostw(i)-v(i,N2-1,2))/2;
vxixi = v(i+1,N2,2)-2*v(i,N2,2)+v(i-1,N2,2);
vetaeta = ghostw(i)-2*v(i,N2,2)+v(i,N2-1,2);
vxieta = (ghostw(i+1)-v(i+1,N2-1,2)-ghostw(i-1)+v(i-1,N2-1,2))/4;

```

```

v(i,N2,3) = (C*dt)^2*((alpha(i,N2)*vxixi ...
- 2*beta(i,N2)*vxieta ...
+ gamma(i,N2)*vetaeta ...
+ 0.5*axi(i,N2)*vxi + 0.5*geta(i,N2)*veta)/jacobian(i,N2)^2 ...
+ (veta*xxi(i,N2) - vxi*xeta(i,N2))/(y(i,N2)*jacobian(i,N2)) ...
+ 2*v(i,N2,2) - v(i,N2,1);
end

% Advance in time at rigid wall - Corner Point (Top Left)
%-----
vxi = (v(2,N2,2)-ghosts(N2))/2;
veta = (ghostw(1)-v(1,N2-1,2))/2;
vxixi = v(2,N2,2)-2*v(1,N2,2)+ghosts(N2);
vetaeta = ghostw(1) - 2*v(1,N2,2) + v(1,N2-1,2);
vxieta = ((3*v(2,N2,2) - 4*v(2,N2-1,2) + v(2,N2-2,2)) ...
- (3*ghosts(N2) - 4*ghosts(N2-1) + ghosts(N2-2)))/4;

v(1,N2,3) = (C*dt)^2*((alpha(1,N2)*vxixi ...
- 2*beta(1,N2)*vxieta ...
+ gamma(1,N2)*vetaeta ...
+ 0.5*axi(1,N2)*vxi + 0.5*geta(1,N2)*veta)/jacobian(1,N2)^2 ...
+ (veta*xxi(1,N2) - vxi*xeta(1,N2))/(y(1,N2)*jacobian(1,N2)) ...
+ 2*v(1,N2,2) - v(1,N2,1);

% Advance in time at Absorbing Boundary
%-----
for j=2:N2-1,
veta = (v(N1,j+1,2)-v(N1,j-1,2))/2;
vetaeta = v(N1,j+1,2)-2*v(N1,j,2)+v(N1,j-1,2);
vxieta = (3*v(N1,j+1,2)-4*v(N1-1,j+1,2)+v(N1-2,j+1,2) ...
-3*v(N1,j-1,2)+4*v(N1-1,j-1,2)-v(N1-2,j-1,2))/4;

v(N1,j,3) = 1/(1+C*dt*R(j)/(jacobian(N1,j)*lambda(j)) ...
*(alpha(N1,j)+0.25*axi(N1,j) ...
-xeta(N1,j)*jacobian(N1,j)/(2*y(N1,j))) ...
*((C*dt)^2/jacobian(N1,j)^2 ...
*((alpha(N1,j)+0.25*axi(N1,j) ...
-xeta(N1,j)*jacobian(N1,j)/(2*y(N1,j))) ...
*(-2*kappa(j)/lambda(j)*veta ...
- jacobian(N1,j)/lambda(j)*v(N1,j,2) ...
+ R(j)*jacobian(N1,j)/(C*lambda(j)*dt)*v(N1,j,1)) ...
+ 2*alpha(N1,j)*(v(N1-1,j,2) - v(N1,j,2)) ...
- 2*beta(N1,j)*vxieta + gamma(N1,j)*vetaeta ...
+ (geta(N1,j)/2+xxi(N1,j)*jacobian(N1,j)/y(N1,j))*veta) ...
+ 2*v(N1,j,2) - v(N1,j,1));
end

% Advance in time at Source
%-----
for j = 2:N2-1,
vxi = (v(2,j,2)-ghosts(j))/2;
veta = (v(1,j+1,2)-v(1,j-1,2))/2;
vxixi = v(2,j,2)-2*v(1,j,2) +ghosts(j);

```

```

vetaeta = v(1,j+1,2)-2*v(1,j,2)+v(1,j-1,2);
vxieta = (v(2,j+1,2)-v(2,j-1,2)-ghosts(j+1)+ghosts(j-1))/4;

v(1,j,3) = (C*dt)^2*((alpha(1,j)*vxixi ...
- 2*beta(1,j)*vxieta ...
+ gamma(1,j)*vetaeta ...
+ 0.5*axi(1,j)*vxi + 0.5*geta(1,j)*veta)/jacobian(1,j)^2 ...
+ (veta*xxi(1,j) - vxi*xeta(1,j))/(y(1,j)*jacobian(1,j)) ...
+ 2*v(1,j,2) - v(1,j,1);
end

% Advance in time at axis of symmetry
%-----
for i=2:N1-1,
vxi = (v(i+1,1,2)-v(i-1,1,2))/2;
veta = (v(i,2,2)-ghosta(i))/2;
vxixi = v(i+1,1,2)-2*v(i,1,2)+v(i-1,1,2);
vetaeta = v(i,2,2)-2*v(i,1,2)+ghosta(i);
vxieta = (v(i+1,2,2)+ghosta(i-1)-v(i-1,2,2)-ghosta(i+1))/4;

v(i,1,3) = (C*dt)^2*((alpha(i,1)*vxixi ...
- 2*beta(i,1)*vxieta*0 ...
+ gamma(i,1)*vetaeta ...
+ 0.5*axi(i,1)*vxi + 0.5*geta(i,1)*veta)/jacobian(i,1)^2 ...
+ (xeta(i,1)^2*yxixi(i)-2*xxi(i,1)*xeta(i,1)*yxieta(i) ...
+xxi(i,1)^2*yetaeta(i))* (xeta(i,1)*vxi-xxi(i,1)*veta) ...
/jacobian(i,1)^3 ...
+ (xeta(i,1)^2*xxixi(i)-2*xxi(i,1)*xeta(i,1)*xxieta(i) ...
+xxi(i,1)^2*xetaeta(i))* (yxi(i,1)*veta-yeta(i,1)*vxi) ...
/jacobian(i,1)^3) ...
+ 2*v(i,1,2) - v(i,1,1);
end

% Advance in time at corner (Bottom Left)
%-----
vxi = (v(2,1,2)-ghosts(1))/2;
veta = 0; %(v(1,2,2)-ghosta(1))/2;
vxixi = v(2,1,2)-2*v(1,1,2)+ghosts(1);
vetaeta = v(1,2,2)-2*v(1,1,2)+ghosta(1);
vxieta = (v(2,2,2)-ghosta(1)-(-3*ghosts(1) + 4*ghosts(2) - ghosts(3)))/4;

v(1,1,3) = (C*dt)^2*((alpha(1,1)*vxixi ...
- 2*beta(1,1)*vxieta ...
+ gamma(1,1)*vetaeta ...
+ 0.5*axi(1,1)*vxi + 0.5*geta(1,1)*veta)/jacobian(1,1)^2 ...
+ (xeta(1,1)^2*yxixi(1)-2*xxi(1,1)*xeta(1,1)*yxieta(1) ...
+xxi(1,1)^2*yetaeta(1))* (xeta(1,1)*vxi-xxi(1,1)*veta) ...
/jacobian(1,1)^3 ...
+ (xeta(1,1)^2*xxixi(1)-2*xxi(1,1)*xeta(1,1)*xxieta(1) ...
+xxi(1,1)^2*xetaeta(1))* (yxi(1,1)*veta-yeta(1,1)*vxi) ...
/jacobian(1,1)^3) ...
+ 2*v(1,1,2) - v(1,1,1);

% Advance in time at corner (Bottom Right)

```

```

%-----
for i=N1,
    v(i,1,3)=(4*v(i,2,3)-v(i,3,3))/3;
end

% Advance in time at corner (Top Right)
%-----
v(N1,N2,3)=(4*v(N1,N2-1,3)-v(N1,N2-2,3))/3;

%-----
%
%                               Plots and Updates
%-----
% Real Time Animation
%-----
if (mod(n,10)==0),
    surf(x,y,(v(:,:,2))); hold on;
    surf(x,-y,(v(:,:,2))); hold off;
    shading interp;
    colorbar
    caxis([-0.015 0.015]);
    xlabel('x','FontSize',18);
    ylabel('y','FontSize',18);
    title(['Time Iter =',num2str(n), ' and Frequency = ', ...
           num2str(freq)], 'Fontsize',16,'Fontweight','demi');
    axis([x(1,1) x(N1,1) 0 max(max(y)) -2 2]);
    view(0,60);
    pause(0.01);
end

% Calculates Pressure Magnitude field after system is in steady state
%-----
if n >= round(Tmax-1/freq/dt),
    t = k*dt;
    vrms = (vrms*t + abs(v(:,:,2)).^2*dt)/(t+dt);
    k = k+1;
end
P_dt(1:N2,iter) = v(N1,:,2)';
iter = iter+1;

% Snapshots of Pressure Field
%-----
if n == 301 || n == 4441 || n == 8601
    P_field(:,:,mi) = v(:,:,2);
    mi = mi + 1;
end

% Update
%-----
n = n + 1;
v(:,:,1) = v(:,:,2);
v(:,:,2) = v(:,:,3);
end
vrms = sqrt(vrms);
return

```

A.3 Horn_Step.m

```

%-----
% This function is used in MainWave
% It computes the initial boundaries to form the initial grid.
%
% Created by Daniel Tengelsen and Sebastian Acosta
%-----

function i1 = Horn_Step(N1,N2,curve)

%-----
%                               Global Variables
%-----

global x y;
global R;
global i3;

%-----
%                               Initial Data
%-----
scale = 0.0254;           % Conversion factor between inches and meters
rad = 0.75;              % Radius of the pipe (inches)
i3 = N2-1;
R = 20*scale*ones(N2,1); % Radius from pipe exit to absorbing boundary

%-----
%                               Definiting Main Vertices
%-----
% Vertex 1
%-----
x(1,1) = -19.685*scale;
y(1,1) = 0;

% Vertex 2
%-----
x(N1,1) = R(1);
y(N1,1) = 0;

% Interpolate between vertices 1 and 2
%-----
interpoint(x(1,1),x(N1,1),y(1,1),y(N1,1),1,N1,1,1); Go to interpoint

% Vertex 3
%-----
x(N1,N2) = 0;
y(N1,N2) = R(1);

[val,i1] = min(abs(x(:,1)-0.001));
xinc = 19.685/(i1-1);
anginc = pi/2/(N2-1); % Angular Increment

```

```

% Vertex 4
%-----
x(i1,N2) = 0;
y(i1,N2) = rad*scale;

% Vertex 5
%-----
x(1,N2) = -19.685*scale;
y(1,N2) = rad*scale;

%-----
%                               Other Interpolation Between Vertices
%-----
% Interpolate between vertices 2 and 3
%-----
ang = 0;
for j=1:N2,
    x(N1,j) = R(j)*cos(ang);
    y(N1,j) = R(j)*sin(ang);
    ang = ang + anginc;
end

% Interpolate between vertices 3 and 4
%-----
interpoint(x(i1,N2),x(N1,N2),y(i1,N2),y(N1,N2),i1,N1,N2,1);

% Interpolate between vertices 4 and 5
%-----
for i=1:i1,
    x(i,N2) = x(1,N2) + (i-1)*xinc*scale;
    y(i,N2) = rad*scale;
end

% Interpolate between vertices 1 and 5
%-----
interpoint(x(1,1),x(1,N2),y(1,1),y(1,N2),1,N2,1,2);
for j=1:N2,
    x(1,j) = x(1,j) + curve*cos(pi/2*(j-1)/(N2-1));
end

return

```

A.4 Metrics_Step.m

```

%-----
% This function is used in MainWave
% It computes the values of all metric factors (alpha, gamma,
% beta), the jacobian, and the metric factor's partial derivatives.

```

```

%
% Created by Daniel Tengelsen and Sebastian Acosta
%-----

function Metrics_Step(N1,N2)

%-----
%                               Global Variables
%-----

global x y;
global jacobian delta;
global alpha beta gamma;
global xxi xeta yxi yeta;
global axi geta;
global lambda kappa;

%-----
%                               Computation of Metrics
%-----

% Interior Points
%-----
for j=2:N2-1,
    for i=2:N1-1,
        xxi(i,j)=(x(i+1,j)-x(i-1,j))/2;
        xeta(i,j)=(x(i,j+1)-x(i,j-1))/2;
        yxi(i,j)=(y(i+1,j)-y(i-1,j))/2;
        yeta(i,j)=(y(i,j+1)-y(i,j-1))/2;
        xxixeta = (x(i+1,j+1)-x(i+1,j-1)-x(i-1,j+1)+x(i-1,j-1))/4;
        yxiyeta = (y(i+1,j+1)-y(i+1,j-1)-y(i-1,j+1)+y(i-1,j-1))/4;

        jacobian(i,j) = xxi(i,j)*yeta(i,j)-xeta(i,j)*yxi(i,j);
        alpha(i,j) = xeta(i,j)^2+yeta(i,j)^2;
        gamma(i,j) = xxi(i,j)^2+yxi(i,j)^2;
        beta(i,j) = xxi(i,j)*xeta(i,j)+yxi(i,j)*yeta(i,j);
        axi(i,j) = 2*(xeta(i,j)*xxixeta+yeta(i,j)*yxiyeta);
        geta(i,j) = 2*(xxi(i,j)*xxixeta+yxi(i,j)*yxiyeta);
        delta(i,j) = jacobian(i,j)/sqrt(alpha(i,j)+gamma(i,j)+2*beta(i,j));
    end
end

% Axis of Symmetry Points
%-----
for i=2:N1-1,
    xxi(i,1) = (x(i+1,1)-x(i-1,1))/2;
    xeta(i,1) = (-3*x(i,1)+4*x(i,2)-x(i,3))/2;
    yxi(i,1) = (y(i+1,1)-y(i-1,1))/2;
    yeta(i,1) = (-3*y(i,1)+4*y(i,2)-y(i,3))/2;
    xxixeta = (-3*x(i+1,1)+4*x(i+1,2)-x(i+1,3)+3*x(i-1,1) ...
        -4*x(i-1,2)+x(i-1,3))/4;
    yxiyeta = (-3*y(i+1,1)+4*y(i+1,2)-y(i+1,3)+3*y(i-1,1) ...
        -4*y(i-1,2)+y(i-1,3))/4;

    jacobian(i,1) = xxi(i,1)*yeta(i,1)-xeta(i,1)*yxi(i,1);
    alpha(i,1) = xeta(i,1)^2+yeta(i,1)^2;
end

```

```

gamma(i,1) = xxi(i,1)^2+yxi(i,1)^2;
beta(i,1) = xxi(i,1)*xeta(i,1)+yxi(i,1)*yeta(i,1);
axi(i,1) = 2*(xeta(i,1)*xxieta+yeta(i,1)*yxieta);
geta(i,1) = 2*(xxi(i,1)*xxieta+yxi(i,1)*yxieta);
delta(i,1) = jacobian(i,1)/sqrt(alpha(i,1)+gamma(i,1)+2*beta(i,1));
end

% Rigid Wall Points
%-----
for i=2:N1-1
xxi(i,N2) = (x(i+1,N2)-x(i-1,N2))/2;
xeta(i,N2) = (3*x(i,N2)-4*x(i,N2-1)+x(i,N2-2))/2;
yxi(i,N2) = (y(i+1,N2)-y(i-1,N2))/2;
yeta(i,N2) = (3*y(i,N2)-4*y(i,N2-1)+y(i,N2-2))/2;
xxieta = (3*x(i+1,N2)-4*x(i+1,N2-1)+x(i+1,N2-2)-3*x(i-1,N2)...
+4*x(i-1,N2-1)-x(i-1,N2-2))/4;
yxieta = (3*y(i+1,N2)-4*y(i+1,N2-1)+y(i+1,N2-2)-3*y(i-1,N2)...
+4*y(i-1,N2-1)-y(i-1,N2-2))/4;

jacobian(i,N2) = xxi(i,N2)*yeta(i,N2)-xeta(i,N2)*yxi(i,N2);
alpha(i,N2) = xeta(i,N2)^2+yeta(i,N2)^2;
gamma(i,N2) = xxi(i,N2)^2+yxi(i,N2)^2;
beta(i,N2) = xxi(i,N2)*xeta(i,N2)+yxi(i,N2)*yeta(i,N2);
axi(i,N2) = 2*(xeta(i,N2)*xxieta+yeta(i,N2)*yxieta);
geta(i,N2) = 2*(xxi(i,N2)*xxieta+yxi(i,N2)*yxieta);
delta(i,N2) = jacobian(i,N2)/sqrt(alpha(i,N2)+gamma(i,N2)+2*beta(i,N2));
end

% Absorbing Points
%-----
for j=2:N2-1,
xxi(N1,j) = (3*x(N1,j)-4*x(N1-1,j)+x(N1-2,j))/2;
xeta(N1,j) = (x(N1,j+1)-x(N1,j-1))/2;
yxi(N1,j) = (3*y(N1,j)-4*y(N1-1,j)+y(N1-2,j))/2;
yeta(N1,j) = (y(N1,j+1)-y(N1,j-1))/2;
xxieta = (3*x(N1,j+1)-4*x(N1-1,j+1)+x(N1-2,j+1)-3*x(N1,j-1)...
+4*x(N1-1,j-1)-x(N1-2,j-1))/4;
yxieta = (3*y(N1,j+1)-4*y(N1-1,j+1)+y(N1-2,j+1)-3*y(N1,j-1)...
+4*y(N1-1,j-1)-y(N1-2,j-1))/4;

jacobian(N1,j) = xxi(N1,j)*yeta(N1,j)-xeta(N1,j)*yxi(N1,j);
alpha(N1,j) = xeta(N1,j)^2+yeta(N1,j)^2;
gamma(N1,j) = xxi(N1,j)^2+yxi(N1,j)^2;
beta(N1,j) = xxi(N1,j)*xeta(N1,j)+yxi(N1,j)*yeta(N1,j);
axi(N1,j) = 2*(xeta(N1,j)*xxieta+yeta(N1,j)*yxieta);
geta(N1,j) = 2*(xxi(N1,j)*xxieta+yxi(N1,j)*yxieta);
delta(N1,j) = jacobian(N1,j)/sqrt(alpha(N1,j)+gamma(N1,j)+2*beta(N1,j));
lambda(j) = x(N1,j)*yeta(N1,j)-y(N1,j)*xeta(N1,j);
kappa(j) = y(N1,j)*xxi(N1,j)-x(N1,j)*yxi(N1,j);
end

% Source Boundary
%-----
for j=2:N2-1,

```

```

xxi(1,j) = -(3*x(1,j)-4*x(2,j)+x(3,j))/2;
xeta(1,j) = (x(1,j+1)-x(1,j-1))/2;
yxi(1,j) = -(3*y(1,j)-4*y(2,j)+y(3,j))/2;
yeta(1,j) = (y(1,j+1)-y(1,j-1))/2;
xxieta = -(3*x(1,j+1)-4*x(2,j+1)+x(3,j+1)-3*x(1,j-1) ...
+4*x(2,j-1)-x(3,j-1))/4;
yxieta = -(3*y(1,j+1)-4*y(2,j+1)+y(3,j+1)-3*y(1,j-1) ...
+4*y(2,j-1)-y(3,j-1))/4;

jacobian(1,j) = xxi(1,j)*yeta(1,j)-xeta(1,j)*yxi(1,j);
alpha(1,j) = xeta(1,j)^2+yeta(1,j)^2;
gamma(1,j) = xxi(1,j)^2+yxi(1,j)^2;
beta(1,j) = xxi(1,j)*xeta(1,j)+yxi(1,j)*yeta(1,j);
axi(1,j) = 2*(xeta(1,j)*xxieta+yeta(1,j)*yxieta);
geta(1,j) = 2*(xxi(1,j)*xxieta+yxi(1,j)*yxieta);
delta(1,j) = jacobian(1,j)/sqrt(alpha(1,j)+gamma(1,j)+2*beta(1,j));
end

% Corner Points (Top Left)
%-----
xxi(1,N2) = -(3*x(1,N2)-4*x(2,N2)+x(3,N2))/2;
xeta(1,N2) = (3*x(1,N2)-4*x(1,N2-1)+x(1,N2-2))/2;
yxi(1,N2) = -(3*y(1,N2)-4*y(2,N2)+y(3,N2))/2;
yeta(1,N2) = (3*y(1,N2)-4*y(1,N2-1)+y(1,N2-2))/2;
xxieta(1,N2) = (3*(-3*x(1,N2)+4*x(2,N2)-x(3,N2)) ...
-4*(-3*x(1,N2-1)+4*x(2,N2-1)-x(3,N2-1)) ...
+(-3*x(1,N2-2)+4*x(2,N2-2)-x(3,N2-2)))/4;
yxieta(1,N2) = (3*(-3*y(1,N2)+4*y(2,N2)-y(3,N2)) ...
-4*(-3*y(1,N2-1)+4*y(2,N2-1)-y(3,N2-1)) ...
+(-3*y(1,N2-2)+4*y(2,N2-2)-y(3,N2-2)))/4;

jacobian(1,N2) = xxi(1,N2)*yeta(1,N2)-xeta(1,N2)*yxi(1,N2);
alpha(1,N2) = xeta(1,N2)^2+yeta(1,N2)^2;
gamma(1,N2) = xxi(1,N2)^2+yxi(1,N2)^2;
beta(1,N2) = xxi(1,N2)*xeta(1,N2)+yxi(1,N2)*yeta(1,N2);
axi(1,N2) = 2*(xeta(1,N2)*xxieta(1,N2)+yeta(1,N2)*yxieta(1,N2));
geta(1,N2) = 2*(xxi(1,N2)*xxieta(1,N2)+yxi(1,N2)*yxieta(1,N2));
delta(1,N2) = jacobian(1,N2)/sqrt(alpha(1,N2)+gamma(1,N2)+2*beta(1,N2));

% Corner Points (Bottom Left)
%-----
xxi(1,1) = -(3*x(1,1)-4*x(2,1)+x(3,1))/2;
xeta(1,1) = 0; %-(3*x(1,1)-4*x(1,2)+x(1,3))/2;
yxi(1,1) = 0; %-(3*y(1,1)-4*y(2,1)+y(3,1))/2;
yeta(1,1) = y(1,2); %-(3*y(1,1)-4*y(1,2)+y(1,3))/2;
xxieta(1,1) = 0; %-(3*(-3*x(1,1)+4*x(2,1)-x(3,1)) ...
% -4*(-3*x(1,2)+4*x(2,2)-x(3,2)) ...
% +(-3*x(1,3)+4*x(2,3)-x(3,3)))/4;
yxieta(1,1) = (-3*y(1,2)+4*y(2,2)-y(3,2))/2;
xxixi(1) = 2*x(1,1) - 5*x(2,1) + 4*x(3,1) - x(4,1);
yxixi(1) = 0; %2*y(1,1) - 5*y(2,1) + 4*y(3,1) - y(4,1);
xetaeta(1) = -2*x(1,1)+2*x(1,2);
yetaeta(1) = 0; %-2*y(1,1);

```



```

%-----
%                               Linear Interpolation Between Points
%-----
for i=2:N1-1,
    interpoint(x(i,1),x(i,N2),y(i,1),y(i,N2),1,N2,i,2);
end

for j=2:N2-1,
    interpoint(x(i1,j),x(N1,j),y(i1,j),y(N1,j),i1,N1,j,1);
end

return

```

A.6 *interpoint.m*

```

%-----
%This function is used in Horn_Step
%It interpolates linearly between points
%Created By Sebastian Acosta
%
%starting point (x0,y0) with n = c0
%final point (xf,yf) with n = cf
%-----
function interpoint(x0,xf,y0,yf,c0,cf,n,flag)
%-----
%                               Global Variables
%-----
global x y;
%-----
%                               Linear Interpolation Between Points
%-----
if flag == 1,
    for i=c0:cf,
        x(i,n) = x0 + (i-c0)*(xf-x0)/(cf-c0);
        y(i,n) = y0 + (i-c0)*(yf-y0)/(cf-c0);
    end
end

if flag == 2,
    for j=c0:cf,
        x(n,j) = x0 + (j-c0)*(xf-x0)/(cf-c0);
        y(n,j) = y0 + (j-c0)*(yf-y0)/(cf-c0);
    end
end

return

```

A.7 gridgen.m

```

%-----
% This function is used in MainWave
% It create the curvilinear grid using Successive Overrelaxation.
%
% Created by Daniel Tengelsen and Sebastian Acosta
%-----

% The generation process is animated in real time.

function [k,err] = gridgen(N1,N2,tol,N,w)

%-----
%
%                               Global Variables
%-----
global x y u;

%-----
%
%                               SOR Algorithm
%-----
k = 0;                               % iteration counter
error2 = 0;                           % Error in vector norm 2
err = tol;                             % absolute error

while(k<N && err >= tol && error2 < 10);

    k = k+1;

    % Making a copy of the current coordinate points
    %-----
    xc = x;
    yc = y;

    % Performing grid generations
    %-----
    for i=2:N1-1,
        d = i-1;
        e = i+1;

        xxi = 0.5*(x(e,1)-x(d,1));
        yeta = 0.5*(y(i,2)+y(i,2));
        a = yeta^2;
        g = xxi^2;
        aux1 = 0.5/(a+g);

        % Approximate coordinate x
        %-----
        aux2 = a*(x(e,1)+x(d,1));
        aux4 = g*(x(i,2)+x(i,2));

```

```

x(i,1) = aux1*(aux2+aux4);
x(i,1) = (1.-w)*xc(i,1)+w*x(i,1);

for j=2:N2-1,
    f = j-1;
    gg = j+1;

    xxi = 0.5*(x(e,j)-x(d,j));
    yxi = 0.5*(y(e,j)-y(d,j));
    xeta = 0.5*(x(i,gg)-x(i,f));
    yeta = 0.5*(y(i,gg)-y(i,f));
    xxieta = (x(e,gg)-x(e,f)-x(d,gg)+x(d,f))/4;
    yxieta = (y(e,gg)-y(e,f)-y(d,gg)+y(d,f))/4;

    a = xeta^2+yeta^2;
    b = xxi*xeta+yxi*yeta;
    g = xxi^2+yxi^2;

    aux1 = 0.5/(a+g);

    % Approximate coordinate x
    %-----
    aux2 = a*(x(e,j)+x(d,j));
    aux4 = g*(x(i,gg)+x(i,f));
    aux10 =
(xxi*xxieta+yxi*yxieta)*xeta+(xeta*xxieta+yeta*yxieta)*xxi;
    x(i,j) = aux1*(aux2-2*b*xxieta+aux4+aux10);

    % Approximate coordinate y
    %-----
    aux5 = a*(y(e,j)+y(d,j));
    aux7 = g*(y(i,gg)+y(i,f));
    aux10 =
(xxi*xxieta+yxi*yxieta)*yeta+(xeta*xxieta+yeta*yxieta)*yxi;
    y(i,j) = aux1*(aux5-2*b*yxieta+aux7+aux10);

    % SOR : accelerating convergence
    %-----
    x(i,j) = (1.-w)*xc(i,j)+w*x(i,j);
    y(i,j) = (1.-w)*yc(i,j)+w*y(i,j);
end
end

% Convergence Check
%-----
err = max(max(max(abs(x-xc)),max(max(abs(y-yc)))));

% Real Time Animation
%-----
if (mod(k,40)==0),
    orient landscape;
    mesh(x,y,u,'EdgeColor','black');
    xlabel('x','FontSize',18);
end

```

```
        ylabel('y','FontSize',18);
        view(0,90);
        title(['CALCULATING - ITER =',num2str(k)]);
        pause(0.01);
    end

end

% In case algorithm is Diverging
%-----
if (k >= N || err >= tol);
    fprintf('\n ***** \n');
    fprintf('***** The Numerical Method is Diverging ***** \n');
    fprintf('***** \n');
    orient landscape;
    mesh(x,y,u,'EdgeColor','black');
    axis tight;
    view(0,90);
    title('DIVERGING','FontSize',18);
    xlabel('x','FontSize',18);
    ylabel('y','FontSize',18);
end

return
```